The Direct Wave-Drive Thruster

Matthew Solomon Feldman

A Dissertation
Presented to the Faculty
of Princeton University
in Candidacy for the Degree
of Doctor of Philosophy

Recommended for Acceptance
by the Department of
Mechanical and Aerospace Engineering
Adviser: Professor Edgar Y. Choueiri

June 2017

© Copyright by Matthew Solomon Feldman, 2017.

All rights reserved.

Abstract

A propulsion concept relying on the direct, steady-state acceleration of a plasma by an inductive wave-launching antenna is presented. By operating inductively in steady state, a Direct Wave-Drive Thruster avoids drawbacks associated with electrode erosion and pulsed acceleration. The generalized relations for the scaling of thrust and efficiency with the antenna current are derived analytically; thrust is shown to scale with current squared, and efficiency is shown to increase with increasing current or power. Two specific configurations are modeled to determine nondimensional parameters governing the antenna-plasma coupling: an annular antenna pushing against a finite-conductivity plasma, and a linear antenna targeting the magnetosonic wave. Calculations from the model show that total thrust improves for increasing excitation frequencies, wavenumbers, plasma densities, and device sizes.

To demonstrate the magnetosonic wave as an ideal candidate to drive a DWDT, it is shown to be capable of carrying substantial momentum and able to drive a variable specific impulse. The magnetosonic wave-driven mass flow is compared to mass transport due to thermal effects and cross-field diffusion in order to derive critical power requirements that ensure the thruster channel is dominated by wave dynamics.

A proof-of-concept experiment is constructed that consists of a separate plasma source, a confining magnetic field, and a wave-launching antenna. The scaling of the increase of exhaust velocity is analytically modeled and is dependent on a nondimensional characteristic wavenumber that is proportional to the excitation frequency and plasma density and inversely proportional to the magnetic field strength. Experimental validation of the derived scaling behavior is carried out using a Mach probe to measure the flow velocity in the plume. Increases in exhaust velocity are measured as the antenna current increases for varying excitation frequencies and applied magnetic field strengths. The scaling of the increase in exhaust velocity is observed to be consistent with our model's predictions.

Acknowledgements

I first want to acknowledge my advisor, Professor Edgar Choueiri, for accepting me into the lab and granting me the freedom to pursue a novel thruster concept. Eddie, you have demanded my best and pushed me to continually refine my ideas. Thank you for being both my fiercest critic and fiercest advocate.

None of my experimental work would have been possible without the help of Bob Sorenson. Bob, your technical expertise was invaluable, and you were always willing to help track down a ground loop or take a late-night phone call when something went wrong. Thank you for your friendship and for sticking around long enough to help me to the finish line.

I owe a number of people who have spent many hours in committee meetings, commenting on my dissertation, or helping me prepare for generals. Prof. Sam Cohen, Prof. Julia Mikhailova, Dr. Mikhail Shneider, and Dr. Yevgeny Raitses, thank you for your mentorship throughout this process. I would like to especially acknowledge Prof. Cohen. You consistently made yourself available to offer advice on how to improve as a researcher and encouragement when work was tough. From Shabbat evenings to committee meetings, I am grateful for your supportive and friendly voice.

To my EPPDyLite friends and colleagues, you develop a special bond when working together in the G-Wing subbasement, and I cannot express how much you meant to me during my time at Princeton. Danny, Ben, and Justin, thank you for showing me the ropes and grilling me for generals. To the younger generation, Taller Matt, Chris, Pat, Will, Mike, Sebastian, and Pierre-Yves, thank you for bringing in new energy and humor to the lab. Ben, I am especially grateful for your continued guidance and collaboration even after you graduated. Justin and Chris, thank you both for being a sounding board to new ideas and a shoulder to lean on while enjoying a restorative beer (Justin) or coffee (Chris). Will, Sebastian, and Pierre-Yves, thank you for your efforts to improve the lab, and good luck as you make your way to the finish line.

I am grateful to the many friends I made at Princeton that have shared this journey with me, and I would like to give a special shout-out to Josh Spechler and Anthony DeGennaro. Josh, you were a constant source of humor, wisdom, and friendship. Our lunches together always helped me see new perspectives on research, politics, and everything else. Anthony, you were a great roommate and even better friend. From teaching me to smoke ribs to challenging my random philosophical musings, I could always count on you to help me unwind after a set back. PS - On page iv of your thesis, you accidentally disparage the great Dallas Cowboys when you clearly meant to praise them. I look forward to an errata.

Finally, to my family - Joshua and Dara, I am thankful we were all on the East Coast for so long together. I can't imagine anyone else willing to take my 4am phone calls or wake up at 4am just to go skiing with me. You are the best brother and best sister I could ask for. Mom and Dad, you have shown me love and patience, and you both have a generosity of spirit that I can only hope to emulate. I owe you everything. 123.

The research in this dissertation was carried out with the support of the Princeton Plasma Physics Laboratory's (PPPL) Program in Plasma Science and Technology (PPST) and the Jet Propulsion Laboratory's (JPL) Strategic University Research Partnership (SURP). This dissertation carries T-3332 in the records of the Department of Mechanical and Aerospace Engineering.

in memory of my grandparents

Contents

List of Tables

List of Figures

List of Symbols

a	Cylindrical separation constant
A	Vector potential field
A_s	Spatial varying-component of the vector potential
A_{cs}	Thruster cross-sectional area
A_p	Area of Langmuir probe tip
B	Magnetic field
B_0	Applied magnetic field strength
B_f	B-field at the front surface the wave-launching antenna
B_r	B-field at the return surface the wave-launching antenna
c	Speed of Light
c_s	Sound speed
C_i	Wave-mode amplitude coefficients
C_T	Thrust coefficient
d	Antenna-plasma stand-off distance
D_P	Plasma dissipation parameter
D_{wla}	Wave-launching antenna dissipation parameter
$D_\perp$	Cross-field diffusion coefficient
e	Elementary charge
E	Electric field
$\mathcal{E}$	Energy density
$\dot{\mathcal{E}}$	Energy flux density
f_ϵ	Ion energy distribution function
F	Force
H	Half-width of the linear wave-launching antenna
I_c	Collector current in the retarding potential analyzer
I_d	Downstream ion saturation current of the Mach probe

I_u	Upstream ion saturation current of the Mach probe
I_{sat}	Ion saturation current of the Langmuir probe
J_a	Amplitude of oscillating current in wave-launching antenna
J_p	Current density in plasma
J_1	Bessel function of the first kind
k	Wavenumber
k_a	Alfvén wavenumber
k_v	Vacuum wavenumber
k_x	Wavenumber in the $\hat{x}$ direction (Perpendicular)
k_z	Wavenumber in the $\hat{z}$ direction (Parallel)
k_{zm}	Maximum k_z in the experimental configuration
k_1	Vacuum wavenumber in the $\hat{x}$ direction
k_2	Plasma wavenumber in the $\hat{x}$ direction
K	Normalized characteristic wavenumber
l	Antenna forward-return current path separation distance
L	Diameter of plasma source
m_e	Mass of electron
$\dot{m}$	Mass flow
$\dot{m}_{th}$	Thermally driven mass flow
$\dot{m}_{\text{wall}}$	Mass diffusion losses to walls
$\dot{m}_{\text{wave}}$	Wave-driven mass flow
M	Mach number
n_e	Plasma electron density
P	Power
$\overline{\overline{P}}_{EM}$	Maxwell stress tensor
P_T	Thrust power
$P_{L,\text{plasma}}$	Resistive power loss in plasma

$P_{L,\mathrm{wla}}$	Resistive power loss in wave-launching antenna
$P_{L,\mathrm{rad}}$	Radiative power loss
P_L	Total power losses
$\dot{\mathcal{P}}$	Momentum flux density
$\mathcal{P}$	Momentum density
p_{th}	Thermal pressure
p_B	Magnetic pressure
P_{wave}	Total wave power
P^*_{th}	P_{wave} required for $\Pi_{th} > 1$
P^*_{wall}	P_{wave} required for $\Pi_{\mathrm{wall}} > 1$
P_{PSA}	Power to the plasma source antenna
P_{WLA}	Power to the wave-launching antenna
R_{rad}	Radiation resistance
R_{plasma}	Plasma resistance
R_{wla}	Wave-launching antenna resistance
r_0	Inner radius of annular solution geometry
r	Radial coordinate
r_s	Radius on surface of annular antenna geometry
T	Thrust
t	Time
T_e	Electron temperature
u_{ex}	Exhaust Velocity
v_ϕ	Phase velocity
v_1	Amplitude of velocity oscillation
v_A	Alfvén velocity
v_{th}	Thermal velocity
V	Voltage

x	Cartesian coordinate in the direction of thrust
y	Cartesian coordinate
Y	Height of the wave-launching antenna in the $\hat{y}$ direction
z	Cartesian coordinate
Z_0	Impedance of free space
α	Plasma resistance coupling parameter
γ	Thrust coefficient coupling parameter
$\Gamma_{\mathcal{E}}$	Wave-driven Engery flux
$\Gamma_{\mathcal{M}}$	Wave-driven mass flux
$\Gamma_{\mathcal{P}_{\mathrm{EIC}}}$	Momentum flux for the electrostatic ion cyclotron wave
$\Gamma_{\mathcal{P}_{\mathrm{MS}}}$	Momentum flux for magnetosonic wave
δ_s	Plasma skin depth
Δu_{ex_p}	Increase in u_{ex} as wave-launching antenna is powered
$\epsilon_\perp$	Cross-field dielectric constant
η	Efficiency
θ_ν	Inverse tangent of $\bar{\nu}$
Θ	Heaviside step function
κ_m	Mach probe calibration constant
μ_0	Permeability of Free Space
ν_e	Electron collision frequency
$\bar{\nu}$	ν_e normalized by ω
Π_{th}	Ratio of $\dot{m}_{\mathrm{wave}}$ to $\dot{m}_{th}$
Π_{wall}	Ratio of $\dot{m}_{\mathrm{wave}}$ to $\dot{m}_{\mathrm{wall}}$
ρ_0	Average mass density
ρ_1	Amplitude of mass density oscillation
σ	Conductivity
τ	Time normalized to the annular excitation frequency

ω	Annular excitation frequency
ω_{ce}	Electron cyclotron frequency
ω_{ci}	Ion cyclotron frequency
ω_{pe}	Electron plasma frequency
ω_{pi}	Ion plasma frequency

Chapter 1

Introduction

The Direct Wave-Drive Thruster (DWDT) is a new, steady-state propulsion concept that uses waves to transfer momentum directly to a plasma. As an electric thruster that uses electromagnetic fields to accelerate the propellant, it retains the key benefits of other electric devices, namely the ability to generate high exhaust velocities[1]. Additionally, by using an inductive wave-launching antenna (WLA), a DWDT can operate without electrodes, which prevents lifetime limitations associated with erosion processes seen in many electric propulsion concepts[2, 3, 4, 5, 6, 7, 8] and allows compatibility with a variety of propellants.

At its core, a DWDT consists of two key features. The first is the WLA which should be designed to target high momentum density wave-modes within a plasma. The second is an applied magnetic field, which confines the plasma and can be tuned to create desirable wave-modes with the system. A simple DWDT channel is shown in Figure 1.1. In the shown configuration, the WLA is positioned just outside the plasma on the left side of the channel. Waves are launched into the plasma in the positive $\hat{x}$-direction in order to generate exhaust in the same direction.

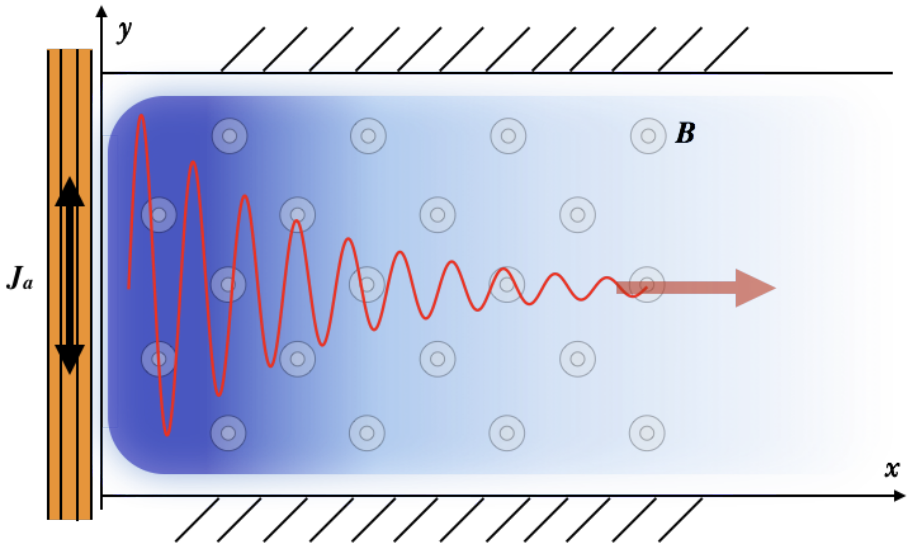

Figure 1.1: A Direct Wave-Drive Thruster Channel. Plasma is confined in a thruster channel with an applied magnetic field. A wave-launching antenna structure is placed behind the channel, which generates a propagating mode in the positive $\hat{x}$-direction. In steady state, the propagating mode accelerates the plasma across field lines and out of the thruster.

1.1 Motivation for Direct, Waves-Based Electric Propulsion

In general, electric thrusters are used for their ability to deliver high exhaust velocities and limit the total propellant mass requirements for various missions[1]. Typically, these devices use any number of electric and magnetic field configurations, in steady or unsteady operation, in order to accelerate a plasma to the required speeds. By reaching exhaust velocities much higher than chemical rockets, an electric thruster can dramatically reduce the total propellant mass requirement for a given mission.

While there are many ways to accelerate a plasma, two primary types of electric thrusters are used for in-space missions: electrostatic ion thrusters[3, 4] and Hall thrusters[5, 6]. Both devices use an electric field to accelerate ions and neutralize the exhaust beam with a cathode that may be required to supply 10s or 100s of amps for future missions[9, 10, 11, 12]. And other higher power concepts, such as Magnetoplas-

madynamic thrusters (MPDT) may require even larger currents[13]. Unfortunately, at sufficiently high currents, most modern cathodes can experience significant erosion which can limit their useful lifetimes.

Because of these potential lifetime limitations, many electrodeless concepts have been developed, which naturally avoid these erosion processes. Broadly speaking, these concepts can be grouped into two major categories: magnetic nozzles[14, 15, 16, 17] and pulsed inductive accelerators[18, 19, 20, 21], and both types suffer from various drawbacks.

Magnetic nozzles are typically operated by heating a plasma and then transforming that thermal energy into directed kinetic energy via an expansion process that generates useful thrust. Therefore, efficient magnetic nozzles often require a separate heating stage[15]. Furthermore, a primary concern for magnetic nozzle concepts is the efficacy of plasma detachment from the magnetic topology during and after the acceleration process[22, 23]. Not only does the magnetic field divergence lead to efficiency losses, but the undetached particles can follow the magnetic field lines and impinge back onto the spacecraft[24]. Additionally, these these devices are typically inefficient at lower powers[16, 17].

Meanwhile, pulsed devices may require over 10^{10} pulses in typical missions, which can also pose various lifetime limitations[25]. Since plasma breakdown must be initialized during each pulse, the high instantaneous power requirements can lead to degradation of the pulsed circuitry. Additionally, to prevent mass utilization losses, injection valves must be operated during each pulse. While some systems have been designed to limit the peak current requirements via pre-ionization of the gases[19, 26], this leads to added system complexity and additional points of failure.

Various other electrodeless concepts have been explored which blend acceleration methods by using rotating electromagnetic fields in magnetic nozzle-like configurations[27, 28]. And another electrodeless concept uses the ponderomotive

force from electron cyclotron waves to directly accelerate electrons[29] and accelerates ions with the developed ambipolar field. However, the proposed topology for all of these devices still requires a magnetic nozzle and therefore shares many of the concerns described above.

More recently, Jorns and Choueiri proposed a direct, wave-drive device[30] that relies on the ponderomotive force obtained from damping beating electrostatic waves[31, 32, 33, 34] to naturally drive plasma motion across magnetic field lines[35], and therefore it does not rely on a magnetic nozzle topology. This force has already been explored to create plasma flows[36, 37, 38, 39], drive currents[40, 41, 42], and confine plasmas[43]. However, theoretical investigations these wave-driven forces have focused solely on the wave-plasma interaction within the plasma control volume. In Jorns' and Choueiri's proposed concept, they do not consider the wave-launching mechanism and assume waves are generated from a annular spiral antenna with no losses. While their approach describes the momentum absorption, it ignores the inductive interactions that initially couple momentum into the plasma from an antenna structure. For any direct, wave-drive device, all of the momentum contained in the excited waves - and subsequently the bulk plasma - must be obtained from this inductive coupling. By analyzing this coupling, we can derive the general scaling behavior for both thrust and thrust efficiency.

While there are many potential benefits of direct, steady-state, waves-based acceleration, there is not yet a fundamental framework to describe this class of accelerator. This framework is critically important to understanding any new electric propulsion concept because electric accelerators require an external power source which is generally more massive for larger power requirements. Therefore, before such devices can be a viable alternative to various other electric thrusters, it is necessary to understand how thrust, thrust efficiency, and exhaust velocity scale.

1.2 Scope and Structure of Thesis

The ultimate goal of this dissertation is to present the Direct Wave-Drive Thruster concept, as well as describe and validate a framework for analyzing this class of thruster. In particular, we seek to understand the fundamental laws governing the scaling of thrust, thrust efficiency, and exhaust velocity of such devices. In order to guide future explorations, we develop design criteria necessary for effective performance dependent on the targeted wave-modes and geometry of the system. Finally, we test our theoretical approach by designing a proof-of-concept experiment. The purpose of this experiment is not to build an optimized thruster, but rather to validate the derived scaling laws for momentum coupling into the plasma.

In Chapter 2, we derive the general scaling of thrust, T, and thrust efficiency, η, as a function of the amplitude of the current oscillation in the WLA. We then use this approach to derive specific thrust and loss coefficients in order to estimate the dependence of T and η on various plasma parameters of interest. Next, we motivate the use of the magnetosonic wave as particularly promising wave-mode of interest in Chapter 3. For a DWDT driven by this mode, we derive design criteria to ensure the wave dynamics dominate the system performance, and we derive the scaling behavior of the thrust coefficient in a simplified linear geometry.

In order to validate our theoretical approach for the calculation of the thrust and exhaust velocity scaling, we design a proof-of-concept experiment, which is described in Chapter 4. In Chapter 5, we analytically model the antenna-plasma coupling in the experimental configuration and measure the increases in exhaust velocity as the wave-launching antenna is powered. Finally, we compare the measured and predicted scaling behaviors and show that the coupling is dependent on a single characteristic wavenumber of the system.

We summarize our findings in Chapter 6, and provide insight into future work on DWDT concepts.

Chapter 2

Direct Wave-Drive Thruster Global Scaling Model[1]

Before delving into detailed analyses of plasma wave-modes and optimizing thruster performance, it is necessary to have a framework for discussing DWDTs that can be used to gauge their potential efficacy. To do this, we must be able to describe the fundamental scaling behavior of thrust and thrust efficiency as a function of various relevant parameters. For steady-state electromagnetic thrusters, such as MPDTs, the scaling behavior is general considered as a function of the applied current that flows between the electrodes and through the plasma[1, 45]. We will follow a similar approach, except the current of interest is that flowing - and oscillating - in the WLA. As we follow this approach, we will find the thruster performance is also dependent on geometry of the system, and various plasma parameters that control the inductive coupling between the plasma and antenna.

The goals of this chapter are to understand the fundamental physics governing the antenna-plasma interaction in DWDTs and derive general and specific equations for

[1]This chapter is based on work currently submitted for publication and previously presented in [44]: Feldman, M.S. and Choueiri, E.Y., "The Direct Wave-Drive Thruster," *50th AIAA/ASME/SAE/ASEE Joint Propulsion Conference*, AIAA-2014-4025, Cleveland, OH, July 28-30, 2014.

the scaling of thrust and thrust efficiency. We start in Section 2.1 by describing the antenna-plasma momentum coupling for a general DWDT and deriving the scaling behavior with increasing driving current. In Section 2.2, we set up an annular DWDT configuration in order to calculate specific thrust and loss coefficients, and we use those coefficients to evaluate thrust and efficiency as a function of various non-dimensional parameters in Section 2.3. Finally in Section 2.4, we summarize the results and discuss the limits of our analytical approach.

2.1 Thrust and Efficiency Model

In its simplest form, the DWDT consists of a confining background magnetic field and a wave-launching antenna, as shown in Figure 1.1. The background $\boldsymbol{B}$-field confines plasma away from the walls and also can be tuned to create wave-modes of interest inside of the thruster that can be coupled to by the wave-launching antenna (WLA).

We desire a simplified analytical model that can predict the basic scaling behavior of thrust and efficiency for a wide range of DWDT parameters. To do this, we must first understand the basic thrust mechanisms and power loss mechanisms that will be dominant in such a concept. The major thrust contribution for a DWDT comes from momentum imparted to the plasma via the WLA. In our simplified model, we will neglect any cold gas and electrothermal thrust components. As a result, the total thrust can be calculated from the electromagnetic interaction between the plasma and the WLA. This force is applied continuously, so the total thrust is determined by time-averaging these electromagnetic forces.

We approximate thrust efficiency by considering only the resistive and radiative losses associated with the antenna-plasma coupling. This ignores non-idealized effects, such as wall losses, frozen flow losses, and imperfect mass utilization. As a result, we derive an upper bound on the thrust efficiency constrained by the Ohmic losses in

the plasma and antenna, as well as the radiative energy losses from wave-modes that do not contribute to thrust.

2.1.1 Thrust

The WLA is responsible for all momentum transferred to the plasma and acquired by the exhaust. As a result, we can calculate the total thrust by time-averaging the electromagnetic pressure exerted on the plasma. Assuming little momentum is lost to by radiation to vacuum, this total force exactly equals the force on the WLA.

Therefore, the total electromagnetic thrust is simply:

$$T = \int_S \langle \overline{\overline{P}}_{EM_{ij}} \rangle \cdot dA, \tag{2.1}$$

where the integral is taken over the surface of the plasma, similar to the derivations for self-field MPDTs[1, 45], and the brackets represent a time-averaging over the oscillating period. This electromagnetic pressure, $\overline{\overline{P}}_{EM_{ij}}$, is the typical Maxwell stress tensor

$$\overline{\overline{P}}_{EM_{ij}} = \epsilon_0 (E_i E_j - \frac{1}{2}\delta_{ij} E^2) + \frac{1}{\mu_0}(B_i B_j - \frac{1}{2}\delta_{ij} B^2). \tag{2.2}$$

If we assume a linear response of the plasma to the excitation in the WLA, the magnitudes of the oscillating electric and magnetic fields are proportional to the magnitude of the exciting current in WLA, J_a. Therefore, the total pressure and total thrust must be proportional to current squared.

$$T = C_T J_a^2, \tag{2.3}$$

and the thrust coefficient, C_T is dependent on the geometry of the system, excitation frequency, and the plasma response. We present an explicit calculation of C_T in an annular DWDT configuration in Section 2.2.

2.1.2 Efficiency

We can determine the scaling of thrust efficiency by determining the total thrust power and the power dissipated by the various loss mechanisms. Thrust power is dependent on mass flow and is given by

$$P_T = \frac{T^2}{2\dot{m}}. \tag{2.4}$$

The dominant loss mechanisms are resistive and radiative in nature. In the plasma, Ohmic heating can be calculated with

$$P_{L,\text{plasma}} = \int \langle \boldsymbol{J}_p \cdot \boldsymbol{E} \rangle \, dV, \tag{2.5}$$

where $\boldsymbol{J}_p$ and $\boldsymbol{E}$ are the currents and electric fields in the plasma and we integrate over the full plasma volume. Again assuming a linear response, both terms are proportional to the excitation current in the WLA, J_a. While some electric accelerators recover thrust from the heating of the plasma, it is usually done with a magnetic nozzle. Since a DWDT is designed to operate without one, we assume this energy is lost to bound system performance.

The resistive dissipation in the WLA and any of the radiative energy loss that does not contribute to thrust also scale with J_a^2:

$$P_{L,\text{wla}} = \langle R_{\text{wla}} J_a^2 \rangle, \tag{2.6}$$

$$P_{L,\text{rad}} = \langle R_{\text{rad}} J_a^2 \rangle, \tag{2.7}$$

where the antenna's ohmic and radiative resistances, R_{wla} and R_{rad} respectively, may be dependent on the frequency of excitation.

Putting these losses together, the total power loss is

$$P_L = \langle (R_{\text{plasma}} + R_{\text{wla}} + R_{\text{rad}}) J_a^2 \rangle = \frac{1}{2} R_{\text{eff}} J_a^2, \tag{2.8}$$

where R_{eff} is the overall effective resistance of the combined losses, and the factor of $\frac{1}{2}$ comes from time-averaging over the oscillation.

Finally, the efficiency of the thrust transfer is thrust power divided by total power consumed. That is,

$$\eta = \frac{P_T}{P_T + P_L} = \frac{1}{1 + \dfrac{\dot{m} R_{\text{eff}}}{C_T^2 J_a^2}}, \tag{2.9}$$

where R_{eff} is a loss coefficient that can have, like C_T, a complicated dependence on geometry and plasma dynamics. While thrust in a DWDT scales with current squared, thrust efficiency also improves with increasing current. This scaling behavior is quite similar to that derived for self-field MPDTs[45], except that the generated electromagnetic pressure is coupled to the plasma inductively.

2.2 Thrust and Loss Coefficient Derivations in an Annular Geometry

The basic scaling behavior of a DWDT with respect to the antenna current is straightforward. When assuming a linear response, an efficient thruster can be created with sufficient current or power. However, in order to determine how much power is required to create an efficient device, we must understand how both C_T and R_{eff} are affected by the configuration of the WLA, the properties of the plasma, and the targeted wave-modes. In this section, we will calculate the thrust and efficiency for a specific configuration in order to bound thruster performance.

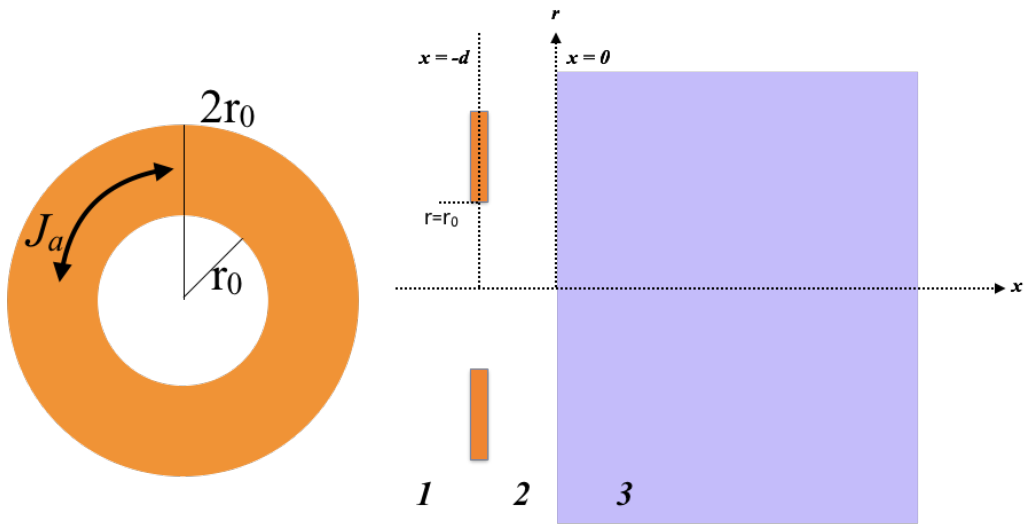

Figure 2.1: Antenna and Plasma Geometry. The antenna is assumed to be an annulus with inner and outer radii r_0 and $2r_0$ respectively and a total current J_a evenly distributed along the radius. The antenna is position a distance d from the surface of the plasma, which is assumed to occupy the infinite half-space $x > 0$. The geometry is therefore cylindrically symmetric about the $\hat{x}$-axis.

We start by taking the antenna to have a fixed annular geometry similar to the antenna configurations used in PITs[18, 19] and proposed for devices like the Ponderomotive thruster[30]. We assume current is distributed evenly through a flat annulus with inner radius r_0 and outer radius $2r_0$ positioned parallel to a flat plasma surface at a stand-off distance d as shown in Figure 2.1. We further simplify the model by treating the plasma as a uniform, semi-infinite slab occupying a half-space a fixed distance from the annular WLA and assume the plasma is pre-ionized in order to isolate the antenna-plasma interaction. Finally, we do not include a background magnetic field. As a result, only the collisional, evanescing ordinary mode is present in the plasma. And finally we note that the approximation of a plasma with infinite extent holds well for high plasma conductivities, which will correspond to stronger coupling between the WLA and the plasma.

In order to calculate the thrust coefficient, C_T, and the plasma resistance, R_{plasma}, we assume an oscillating azimuthal source current with magnitude J_a evenly dis-

tributed in the WLA and solve Maxwell's equations throughout the geometry. Once we have solved for the electric and magnetic fields, the force on the plasma can be immediately determined. The currents and fields in the plasma are determined by the frequency-dependent plasma conductivity, which is primarily a function of the plasma density, and electron collision frequency.

2.2.1 Magnetic Vector Potential Solution

In this configuration, it is easiest to calculate the electric and magnetic fields via the magnetic vector potential, $\boldsymbol{A}$, where

$$\boldsymbol{B} = \nabla \times \boldsymbol{A}, \qquad \boldsymbol{E} = -\frac{\partial \boldsymbol{A}}{\partial t}, \qquad \boldsymbol{J} = -\sigma \frac{\partial \boldsymbol{A}}{\partial t}. \tag{2.10}$$

Because of the cylindrical symmetry, $\boldsymbol{A}$ is purely is the azimuthal direction, and the wave equation becomes

$$\nabla^2 \boldsymbol{A} - \frac{1}{c^2}\frac{\partial^2 \boldsymbol{A}}{\partial t^2} - \mu_0 \sigma \frac{\partial \boldsymbol{A}}{\partial t} = \mu_0 \boldsymbol{J_0}, \tag{2.11}$$

where σ is the frequency-dependent conductivity, which is 0 in free space, and $\boldsymbol{J}_0 = ({}^{J_a}/_{r_0})\delta(x+l)$ is the excitation current density in the WLA. To solve, we allow J_a and $\boldsymbol{A}$ to vary sinusoidally with a given frequency, such that, $\boldsymbol{A} = \boldsymbol{A}_s\, e^{i\omega t}$, where $\boldsymbol{A}_s$ is the spatially-varying part of $\boldsymbol{A}$ and is complex-valued. The complex conductivity can be obtained from the linearized electron momentum equation;

$$\sigma = \frac{e^2 n_e}{m_e(\nu_e + i\omega)} = \frac{1}{\mu_0}\frac{\omega_{pe}^2}{c^2}\frac{1}{\nu_e + i\omega}, \tag{2.12}$$

where m_e is the mass of an electron, n_e is the electron density, ν_e is the electron collision frequency.

We also assume that the input frequencies are sufficiently small that the second-order time derivative is negligible, so that

$$\nabla^2 \boldsymbol{A}_s - \frac{\omega_{pe}^2}{c^2} \frac{i\omega}{\nu_e + i\omega} \boldsymbol{A}_s = \mu_0 \boldsymbol{J_0}. \tag{2.13}$$

This assumption is equivalent to assuming that the speed of light in vacuum in large or that the wave-lengths of vacuum-propagating wave-modes are large compared to the size of the system.

We solve for $\boldsymbol{A}$ following closely the solution used by Dodd and Deeds[46], who solved a similar configuration using a single coil near a material with purely real conductivity. However, we use Equation 2.12 for the plasma conductivity and also integrate over many loops to form a flat annular antenna. Like in other wave-coupling solutions[47, 48], we split the solution space into separate domains (shown in Figure 2.1) corresponding to $x < -d$, $-d < x < 0$, and $x > 0$, solve each domain separately, then match boundary conditions in order to stitch together a unique self-consistent solution. Before proceeding, we non-dimensionalize Eq. 2.13 using the following scheme based on the geometry described above:

$$\bar{r} = {}^{r}/_{r_0} \qquad \bar{x} = {}^{x}/_{r_0} \qquad \bar{d} = {}^{d}/_{r_0} \qquad \delta_s = {}^{c}/_{\omega_{pe}} \qquad \bar{\delta}_s = {}^{\delta_s}/_{r_0} \qquad \bar{\nu} = {}^{\nu_e}/_{\omega} \qquad \tau = \omega t,$$

where $\bar{r}, \bar{x}$ are the normalized cylindrical coordinates, d is the antenna-plasma stand-off distance, and δ_s is the classical plasma skin depth.

In region 1 and 2 there is no plasma, and the vector potential diffusion equation becomes

$$\nabla^2 \boldsymbol{A}_s = 0, \tag{2.14}$$

where ∇ is now the spatial gradient with respect to the normalized coordinate system. In region 3, the equation becomes

$$\nabla^2 \boldsymbol{A}_s - \bar{\delta}_s^{-2} \frac{1}{\sqrt{1+\bar{\nu}^2}} e^{i \tan^{-1} \bar{\nu}} \boldsymbol{A}_s = 0. \tag{2.15}$$

Finally, we define $\theta_\nu = \tan^{-1}\bar{\nu}$, where θ_ν is between 0 and $\frac{\pi}{2}$, so that

$$\nabla^2 \boldsymbol{A}_s - \bar{\delta}_s^{-2}\cos\theta_\nu e^{i\theta_\nu}\boldsymbol{A}_s = 0. \tag{2.16}$$

This is expanded into the cylindrical coordinate system;

$$\frac{1}{\bar{r}}\frac{\partial}{\partial\bar{r}}(\bar{r}\frac{\partial \boldsymbol{A}_s}{\partial\bar{r}}) - \frac{\boldsymbol{A}_s}{\bar{r}^2} + \frac{\partial^2\boldsymbol{A}_s}{\partial\bar{x}^2} - \bar{\delta}_s^{-2}\cos\theta_\nu e^{i\theta_\nu}\boldsymbol{A}_s = 0. \tag{2.17}$$

In order to calculate the forces on and dissipation within the plasma, we only need to know $\boldsymbol{A}$ in region 3, but we need to solve for the equations in all three regions simultaneously. The full derivation is performed in the Appendix A.1 and yields

$$\boldsymbol{A}_{3s} = \mu_0 J_a \int_0^\infty\int_1^2 \bar{r}_s J_1(a\bar{r}_s)J_1(a\bar{r})\frac{a}{a+\sqrt{a^2+\bar{\delta}_s^{-2}\cos\theta_\nu e^{i\theta_\nu}}}e^{-a\bar{d}}e^{-\sqrt{a^2+\bar{\delta}_s^{-2}\cos\theta_\nu e^{i\theta_\nu}}\bar{x}}d\bar{r}_s da, \tag{2.18}$$

where J_1 is a Bessel function of the first kind, and we are integrating over a, the spatial separation constant, and $\bar{r}_s$ is the normalized location on the surface of the annulus. The time-dependent solution is further normalized by defining $\bar{\boldsymbol{A}} = \boldsymbol{A}/(\mu_0 J_a)$, such that

$$\bar{\boldsymbol{A}}_{3s}(\bar{r},\bar{x},\bar{\delta}_s,\bar{l},\theta_\nu,\tau) = e^{i\tau}\int_0^\infty\int_1^2 \bar{r}_s J_1(a\bar{r}_s)J_1(a\bar{r})\frac{a}{a+\sqrt{a^2+\bar{\delta}_s^{-2}\cos\theta_\nu e^{i\theta_\nu}}}e^{-a\bar{d}}e^{-\sqrt{a^2+\bar{\delta}_s^{-2}\cos\theta_\nu e^{i\theta_\nu}}\bar{x}}d\bar{r}_s da. \tag{2.19}$$

2.2.2 Thrust Coefficient, C_T

The net electromagnetic force generated on the plasma can be calculated from the integration of the $\boldsymbol{J} \times \boldsymbol{B}$ force density in the plasma;

$$\boldsymbol{F} = \int \mathtt{Re}[\boldsymbol{J}] \times \mathtt{Re}[\boldsymbol{B}] dV. \tag{2.20}$$

Using Eqs. 2.10 and the normalization scheme,

$$\boldsymbol{F} = \mu_0 J_a^2 \int \mathtt{Re}[-\bar{\delta}_s^{-2} \cos\theta_\nu e^{i\theta_\nu} \bar{\boldsymbol{A}}] \times \mathtt{Re}[\nabla \times \bar{\boldsymbol{A}}] d\bar{V}. \tag{2.21}$$

Since $\boldsymbol{A}$ is only in the $\hat{\theta}$ direction, we can rewrite the force component in the $\hat{x}$, i.e. thrust, direction as

$$F_x = -\mu_0 J_a^2 \bar{\delta}_s^{-2} \cos\theta_\nu \int \mathtt{Re}[e^{i\theta_\nu} \bar{\boldsymbol{A}}] \cdot \mathtt{Re}[\frac{\partial \bar{\boldsymbol{A}}}{\partial \bar{x}}] d\bar{V}. \tag{2.22}$$

By time-averaging the total axial force and applying the divergence theorem, we get

$$T = \frac{\pi}{2} \mu_0 J_a^2 \bar{\delta}_s^{-2} \cos^2\theta_\nu \int_0^\infty \|\bar{\boldsymbol{A}}_{3s}(\bar{r}, \bar{x} = 0, \bar{\delta}_s, \bar{l}, \theta_\nu)\|^2 \bar{r} d\bar{r}. \tag{2.23}$$

The maximum of the time-averaged force, $T_{\max} = \frac{3}{4}\pi\mu_0 J_a^2$, occurs as $\bar{\delta}_s, \bar{l}, \theta_\nu \to 0$. Physically, this occurs when the plasma density is sufficiently high and the electron collision frequency and stand-off distance are sufficiently small. This result is not surprising, as $T_{\max}$ is equal to the magnetic pressure between two infinite current sheets[49] multiplied by the area of the antenna and an additional factor of $\frac{1}{2}$ to account for the average over the period of oscillation.

Normalizing by this maximum force, we get

$$T(\bar{\delta}_s, \bar{l}, \theta_\nu, J_a) = T_{\max} \cdot \gamma(\bar{\delta}_s, \bar{l}, \theta_\nu), \tag{2.24}$$

where

$$\gamma(\bar{\delta}_s, \bar{d}, \theta_\nu) = \int_0^\infty \frac{2}{3}\bar{r} \left\| \int_0^\infty \int_1^2 \bar{r}_s J_1(a\bar{r}_s) J_1(a\bar{r}) \frac{a\bar{\delta}_s^{-1}\cos\theta_\nu}{a + \sqrt{a^2 + \bar{\delta}_s^{-2}\cos\theta_\nu e^{i\theta_\nu}}} e^{-a\bar{d}} d\bar{r}_s da \right\|^2 d\bar{r} \tag{2.25}$$

and is between 0 and 1.

Therefore, the thrust coefficient, C_T, is given by:

$$C_T = \frac{3}{4}\pi\mu_0 \ \gamma(\bar{\delta}_s, \bar{d}, \theta_\nu). \tag{2.26}$$

2.2.3 Plasma Resistance, R_{plasma}

The power dissipation in the plasma is calculated from the integration over the volume of joule-heating in the plasma;

$$P_{L,\text{plasma}} = \int \langle \mathtt{Re}[\boldsymbol{J}] \cdot \mathtt{Re}[\boldsymbol{E}] \rangle dV. \tag{2.27}$$

Again using Equation 2.10 and the normalization scheme, we have

$$P_{L,\text{plasma}} = \langle Z_0 J_a^2 \bar{\delta}_s^{-3} \frac{\omega}{\omega_{pe}} \cos\theta_\nu \int_0^\infty \int_0^\infty \left\{ \mathtt{Re}[e^{i\theta_\nu}\bar{\boldsymbol{A}}] \cdot \mathtt{Re}[i\bar{\boldsymbol{A}}] \right\} \bar{r} d\bar{r} d\bar{x} \rangle. \tag{2.28}$$

And the time-averaged result is

$$P_{L,\text{plasma}} = \pi Z_0 J_a^2 \bar{\delta}_s^{-3} \frac{\nu_e}{\omega_{pe}} \cos^2\theta_\nu \int_0^\infty \int_0^\infty \|\bar{\boldsymbol{A}}_s(\bar{r}, \bar{x}, \bar{\delta}, \bar{l}, \theta_\nu)\|^2 \bar{r} d\bar{r} d\bar{x} = \frac{1}{2} R_{\text{plasma}} J_a^2. \tag{2.29}$$

We can normalize the plasma resistance in a similar manner to C_T by separating a new coupling parameter, α, from a term dependent on the ratio of ν_e to ω_{pe}.

$$R_{\text{plasma}} = \frac{3}{2}\pi Z_0 J_a^2 \frac{\nu_e}{\omega_{pe}} \cdot \alpha(\bar{\delta}_s, \bar{d}, \theta_\nu), \tag{2.30}$$

where

$$\alpha(\bar{\delta}_s, \bar{d}, \theta_\nu) = \bar{\delta}_s^{-1} \times$$
$$\int_0^\infty\int_0^\infty \frac{4}{3}\bar{r}\left\| \int_0^\infty\int_1^2 \bar{r}_s J_1(a\bar{r}_s) J_1(a\bar{r}) \frac{a\bar{\delta}_s^{-1}\cos\theta_\nu}{a + \sqrt{a^2 + \bar{\delta}_s^{-2}\cos\theta_\nu e^{i\theta_\nu}}} e^{-a\bar{d}} e^{-\sqrt{a^2+\bar{\delta}_s^{-2}\cos\theta_\nu e^{i\theta_\nu}}\bar{x}} d\bar{r}_s da \right\|^2 d\bar{r} d\bar{x} \tag{2.31}$$

and is also between 0 and 1.

2.3 Parametric Investigation of Thrust and Thrust Efficiency

2.3.1 Scaling of C_T and R_{plasma} with dimensionless quantities

We now have analytical descriptions for C_T and R_{plasma} as functions of three non-dimensional parameters, $\bar{\delta}_s$, $\bar{d}$, and $\bar{\nu}$. The interplay of these three parameters is seen in Equations 2.25 and 2.31 for γ and α, both of which go to unity as $\bar{\delta}_s, \bar{d}, \bar{\nu} \to 0$. These equations do not have explicit solutions in terms of elementary functions, and therefore we performed numerical integrations over a parameter space from $\bar{\delta}_s = 1$ to $1/64$, $\bar{d} = 1$ to $1/16$, and $\bar{\nu} = 1/10$ to 10 ($\theta_\nu = .1$ to 1.47).

Figure 2.2 shows contour plots for the coupling parameter, γ, in terms of $\bar{\delta}_s$ and $\bar{d}$ for various values of $\bar{\nu}$. As expected, we can see that γ increases towards unity as $\bar{\delta}_s, \bar{d}, \bar{\nu} \to 0$. In the reverse direction, γ quickly decreases to zero. α and γ exhibit similar behavior, such that as γ increases, the dissipation losses also increase. Qualitatively, this occurs because more current must be present in the plasma in order to increase the net force. This additional current leads to more ohmic heating.

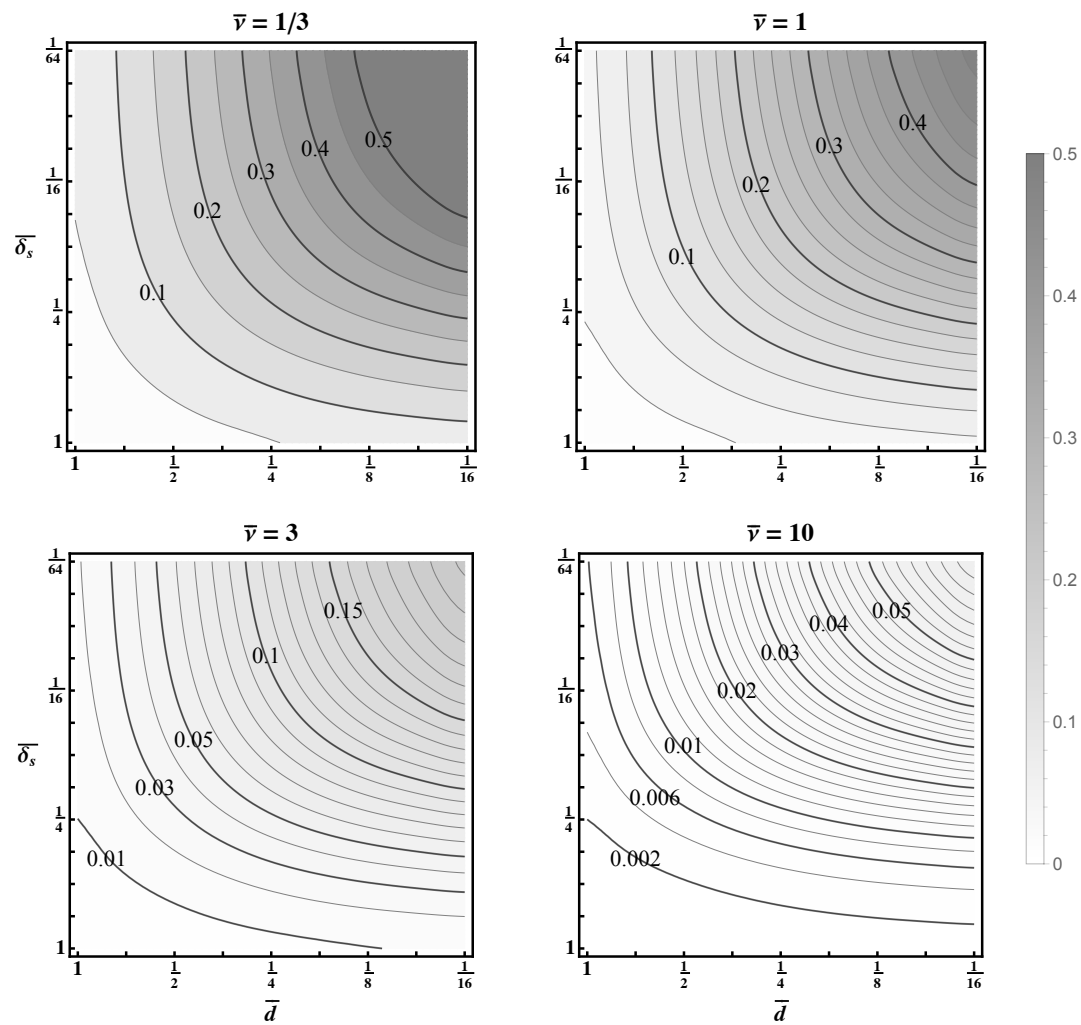

Figure 2.2: Contour Plots of the coupling parameter γ as a function of the normalized skin-depth, $\bar{\delta}_s$, the normalized stand-off distance, $\bar{d}$, and the normalized electron collision frequency, $\bar{\nu}$. Contours of γ are plotted on Log-Log plots of the antenna-plasma coupling length and the inverse of the plasma skin depth. The four plots correspond to varying normalized electron collision frequencies, $\bar{\nu}$. Darker regions correspond to larger γ.

2.3.2 Scaling of Efficiency

By recalling Equation 2.9, and ignoring losses from R_{wla} and R_{rad}, we have

$$\eta = \frac{1}{1 + \frac{\dot{m} R_{\text{plasma}}}{C_T^2 J_a^2}} = \frac{1}{1 + D_P}, \tag{2.32}$$

where $D_P = \frac{\dot{m}R_{\text{plasma}}}{C_T^2 J_a^2}$ is a normalized dissipation parameter. Substituting Equations 2.26 and 2.30 gives us

$$D_P = \frac{8\dot{m}c}{3\pi\mu_0 J_a^2}\frac{\nu_e}{\omega_{pe}}\frac{\alpha}{\gamma^2}, \tag{2.33}$$

where efficiency is improved by minimizing D_P. This can be achieved by increasing the total current in the antenna - and therefore the total power of the device - or by minimizing the ratio of α/γ^2, the ratio of ν_e/ω_{pe}, or the mass flow rate.

We put the above model in perspective by making assumptions typical of an electric propulsion device; $\dot{m} = 1\,\text{mg/s}$, $r_0 = 4\,\text{cm}$, $d = 1\,\text{cm}$, $n_e = 3 \times 10^{17}\,\text{m}^{-3}$, and $T_e = 5\,\text{eV}$, such that $\bar{\delta}_s = 1/4$ and $\bar{d} = 1/4$. For these values, the thrust efficiency can be calculated by assuming various $\bar{\nu}$, and Figure 2.3(a) shows plots of efficiency as a function of power for a range of $\bar{\nu}$. Clearly, improved performance occurs for smaller electron collision frequencies or higher input frequencies, which is the parameter most easily experimentally controlled.

We can account for resistive losses in the WLA by deriving a second dissipation parameter,

$$D_{\text{wla}} = \frac{16\dot{m}R_{\text{wla}}}{9\pi^2\mu_0^2 J_a^2}\frac{1}{\gamma^2}, \tag{2.34}$$

which is the ratio of power dissipated in the WLA to the thrust power, such that the efficiency becomes

$$\eta = \frac{1}{1 + D_P + D_{\text{wla}}} \tag{2.35}$$

In Figure 2.3(b), we hold the total input power fixed at 5 kW and vary the WLA resistance, R_{wla}, while plotting efficiency against the non-dimensional skin depth, $\bar{\delta}_s$. We find that decreasing skin depth and resistance both improve the calculated efficiency.

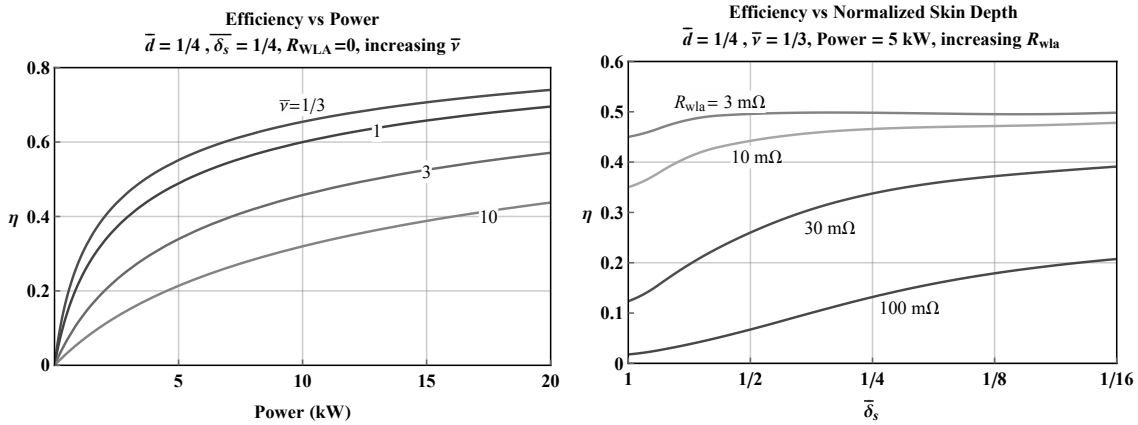

(a) (b)

Figure 2.3: Efficiency vs Power for fixed $\bar{d} = 1/4$. (a) Curves of η vs P for $R_{\text{wla}} = 0$, $\bar{\delta}_s = 1/4$, and increasing normalized electron collision frequency, $\bar{\nu}$. (b) Curves of η vs $\bar{\delta}_s$ for $P = 5\,\text{kW}$, $\bar{\nu} = 1/3$, and increasing WLA resistance, R_{wla}. Efficiency improves for increasing power and decreasing $\bar{\delta}_s$, $\bar{\nu}$, and R_{wla}.

2.3.3 Thruster Design Considerations

We have analytically modeled a simplified DWDT concept and shown that in addition to J_a, the scaling of thrust and thrust efficiency depends on three important non-dimensional parameters: $\bar{\nu}$, $\bar{d}$, and $\bar{\delta}_s$. While the most straight-forward method for improving efficiency is to increase the total power, coupling and efficiency can be improved as $\bar{\nu}$, $\bar{d}$, and $\bar{\delta}_s \to 0$. Practically speaking, δ_s and d are difficult to decrease, as $\delta_s \sim n_e^{-1/2}$, and d is dependent on the amount of material insulating the WLA. Therefore, $\bar{d}$ and $\bar{\delta}_s$ are most easily controlled by increasing the physical size of the thruster, r_0. Finally, $\bar{\nu}$ can be easily minimized by increasing the applied angular frequency, ω.

2.4 Discussion

In this chapter, we have laid out a framework for analyzing the thrust and thrust efficiency of the DWDT concept. We start by modeling the momentum coupling between the wave-launching antenna structure and the plasma, along with any asso-

ciated energy losses. From this approach, we see that a DWDT will have a thrust proportional to the magnitude of the WLA current squared, J_a^2, and that efficiency of the momentum coupling will increase as current and power are increased. By analyzing a specific configuration and calculating thrust and loss coefficients, determined four design criterion for effective performance:

- The size of the device must be as large as the plasma length scales, $r_0 \geq \delta_s$.
- The size of the WLA must be larger than the stand-off distance, $r_0 > d$.
- The excitation frequency must be as large as the electron collision frequency, $\omega \geq \nu_e$.
- Resistive losses within the WLA must be minimized, $R_{\text{wla}} \to 0$.

A few key assumptions were made in our specific configuration that can change the calculated performance. First, by assuming an infinite extent plasma, we have artificially limited fringe effects. Second, by assuming a constant density plasma, we have ignored the wave-absorption dynamics that are likely to occur for various wave-modes. Finally, by choosing a linear, ordinary coupling to the plasma, we have ignored potential optimizations that may exist by targeting those specific wave-modes. Including these changes should not affect the J_a^2 scaling behavior; however, these assumptions must be relaxed in order to determine more precise scaling laws and design criteria.

Chapter 3

A DWDT using the Magnetosonic Mode[2]

A major step in the design of any DWDT is the selection of an appropriate wave-mode to target. While some previous work has focused on propagating electrostatic waves in the context of the ponderomotive thruster[30], these wave-modes are not necessarily an optimal design choice. In fact, various electrostatic[36, 37, 38] and electromagnetic[39, 51, 52] modes have been studied for their ability to generate high energy particles[31, 32, 33] and drive current flows[40, 40, 41]. In this chapter, we motivate the use of the magnetosonic or *fast* wave as an ideal mode for driving this type of accelerator. We then identify key parameters that govern the performance of the magnetosonic mode driven DWDT, including design criteria for a wave-dominated thruster channel, as well as the scaling of thrust.

To motivate the magnetosonic wave as particularly suited for plasma acceleration, we analyze how the wave phase velocity effects the potential performance of the accelerator and demonstrate that the magnetosonic mode can carry substantial

[2]This chapter is based on work previously presented in[50]: Feldman, M.S. and Choueiri, E.Y., "A Direct Wave-Drive Thruster using the Magnetosonic Mode," *34th International Electric Propulsion Conference*, IEPC-2015-115, Kobe, Japan, July 6-10, 2015.

momentum in Section 3.1. We use a mass continuity analysis in Section 3.2 to derive the critical powers required for wave-driven mass flow to exceed wall losses and other thermal effects. In Section 3.3, we layout an simple geometry for targeting the magnetosonic wave and calculate the scaling of the thrust coefficient as a function of the applied magnetic field strength, excitation frequency, and plasma density. In Section 3.4, we summarize our findings and discuss how these design considerations affect the design of our proof-of-concept experiment.

3.1 Why use the Magnetosonic Mode?

Relationship between Wave Phase Velocity and Thruster Exhaust Velocity

Before examining any specific mode, it is informative to consider how exhaust velocity is affected by the targeted wave. The exhaust velocity is a function of thrust and mass flow by

$$u_{ex} = T/\dot{m}, \tag{3.1}$$

and thrust power is

$$P_T = \frac{1}{2}\dot{m}u_{ex}^2 = \eta P. \tag{3.2}$$

Combining, we get well know result[1] that the thrust-to-power ratio is

$$\frac{T}{P} = \frac{2\eta}{u_{ex}}. \tag{3.3}$$

But the thrust and power of an efficient DWDT should be predominantly carried by the excited wave-mode(s). The total thrust is the channel cross-sectional area, A_{cs}, times the momentum flux density, and the total power is A_{cs} times the energy flux

density.

$$T = A_{cs}\dot{\mathcal{P}} \tag{3.4}$$

$$P = A_{cs}\dot{\mathcal{E}} \tag{3.5}$$

Therefore in an idealized thruster channel,

$$\frac{\dot{\mathcal{P}}}{\dot{\mathcal{E}}} = \frac{2\eta}{u_{ex}}. \tag{3.6}$$

Finally, a wave's momentum density and energy density are proportional to the wave number and frequency respectively[53, 54].

$$\mathcal{P} \sim \hbar k \tag{3.7}$$

$$\mathcal{E} \sim \hbar\omega \tag{3.8}$$

And we see that the predicted exhaust velocity is governed primarily by the phase velocity of the targeted wave mode.

$$u_{ex} \sim 2\eta\frac{\omega}{k} \sim v_\phi. \tag{3.9}$$

It is immediately apparent that in an efficient device, if the momentum and energy is carried primarily by the wave, the exhaust velocity will be of a similar order. Therefore, we should choose modes that have phase velocities near our targeted exhaust velocity.

Electric devices typically target exhaust velocities between 10-100 km/s[1, 2], though higher speeds might be desirable as more power becomes available. Modes that operate at these v_ϕ are generally those that target ion motion, such as ion acoustic and magnetosonic waves. And those modes which have easily varied phase velocities

could be particularly desirable in order to design variable impulse accelerators. Because the phase velocity of the magnetosonic mode can be controlled with the applied magnetic field strength, it is an appealing option to explore.

Electrostatic vs Magnetosonic Momentum Density

Both electrostatic and electromagnetic waves can reach and be tuned to phase velocities of interest, and as previously mentioned, both types of modes have been examined for their ability to drive plasma flows. However, these explorations have not focused on their overall suitability for an efficient propulsion device. In particular, if the momentum density carried by a wave is small, it may not be a suitable choice to target in a DWDT.

In an electrostatic wave, the restoring force responsible for propagation of the wave and its momentum is derived from the thermal energy within the system. Whereas for Alfvén waves, the magnetic lines of force provide the necessary restoring forces. In an electrostatic mode, the reliance on thermal energy for wave propagation limits the achievable performance. This is readily seen by comparing the momentum flux of the electrostatic ion cyclotron waves used by Jorns and Choueiri[30] to that carried by magnetosonic waves.

The momentum flux of a given wave is a product of the group velocity and the momentum density. In these waves, the momentum is primarily contained in the oscillating particles rather than the electromagnetic fields[53, 54]. Therefore, we can directly calculate the momentum density by time-averaging the particle motion. Considering the problem in one dimension and starting with the continuity equation:

$$\frac{\partial \rho}{\partial t} + \nabla(\rho v) = 0. \tag{3.10}$$

And using the standard linearization scheme

$$\rho = \rho_0 + \rho_1 e^{i(kx-\omega t)} \tag{3.11}$$

$$v = v_1 e^{i(kx-\omega t)} \tag{3.12}$$

we have

$$v_1 = \frac{\omega}{k}\frac{\rho_1}{\rho_0}. \tag{3.13}$$

The total time-averaged momentum density contained in the oscillating particles is

$$\mathcal{P} = \langle \rho v \rangle = \frac{1}{2}\rho_1 v_1 = \frac{1}{2}\frac{\rho_1^2}{\rho_0}\frac{\omega}{k}. \tag{3.14}$$

The phase and group velocities of the electrostatic ion cyclotron and magnetosonic waves can be calculated from their respective dispersion relations

$$\omega^2 = \Omega_i^2 + c_s^2 k^2, \tag{3.15}$$

$$\omega^2 = v_A^2 k^2 = \frac{B_0^2}{\mu_0 \rho_0} k^2. \tag{3.16}$$

Therefore the particle momentum flux, $\Gamma_{\mathcal{P}}$, for each wave is

$$\Gamma_{\mathcal{P}_{\mathrm{EIC}}} = \frac{1}{2}\frac{\rho_1^2}{\rho_0} c_s^2, \tag{3.17}$$

$$\Gamma_{\mathcal{P}_{\mathrm{MS}}} = \frac{1}{2}\frac{\rho_1^2}{\rho_0} v_A^2, \tag{3.18}$$

which can be simplified to

$$\Gamma_{\mathcal{P}_{\mathrm{EIC}}} = p_{\mathrm{th}} \frac{\rho_1^2}{\rho_0^2}, \tag{3.19}$$

$$\Gamma_{\mathcal{P}_{\mathrm{MS}}} = p_{\mathrm{B}} \frac{\rho_1^2}{\rho_0^2}. \tag{3.20}$$

Both waves transport momentum in proportion to the thermal or magnetic pressure associated with the driving restoration force. And for linear modes, $\rho_1/\rho_0 \ll 1$. As a result, the momentum flux for linear modes is necessarily limited by the pressure terms in Equations 3.19 and 3.20. For the linear electrostatic ion cyclotron waves explored by Jorns and Choueiri[30], this momentum must be smaller than the thermal pressure already present in the plasma. In order to reach a regime where the wave propagation dominates the momentum transfer, the wave must be highly non-linear, and the density rarefactions will be large compared to the background density. This average lower density may tend to result in worse coupling between the wave-launching antenna and the plasma.

However, the magnetosonic wave does not rely on thermal energy to propagate. With sufficiently large applied magnetic fields, this mode can carry significant momentum flux while remaining linear. Moreover, since we have direct control over the background magnetic strength and topology, we can tune the wave parameters to achieve the desired phase and exhaust velocities. This makes the magnetosonic wave ideal for driving a confined Direct Wave-Drive Thruster.

3.2 Criteria for a Wave-dominated Channel

In Chapter 2, we calculated the thrust and loss coefficients between a simple resistive plasma and an annular inductive antenna. However, this calculation ignored the propagating wave dynamics of the system that may limit performance. Not only must the WLA add momentum to the plasma, but this should be the dominant thrust contribution in an effective device. This can only reasonably be expected when the total mass flow within the thruster channel is primarily controlled by the driven waves. In the previous section, we made this assumption implicitly and ignored any thermally driven mass flow or losses to the channel walls. In this section, we will

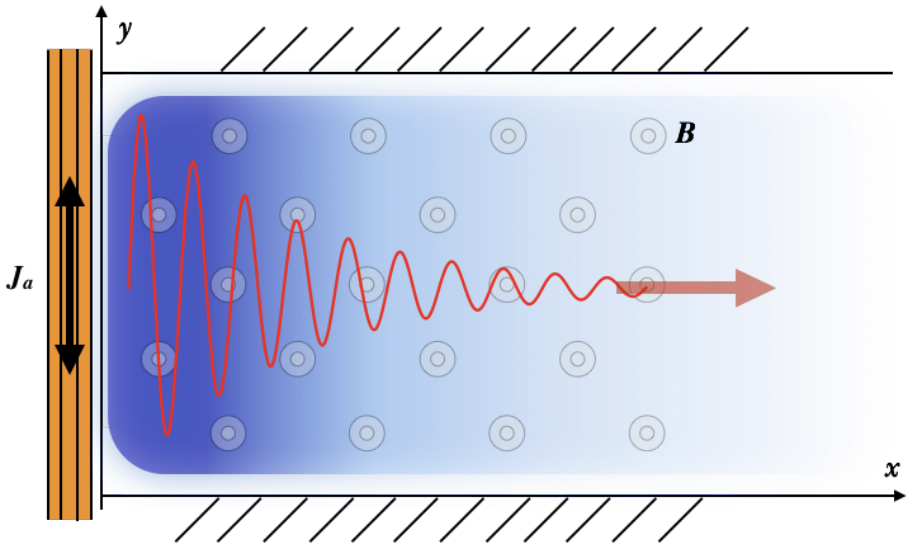

Figure 3.1: A Direct Wave-Drive Thruster Channel. Plasma is confined in a thruster channel by way of a background magnetic field. A wave-launching antenna structure is placed behind the channel, which generates a propagating mode in the positive $\hat{x}$-direction. In steady state, the propagating mode accelerates the plasma across field lines and out of the thruster.

derive simple requirements to create a wave-dominated channel for a DWDT using the magnetosonic mode.

We start by examining wave propagation in a channel where the assumption of wave-dominance is made a priori. We once again consider the simple 1D thruster channel shown in Figure 3.1, and assume that background magnetic field is constant and that wave propagation and thrust are purely in the $\hat{x}$-direction. We further assume that the plasma enters the channel such that the initial cold gas velocity is small compared to the propagating wave phase velocity. And finally, we ignore collisional processes that might reduce coupling efficiency.

In this case, the thruster dynamics are governed by three externally controllable parameters: the applied current in the WLA, J_a, the applied background magnetic field strength, B_0, and the total mass flow rate into the channel itself, $\dot{m}$. And we assume this mass flow is fully ionized as it enters the channel.

Assuming that the total thrust is simply the total momentum flux contained within the wave multiplied by the area of the channel, then from Equation 3.20 for the magnetosonic mode, we have

$$T = \Gamma_{\mathcal{P}} A_{cs} = \frac{B_0^2}{2\mu_0} \frac{\rho_1^2}{\rho_0^2} A_{cs}. \tag{3.21}$$

By linearizing the induction equation, $\frac{\partial B_z}{\partial t} = \frac{\partial}{\partial x}(vB_z)$, and combining with Equation 3.13, we get

$$\frac{B_1}{B_0} = \frac{\rho_1}{\rho_0}. \tag{3.22}$$

Together, Equations 3.20, 3.21, and 3.22 give

$$T = \Gamma_{\mathcal{P}} A = \frac{B_1^2}{2\mu_0} A_{cs}, \tag{3.23}$$

where the magnitude of B_1 is dependent on the coupling between the antenna and plasma and the controllable current in the WLA, J_a, such that

$$\frac{B_1^2}{2\mu_0} A_{cs} = C_{T_{\max}} \gamma J_a^2. \tag{3.24}$$

The wave-driven mass flow is

$$\dot{m}_{\text{wave}} = \Gamma_{\mathcal{M}} A_{cs} = \langle \rho v \rangle A = \frac{1}{2} \rho_1 v_1 A = \frac{1}{2} \frac{\rho_1^2}{\rho_0} \frac{B_0}{\sqrt{\mu_0 \rho_0}} A_{cs}. \tag{3.25}$$

Assuming the channel is wave-dominated, this accounts for all of the total mass flow into the system; $\dot{m} = \dot{m}_{\text{wave}}$. Therefore we can rewrite the plasma density as a function of B_1, B_0, and $\dot{m}$ by combining Equations 3.22 and 3.25. We get

$$\rho_0 = \frac{4\mu_0 B_0^2 \dot{m}^2}{B_1^4 A_{cs}^2}, \tag{3.26}$$

where the channel density increases with larger mass flow rates and background magnetic field strengths, but decreases with larger mode amplitudes.

While B_0 and $\dot{m}$ are directly controllable parameters, the mode amplitude, B_1, is not. Instead, it is dependent on the exciting current in the WLA and the theoretical coupling parameter, γ, through Equation 3.24. In a real system, γ may have complicated dependencies on collisional losses, the background density, and the wavelengths of the launched modes. However, we can determine important design criteria without a full calculation of γ by leaving the relevant equations dependent only on the amplitude of the wave-mode, B_1.

Since other mass transport effects are dependent on the density in the channel, we can use this expression to help determine what conditions are required for a wave-dominated channel to exist. To do this, we consider two other mechanisms responsible for mass flow in a real system: the cold gas flow and anisotropic wall losses across the confining magnetic field lines. We compare these to the wave-driven mass flow in order to create non-dimensional parameters which govern the system behavior.

For the first parameter, we note that in the absence of other effects, the thermally driven mass flow in the channel as a function of density ρ_0, thermal velocity, v_{th}, and channel size is

$$\dot{m}_{th} = A_{cs}\rho_0 v_{th}. \tag{3.27}$$

An effective DWDT should be designed so that this thermal mass flow is substantially less than the wave-driven mass flow,

$$\frac{\dot{m}_{\text{wave}}}{\dot{m}_{th}} \equiv \Pi_{th} \gg 1. \tag{3.28}$$

Combining Equations 3.25, 3.27, and 3.28, we have

$$\frac{B_1^2}{2\mu_0}\frac{\sqrt{\mu_0\rho_0}}{B_0} \cdot \frac{1}{\rho_0 v_{th}} \gg 1. \tag{3.29}$$

However, Equation 3.29 is not a function of externally controllable parameters, as ρ_0 is dependent on $\dot{m}$, B_0, and B_1 through Equation 3.26. Substituting in, we find a critical inequality dependent primarily on these controllable parameters (and the plasma temperature through the thermal velocity):

$$\Pi_{th} = \frac{B_1^4}{4\mu_0^2}\frac{2\mu_0}{B_0^2}\frac{A_{cs}}{2v_{th}\dot{m}} \gg 1. \tag{3.30}$$

The second condition requires that any mass flux to the walls also be small compared to the total wave-driven flow. This ratio,

$$\Pi_{\text{wall}} \equiv \frac{\dot{m}_{\text{wave}}}{\dot{m}_{\text{wall}}}, \tag{3.31}$$

is effectively an anisotropic Péclet number relating the cross-field diffusion to the walls to the wave-driven convection.

The wall flux is a function of the cross-field diffusion coefficient, the area of the channel walls, and the plasma density:

$$\dot{m}_{\text{wall}} = \rho_0 D_\perp A_{\text{wall}}/Y. \tag{3.32}$$

Here, Y is the separation distance between the channel walls, i.e., the effective distance over which cross-field diffusion must occur to reach the thruster walls. And we have a similar design criterion that

$$\Pi_{\text{wall}} = \frac{A_{cs}}{A_{\text{wall}}}\frac{B_1^2}{2\mu_0}\frac{\sqrt{\mu_0\rho_0}}{B_0}\frac{Y}{\rho_0 D_\perp} \gg 1. \tag{3.33}$$

Assuming classical cross-field diffusion[55, 56, 57],

$$D_\perp = \frac{p_e}{\sigma_e B_0^2}, \tag{3.34}$$

where $\sigma_e = \frac{e^2 n_e}{m_e \nu_e}$. And we combine to get the anisotropic Péclet number relating waves-driven mass flow to wall losses primarily as a function of our controllable parameters:

$$\Pi_{\text{wall}} = \frac{B_1^4}{4\mu_0^2} \frac{\mu_0 e^2}{m_e T_e \nu_e} \frac{Y A_{cs}^2}{\dot{m} A_{\text{wall}}} \gg 1. \tag{3.35}$$

But we note that we have not completely eliminated uncontrolled quantities, since the electron collision frequency is itself dependent on the plasma density.

Qualitatively, there is a minimum wave amplitude, B_1, for which the criteria given in Equations 3.30 and 3.35 are satisfied. This can be directly related to the total power in the propagating wave by noting that the wave energy flux is

$$\Gamma_{\mathcal{E}} = v_A \mathcal{E} = \frac{B_0}{\sqrt{\mu_0 \rho_0}} \frac{B_1^2}{2\mu_0}, \tag{3.36}$$

which can be solved in terms of our control parameters and the channel cross-sectional area:

$$\Gamma_{\mathcal{E}} = \frac{B_1^4}{4\mu_0^2} \frac{A_{cs}}{\dot{m}}. \tag{3.37}$$

Thus the total wave power is

$$P_{\text{wave}} = A_{cs} \Gamma_{\mathcal{E}} = \frac{B_1^4}{4\mu_0^2} \frac{A_{cs}^2}{\dot{m}}. \tag{3.38}$$

We briefly note that since $B_1 \sim J_a$ from Equation 3.24, the total power driven by the magnetosonic mode scales with J_a^4 consistent with our predictions in Chapter 2. This fourth-power scaling is the dominant mechanism that allows a DWDT to scale to higher efficiencies. But Equation 3.38 only applies when the mass-flow is predominately waves-driven. As a result, a DWDT must reach sufficient power to ensure this favorable scaling holds.

Finally, by combining Equations 3.30 and 3.35 with Equation 3.38, we generate two criteria for the total wave power necessary to ensure that the wave dynamics are

dominant. That is, $P_{\text{wave}} \gg P^*$, where

$$P^*_{\text{wall}} = \frac{m_e T_e \nu_e}{\mu_0 e^2} \frac{A_{\text{wall}}}{Y}, \tag{3.39}$$

$$P^*_{th} = 2 v_{th} \frac{B_0^2}{2\mu_0} A_{cs}. \tag{3.40}$$

3.3 Thrust Scaling in a Magnetosonically Powered DWDT

In Chapter 2, we calculated C_T and R_{eff} for the evanescing ordinary mode in an annular geometry. In this section, we will proceed along the same path to determine the thrust coefficient for a magnetosonic mode driven DWDT in a simplified linear geometry, which will help reveal important nondimensional parameters that govern the antenna-plasma coupling.

3.3.1 C_T Derivation in a Linear Geometry

The idealized geometry, shown in Figure 3.2, is uniform and infinite in the $\hat{y}$-direction. A constant background magnetic field is applied in the $\hat{z}$-direction with magnitude B_0. The wave-launching antenna is located at the $x = 0$ plane with a width of $2H$ and current flowing in the $\hat{y}$-direction, oscillating with angular frequency ω and magnitude J_a. The current return path for the WLA is located at $x = -l$. A semi-infinite slab of plasma is located at $x > d$ with density ρ_0. Additionally, we relax some of the constraints from our previous analysis to allow electromagnetic modes to propagate both inside and outside the plasma. In this configuration, the perturbing magnetic field from the WLA is predominantly parallel to B_0.

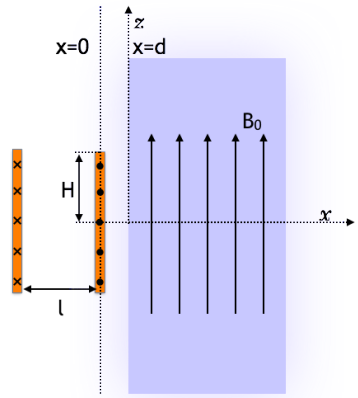

Figure 3.2: Simplified magnetosonic mode driven DWDT geometry. A semi-infinite plasma slab is placed at $x > d$ in a constant background magnetic field, $B_0\hat{z}$. A wave-launching antenna is located at $x = 0$ with a height, $2H$, in the $\hat{z}$-direction, and a total current in the $\hat{y}$-direction oscillating with frequency, ω, and magnitude, J_a. The current return path for the WLA is located at $x = -l$. The geometry is assumed to be uniform and infinite in the $\hat{y}$-direction.

We calculate the total electromagnetic fields as before by recalling the wave equation for the magnetic vector potential,

$$\nabla^2 \mathbf{A} = \frac{1}{c^2}\frac{\partial^2}{\partial t^2}\mathbf{A} + \mu_0 \sigma_\omega \cdot \frac{\partial}{\partial t}\mathbf{A}. \tag{3.41}$$

Unlike in Chapter 2, we have included the second derivative with respect to time, which has little effect on the propagating plasma mode, but allows vacuum electromagnetic modes to propagate. In our simplified geometry, $\mathbf{A}$ has components in only the $\hat{y}$-direction, and we can further reduce the equation with a Fourier transform in the time domain by assuming $\mathbf{A} = A_y e^{-i\omega t}$, such that

$$\nabla^2 A_y + \frac{\omega^2}{c^2}\epsilon_\perp A_y = 0. \tag{3.42}$$

In vacuum, the dielectric is unity, and inside the plasma at sufficiently low frequencies $\epsilon_\perp = 1 + \frac{c^2}{v_A^2}$.[58] Before solving, we will follow previous convention and nondimen-

sionalize the domain by the antenna half-width, H, and the excitation frequency, ω, such that

$$\bar{x} = \tfrac{x}{H} \qquad \bar{z} = \tfrac{z}{H} \qquad \bar{l} = \tfrac{l}{H} \qquad \bar{k}_v = \tfrac{\omega H}{c} \qquad \bar{k}_a = \tfrac{\omega H}{v_A}$$
$$\bar{A} = \tfrac{A}{\mu_0 J_a} \qquad \tau = \omega t \qquad \bar{\nabla} = H\nabla, \tag{3.43}$$

and Equation 3.42 becomes

$$\bar{\nabla}^2 \bar{A}_y + \bar{k}^2 \bar{A}_y = 0, \tag{3.44}$$

where

$$\bar{k}^2 = \begin{cases} \bar{k}_v^2 & \bar{x} < \bar{l} \\ \bar{k}_v^2 + \bar{k}_a^2 & \bar{x} > \bar{l} \end{cases}. \tag{3.45}$$

We solve Equation 3.44 by separation of variables into the $\hat{x}$ and $\hat{z}$ components of the excited wave-modes, and it is easy to see that the natural separation constant is simply the $\hat{z}$-directed wavenumber, k_z.

The full derivation for the spatial solution in the $\hat{\bar{x}} - \hat{\bar{z}}$ plane is in Appendix A.2 and follows techniques used in previous works[46, 47] and Chapter 2. The result is a piecewise solution across the four regions: behind the antenna, between the two antenna current paths, between the antenna and plasma, and in the plasma:

$$\bar{A}_{y1}(\bar{x}, \bar{z}, \bar{k}_v, \bar{k}_a, \bar{l}) = \int_0^\infty C_1 e^{-i\bar{k}_1 \bar{x}} \cos(\bar{k}_z \bar{z}) d\bar{k}_z, \tag{3.46}$$

$$\bar{A}_{y2}(\bar{x}, \bar{z}, \bar{k}_v, \bar{k}_a, \bar{l}) = \int_0^\infty (C_2 e^{i\bar{k}_1 \bar{x}} + C_3 e^{-i\bar{k}_1 \bar{x}}) \cos(\bar{k}_z \bar{z}) d\bar{k}_z, \tag{3.47}$$

$$\bar{A}_{y3}(\bar{x}, \bar{z}, \bar{k}_v, \bar{k}_a, \bar{l}) = \int_0^\infty (C_4 e^{i\bar{k}_1 \bar{x}} + C_5 e^{-i\bar{k}_1 \bar{x}}) \cos(\bar{k}_z \bar{z}) d\bar{k}_z, \tag{3.48}$$

$$\bar{A}_{y4}(\bar{x}, \bar{z}, \bar{k}_v, \bar{k}_a, \bar{l}) = \int_0^\infty C_6 e^{i\bar{k}_2 \bar{x}} \cos(\bar{k}_z \bar{z}) d\bar{k}_z, \tag{3.49}$$

where

$$\bar{k}_1 = \sqrt{\bar{k}_v^2 - \bar{k}_z^2}, \tag{3.50}$$

$$\bar{k}_2 = \sqrt{\bar{k}_v^2 + \bar{k}_a^2 - \bar{k}_z^2}. \tag{3.51}$$

k_1 and k_2 are the $\hat{x}$-directed wavenumbers of the various modes in vacuum and in the plasma respectively. The coefficients, C_i, are derived in Appendix A.2:

$$C_1 = \frac{1}{2\pi i}\frac{\sin\bar{k}_z}{\bar{k}_z}\frac{1}{\bar{k}_1}\left(1 - e^{i\bar{k}_1\bar{l}}\right)\left(1 + \frac{\bar{k}_1 - \bar{k}_2}{\bar{k}_1 + \bar{k}_2}e^{2i\bar{k}_1 d}\right) \tag{3.52}$$

$$C_2 = -\frac{1}{2\pi i}\frac{\sin\bar{k}_z}{\bar{k}_z}\frac{1}{\bar{k}_1}e^{i\bar{k}_1\bar{l}} \tag{3.53}$$

$$C_3 = \frac{1}{2\pi i}\frac{\sin\bar{k}_z}{\bar{k}_z}\frac{1}{\bar{k}_1}\left(1 + \frac{\bar{k}_1 - \bar{k}_2}{\bar{k}_1 + \bar{k}_2}\left(1 - e^{i\bar{k}_1\bar{l}}\right)e^{2i\bar{k}_1 d}\right) \tag{3.54}$$

$$C_4 = \frac{1}{2\pi i}\frac{\sin\bar{k}_z}{\bar{k}_z}\frac{1}{\bar{k}_1}\left(1 - e^{i\bar{k}_1\bar{l}}\right) \tag{3.55}$$

$$C_5 = \frac{1}{2\pi i}\frac{\sin\bar{k}_z}{\bar{k}_z}\frac{1}{\bar{k}_1}\frac{\bar{k}_1 - \bar{k}_2}{\bar{k}_1 + \bar{k}_2}\left(1 - e^{i\bar{k}_1\bar{l}}\right)e^{2i\bar{k}_1 d} \tag{3.56}$$

$$C_6 = \frac{1}{\pi i}\frac{\sin\bar{k}_z}{\bar{k}_z}\frac{1}{\bar{k}_1 + \bar{k}_2}\left(1 - e^{i\bar{k}_1\bar{l}}\right)e^{i(\bar{k}_1 - \bar{k}_2)d} \tag{3.57}$$

Instead of integrating the total electromagnetic pressure on the plasma surface, we calculate the total thrust by integrating the $\boldsymbol{J} \times \boldsymbol{B}$ forces directly on the WLA surface. Again assuming that little momentum is lost by radiation to vacuum, this will exactly equal the total force on the plasma. Since we are only concerned with the $\hat{x}$-directed force, and the WLA-currents are solely in the $\hat{y}$-direction, we are concerned with B_z, which can be obtained from the vector potential via:

$$B_{zi} = \frac{\partial A_{yi}}{\partial x}, \tag{3.58}$$

where i is the region of the solution space.

However, we note that mathematically, the magnetic field experiences a jump discontinuity about the current paths in the antenna. That is, $B_{z1}|_{x=-l} \neq B_{z2}|_{x=-l}$, and $B_{z2}|_{x=0} \neq B_{z3}|_{x=0}$. The correct magnetic field to use is the average of the two values at the antenna surface. However, we can simplify the problem via superposition. First, we solve for the magnetic field in the absence of a plasma to push on. In this situation, the only forces on the antenna surfaces are generated by the antenna on itself and therefore do not contribute to the total thrust. Second, we solve for the magnetic field with the plasma present. The difference in these calculated values represents the total magnetic field that contributes to thrust. This difference is effectively the strengths of the reflected wave-modes from the plasma surface as the waves are launched. As a result, this field is continuous across the antenna surfaces, and there is no longer a discontinuity to be addressed.

The magnetic field in the $\hat{z}$-direction in the presence of a plasma to push on is

$$B_{z1} = \frac{\mu_0 J_a}{H} \int_0^\infty -i\bar{k}_1 C_1 e^{-i\bar{k}_1\bar{x}} \cos(\bar{k}_z\bar{z}) d\bar{k}_z, \tag{3.59}$$

$$B_{z2} = \frac{\mu_0 J_a}{H} \int_0^\infty i\bar{k}_1 (C_2 e^{i\bar{k}_1\bar{x}} - C_3 e^{-i\bar{k}_1\bar{x}}) \cos(\bar{k}_z\bar{z}) d\bar{k}_z, \tag{3.60}$$

$$B_{z3} = \frac{\mu_0 J_a}{H} \int_0^\infty i\bar{k}_1 (C_4 e^{i\bar{k}_1\bar{x}} - C_5 e^{-i\bar{k}_1\bar{x}}) \cos(\bar{k}_z\bar{z}) d\bar{k}_z, \tag{3.61}$$

$$B_{z4} = \frac{\mu_0 J_a}{H} \int_0^\infty i\bar{k}_2 C_6 e^{i\bar{k}_2\bar{x}} \cos(\bar{k}_z\bar{z}) d\bar{k}_z. \tag{3.62}$$

And we care about the magnetic field at WLA surfaces, $x = -l$ and $x = 0$, so we examine B_z in region 2. In this region at the the forward (f) and return (r) current

surfaces of the WLA, we have

$$B_r = B_{z2}|_{x=-l} =$$
$$\frac{\mu_0 J_a}{H}\int_0^\infty \frac{1}{2\pi}\frac{\sin\bar{k}_z}{\bar{k}_z}\Big(-1-e^{i\bar{k}_1\bar{l}}-\frac{\bar{k}_1-\bar{k}_2}{\bar{k}_1+\bar{k}_2}\big(1-e^{i\bar{k}_1\bar{l}}\big)e^{2i\bar{k}_1 d}e^{i\bar{k}_1\bar{l}}\Big)\cos(\bar{k}_z\bar{z})d\bar{k}_z \quad (3.63)$$

$$B_f = B_{z2}|_{x=0} =$$
$$\frac{\mu_0 J_a}{H}\int_0^\infty \frac{1}{2\pi}\frac{\sin\bar{k}_z}{\bar{k}_z}\Big(-e^{i\bar{k}_1\bar{l}}-1-\frac{\bar{k}_1-\bar{k}_2}{\bar{k}_1+\bar{k}_2}\big(1-e^{i\bar{k}_1\bar{l}}\big)e^{2i\bar{k}_1 d}\Big)\cos(\bar{k}_z\bar{z})d\bar{k}_z. \quad (3.64)$$

In the absence of a plasma, $k_1 = k_2$, and these fields become

$$B_{r_v} = \frac{\mu_0 J_a}{H}\int_0^\infty \frac{1}{2\pi}\frac{\sin\bar{k}_z}{\bar{k}_z}\big(-1-e^{i\bar{k}_1\bar{l}}\big)\cos(\bar{k}_z\bar{z})d\bar{k}_z, \quad (3.65)$$

$$B_{f_v} = \frac{\mu_0 J_a}{H}\int_0^\infty \frac{1}{2\pi}\frac{\sin\bar{k}_z}{\bar{k}_z}\big(-e^{i\bar{k}_1\bar{l}}-1\big)\cos(\bar{k}_z\bar{z})d\bar{k}_z. \quad (3.66)$$

And the differences in the magnetic field strengths with and without a plasma represent the total magnetic field that contributes to thrust.

$$\Delta B_r = \frac{\mu_0 J_a}{H}\int_0^\infty \frac{1}{2\pi}\frac{\sin\bar{k}_z}{\bar{k}_z}\Big(-\frac{\bar{k}_1-\bar{k}_2}{\bar{k}_1+\bar{k}_2}\big(1-e^{i\bar{k}_1\bar{l}}\big)e^{2i\bar{k}_1 d}e^{i\bar{k}_1\bar{l}}\Big)\cos(\bar{k}_z\bar{z})d\bar{k}_z \quad (3.67)$$

$$\Delta B_f = \frac{\mu_0 J_a}{H}\int_0^\infty \frac{1}{2\pi}\frac{\sin\bar{k}_z}{\bar{k}_z}\Big(-\frac{\bar{k}_1-\bar{k}_2}{\bar{k}_1+\bar{k}_2}\big(1-e^{i\bar{k}_1\bar{l}}\big)e^{2i\bar{k}_1 d}\Big)\cos(\bar{k}_z\bar{z})d\bar{k}_z \quad (3.68)$$

Finally, we note that the current is negative along the reverse path, and that the total force on the antenna will be in the negative $\hat{x}$-direction, corresponding to positive thrust. Additionally, we integrate over a fixed distance in the $\hat{y}$-direction, Y, while maintaining the uniform assumption and neglecting fringe effects. And we get

thrust from time-averaging the real components of the $\boldsymbol{J} \times \boldsymbol{B}$ product. i.e.,

$$T = \left\langle \int_0^Y dy \cdot \frac{1}{2H} \int_{-H}^{H} \mathrm{Re}[J_a] \cdot \mathrm{Re}[\Delta B_r - \Delta B_f] dz \right\rangle \tag{3.69}$$

Putting it together and integrating in the normalized coordinates, the total thrust is

$$T = \frac{1}{8}\mu_0 J_a^2 \int_0^{\bar{Y}} d\bar{y} \int_0^{\infty} \frac{2}{\pi}\left(\frac{\sin \bar{k}_z}{\bar{k}_z}\right)^2 \mathrm{Re}\left[\left(1 - e^{i\bar{k}_1\bar{l}}\right)^2 e^{2i\bar{k}_1\bar{d}} \frac{\bar{k}_2 - \bar{k}_1}{\bar{k}_2 + \bar{k}_1}\right] d\bar{k}_z. \tag{3.70}$$

And without the normalization scheme, we have

$$T = \frac{1}{8}\mu_0 J_a^2 \int_0^{Y} dy \int_0^{\infty} \frac{2}{\pi}\left(\frac{\sin k_z H}{k_z H}\right)^2 \mathrm{Re}\left[\left(1 - e^{ik_1 l}\right)^2 e^{2ik_1 d} \frac{k_2 - k_1}{k_2 + k_1}\right] dk_z. \tag{3.71}$$

We can define thrust in terms of a maximum possible force and a coupling coefficient, γ, in the same manner as Chapter 2.

$$T = \frac{1}{8}\mu_0 J_a^2 \frac{Y}{H} \cdot \gamma(\bar{k}_a, \bar{k}_v, \bar{l}, \bar{d}), \tag{3.72}$$

where

$$\gamma(\bar{k}_a, \bar{k}_v, \bar{l}, \bar{d}) = \int_0^{\infty} \frac{2}{\pi}\left(\frac{\sin \bar{k}_z}{\bar{k}_z}\right)^2 \mathrm{Re}\left[\left(1 - e^{i\sqrt{\bar{k}_v^2 - \bar{k}_z^2}\bar{l}}\right)^2 e^{2i\sqrt{\bar{k}_v^2 - \bar{k}_z^2}\bar{d}} \frac{\sqrt{\bar{k}_v^2 + \bar{k}_a^2 - \bar{k}_z^2} - \sqrt{\bar{k}_v^2 - \bar{k}_z^2}}{\sqrt{\bar{k}_v^2 + \bar{k}_a^2 - \bar{k}_z^2} + \sqrt{\bar{k}_v^2 - \bar{k}_z^2}}\right] d\bar{k}_z, \tag{3.73}$$

and γ has a maximum of 1.

3.3.2 Interpretation of Thrust Coefficient

Unlike in the annular solution described in Chapter 2, the equations derived here for T and γ are easier to interpret, and understanding each term helps elucidate the relevant physics. Just like in the annular characterization, the maximum thrust, $T_{\max} = {}^{1}\!/_{8}\mu_0 J_a^2 \bar{Y}$, is equivalent to the maximum magnetic pressure exerted between two infinitely close current sheets. The rest of the coupling coefficient can be understood from the geometry of the antenna structure and the reflection of the vacuum wave-mode propagating from the antenna to the plasma.

Antenna Shape

The first term, ${}^{\sin \bar{k}_z}\!/_{\bar{k}_z}$, is the Fourier decomposition of the WLA's shape in the $\hat{z}$-direction. If the WLA consisted of an infinite, sinusoidal structure with a fixed wavenumber, it would generate one k_z of interest. For our WLA, the shape is a step-up and step-down, described by $\Theta(\bar{z}+1) - \Theta(\bar{z}-1)$, where Θ is the Heaviside function. And its Fourier transform is simply:

$$\mathcal{F}(\Theta(\bar{z}+1) - \Theta(\bar{z}-1)) = \sqrt{\frac{2}{\pi}} \frac{\sin \bar{k}_z}{\bar{k}_z}. \tag{3.74}$$

Stand-off Distance

The term dependent on $\bar{d}$ describes how the wave-modes are altered by the stand-off distance. The exponent, $i\sqrt{\bar{k}_v^2 - \bar{k}_z^2}\bar{d}$, controls either the phase or evanescence of the vacuum mode between the WLA and plasma. If $\bar{k}_v > \bar{k}_z$, the exponent is imaginary and the mode is simply phase-shifted. However, we are primarily interested in configurations where $\bar{k}_v$ is small, which is identical to the low frequency assumption made in Chapter 2 and physically equivalent to the assumption that the wavelengths associated with the excitation frequency in vacuum are large compared to the geometry

of the system. In this case, the exponent simply becomes $-2\bar{k}_z\bar{d}$. And as should be expected, the coupling decreases as the stand-off distance becomes large.

Current Return Path

The $\bar{l}$-dependent term essentially includes the effects of the current return path. The negative sign is due to the fact that the return path has current flowing in the reverse direction. Like above, if $\bar{k}_v$ is sufficiently large, than the launched mode is phase-shifted, and when $\bar{k}_v$ is small, we get $1 - e^{-\bar{k}_z\bar{l}}$. When $l = 0$, the two current paths are coincident and cancel, and therefore no thrust in generated. It's immediately apparently that the reverse path can dramatically limit the total coupling. This effect becomes particularly important in Chapter 5 as we analyze the experimental wave-launching antenna, since it limits the overall performance of the system.

Plasma Interaction

Finally, we examine the only term that explicitly includes the plasma interaction,

$$\frac{\sqrt{\bar{k}_v^2 + \bar{k}_a^2 - \bar{k}_z^2} - \sqrt{\bar{k}_v^2 - \bar{k}_z^2}}{\sqrt{\bar{k}_v^2 + \bar{k}_a^2 - \bar{k}_z^2} + \sqrt{\bar{k}_v^2 - \bar{k}_z^2}} = \frac{k_2 - k_1}{k_2 + k_1}. \tag{3.75}$$

This is essentially a reflection coefficient. As the plasma density decreases and becomes closer to vacuum, $k_2 \to k_1$, the term becomes small, and there is no reflection of the propagating or evanescing wave modes. However, for sufficiently small wavelengths of propagation within the plasma, $k_2 \gg k_1$, and the term becomes close to unity. Essentially, in order to launch high momentum-to-energy-ratio wave-modes within the plasma, most of the vacuum mode must be reflected at the plasma surface.

It is important to note that the reflected energy is not wasted and therefore does not become a source of inefficiency. When $\bar{k}_v$ is small, the reflected mode is primarily out of phase with the corresponding mode originally launched by the WLA in the

negative $\hat{x}$-direction. As a result, the two modes cancel and there is little associated energy loss. However, when $\bar{k}_v$ becomes large, these modes will not precisely cancel, and instead the reflected energies will be propagate into vacuum, which results in a larger R_{rad} and smaller efficiency.

3.3.3 Parametric Investigation of C_T

It is easy to see how each term effects γ. For small $\bar{k}_v$, as $\bar{d}$ becomes small and $\bar{l}$ becomes large, their respective terms go to unity. This makes physical sense, since as the stand-off length becomes large, coupling should decrease, and as the WLA current return path is moved closer to the forward path, it should tend to counteract the forward current. Finally, as k_a becomes large corresponding to smaller wavelengths, the reflection coefficient goes towards unity as well, and the thrust is maximized. Figure 3.3 shows plots of γ for varying $\bar{k}_a$, $\bar{d}$, and $\bar{l}$, assume small $\bar{k}_v$.

3.4 Chapter Summary

In this chapter, we have motivated the magnetosonic wave as a strong candidate for powering a DWDT, and derived critical power requirements in order to achieve a wave-dominated thruster channel as well as the scaling of the thrust coefficient. We first showed that in an effective DWDT, u_{ex} is comparable to v_ϕ of the targeted wave-mode, which suggests that a DWDT should target waves based on ion motion, such as the magnetosonic wave. Furthermore, we showed that these modes are capable of carrying significant momentum compared to electrostatic waves.

In order to characterize under what conditions the thruster channel may be wave-dominated, we derived Péclet numbers comparing the mass flow due to wave advection against the mass transport due to diffusion and thermal effects. These criteria were

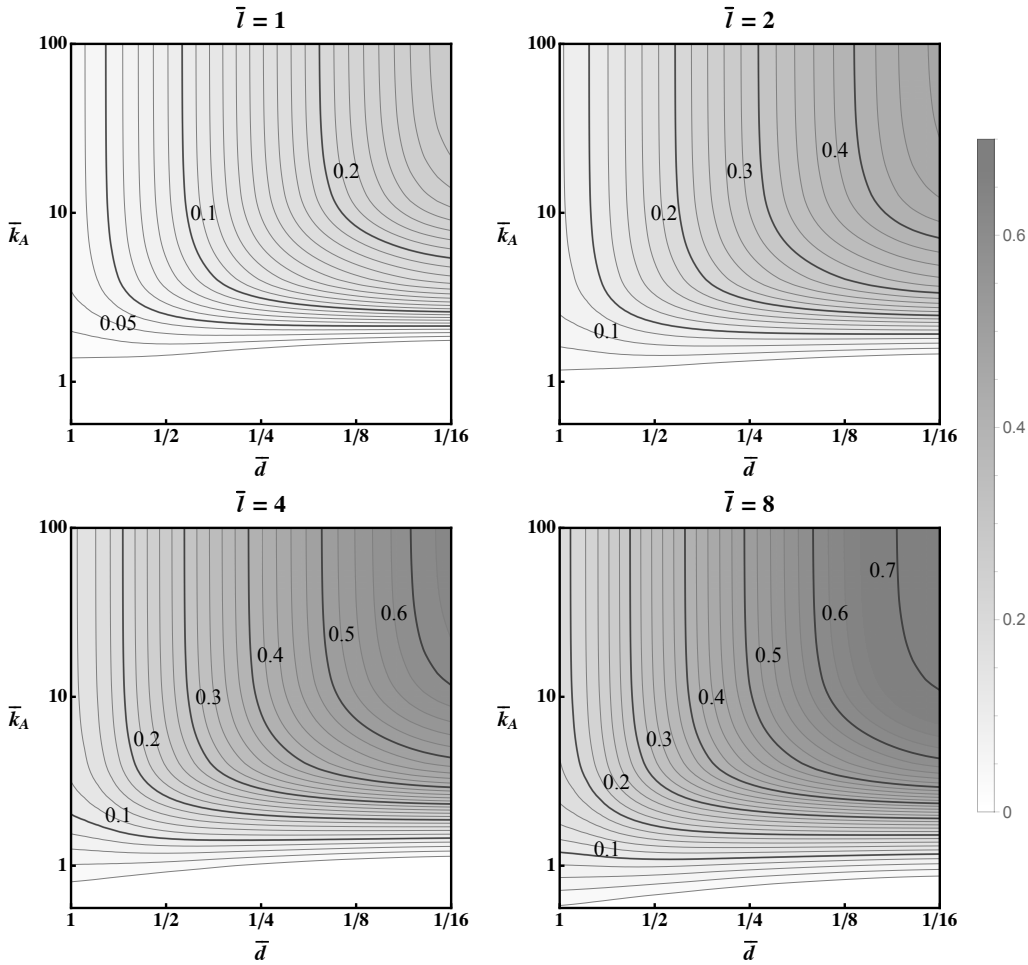

Figure 3.3: γ vs. $\bar{k}_a$, $\bar{d}$, $\bar{l}$. Contour plots of the coupling parameter, γ, with respect to the normalized magnetosonic wavenumber, $\bar{k}_a$ and thenormalized stand-off lengths, $\bar{d}$, for various normalized current-path separation lengths, $\bar{l}$. Coupling (and therefore the total thrust coefficient), decrease for smaller wavenumbers. Coupling improves for larger wavenumbers and reaches a maximum dependent on $\bar{d}$ and $\bar{l}$.

used to derive the total power required to reach wave-dominated flow within the thruster channel.

We then calculated C_T for a simple, linear geometry. This derivation shows that the WLA-plasma coupling is strongly dependent on, $\bar{k}_a$, the ratio of the magnetosonic wavelength to the size of the thruster, and the coupling is uniform and maximized in the limit where $\bar{k}_a \gg 1$. Additionally, of particular importance is the effect of the current return path on C_T. In the linear geometry described in this chapter, the return path is necessary and dramatically reduces the total momentum coupling

unless it is far from the forward current path. However, this effect is not present in an annular geometry, such as the one described in Chapter 2. In that case, no return path is necessary and all current paths can be located adjacent to the plasma. As a result, the linear configuration described is not ideal for optimizing a DWDT.

Chapter 4

Experimental Setup and Diagnostics

The goal of our experimentation is to investigate the fundamental scaling behavior described in Chapters 2 and 3. In particular, we wish to validate predictions for plasma acceleration as a function of controllable parameters, such as the targeted frequency or applied background magnetic field. We are not yet concerned with the construction of an optimized thruster, and so the design and construction of the Direct Wave-Drive Thruster Proof-of-Concept Experiment is done to most easily validate predictions rather than maximize thrust and efficiency. This chapter provides a technical overview of the experiment used to validate these predictions as well as a characterization of the operating conditions of the plasma source.

The Direct Wave-Drive Thruster Experiment (DWDTX) consists of a plasma generation stage and an acceleration stage, along with the exhaust plume diagnostics. Two major design considerations simplify both the construction and modeling of the DWDTX. First, we separate the plasma generation and acceleration to isolate the coupling between the wave-launching antenna (WLA) and the plasma. Second, unlike the model in Chapter 2, the DWDTX geometry is linear, similar to the model used

in Chapter 3. Figure 4.1 shows a full CAD model (2D and 3D) of the experiment, including the plasma source, confining magnetic fields, and wave-launching antenna. The physical experiment mounted in the EPPDyL's "Orange Vacuum Tank" is shown in Figure 4.2. Finally, a full schematic overview of the system infrastructure is shown in Figure 4.3.

In Section 4.1, we describe the vacuum system and each of the physical components required to generate, confine, and accelerate the plasma. In Section 4.2, we discuss the various diagnostics used in our experimentation. Finally, we characterize the source plasma in Section 4.3.

4.1 Experimental Set-Up

4.1.1 Plasma Source

The plasma source consists of all the hardware necessary to create and confine the plasma to be accelerated. While a real thruster will likely require blending or combining the plasma creation and acceleration mechanisms (such as similar attempts for PITs[59]), we are primarily concerned with validating our theoretical model, rather than optimizing thruster design. This is most easily done by separating out the plasma generation process. This reduces the complexity of the coupling to the WLA, and it allows us to independently control the plasma density aside from the WLA input power and frequency.

To simplify the analytical modeling and system complexity, we construct the experiment in a linear geometry, and the DWDTX source is essentially a linear magnetic bottle. It consists of a a 8 cm diameter glass tube with an 8 cm x 8 cm exhaust hole centered on the tube. This exhaust hole is bracketed by two water-cooled electromagnets, forming the magnetic bottle. Each end of the glass tube is closed by a Macor backplate. Argon gas is fed though each backplate via an alumina gas injec-

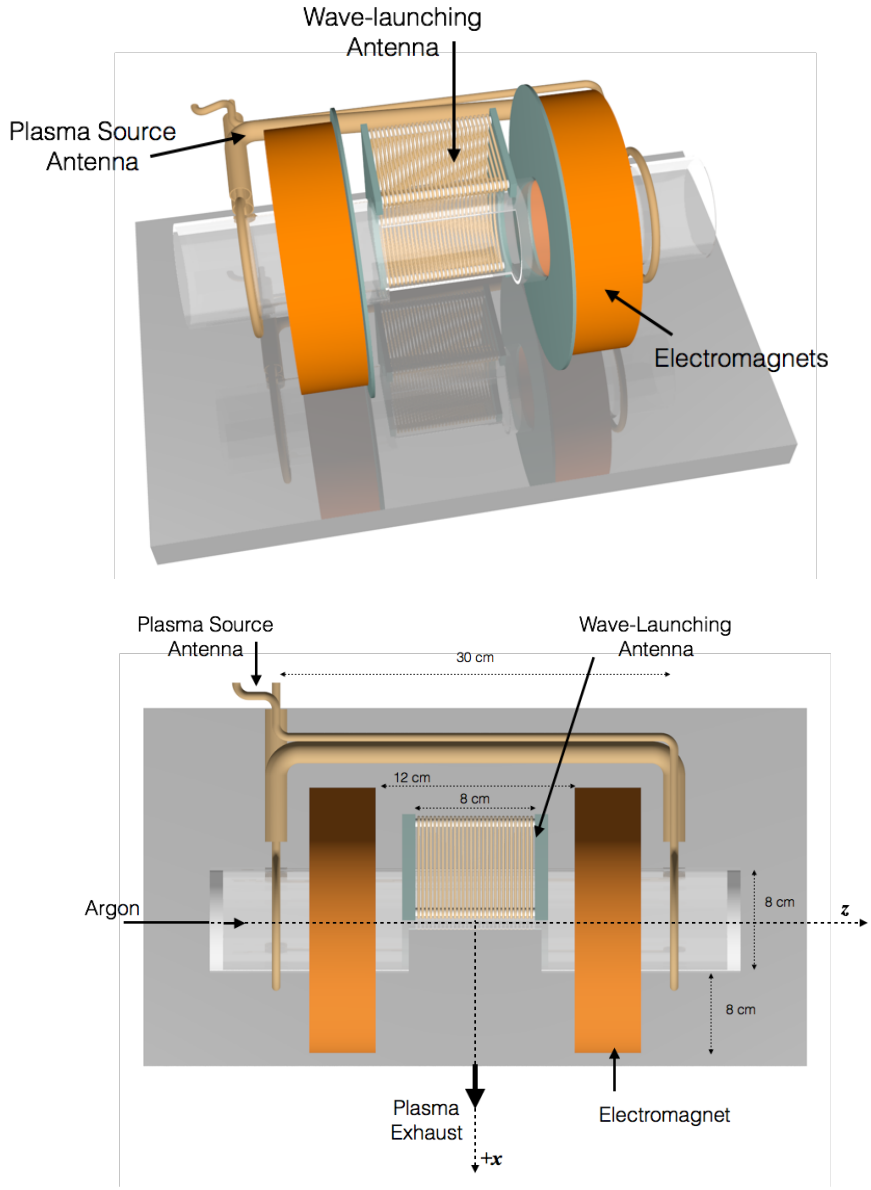

Figure 4.1: The Direct Wave-Drive Thruster Experiment (DWDTX) POVRay Model. Top: Perspective. Bottom: Overhead Orthographic. The DWDT experiment is mounted in the EPPDyL's "Orange" Vacuum Tank. It consists of a confining glass tube with an exhaust hole centered between two electromagnets (in orange), which creates a magnetic bottle. Gas is injected from either side of the tube and a plasma is created using a 13.56 Mhz RF signal by the two copper loop antennas bracketing the electromagnets. The WLA is center mounted behind the exhaust hole. G10 plates (shown in green) isolate the electromagnets from direct exposure to the plume. Not pictured are two Macor backplates which seal the open ends of the tube, through which argon gas is injected.

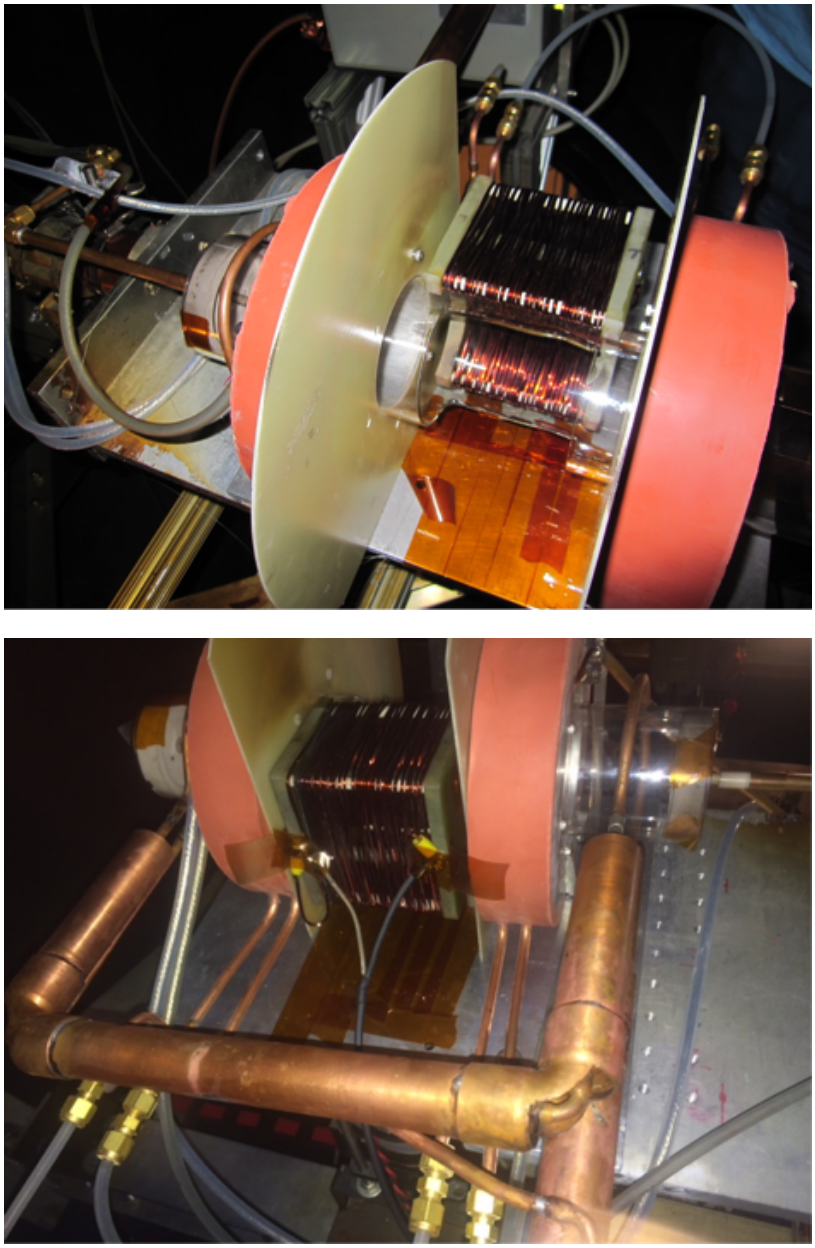

Figure 4.2: Direct Wave-Drive Thruster Experiment Front (top) and Back (bottom) View. The electromagnets are the red cylinders bracketing the centered WLA. Two large G10 plates protect the magnets from the plasma plume. The plasma generating antenna loops around the glass cylinder outside of the two electromagnets.

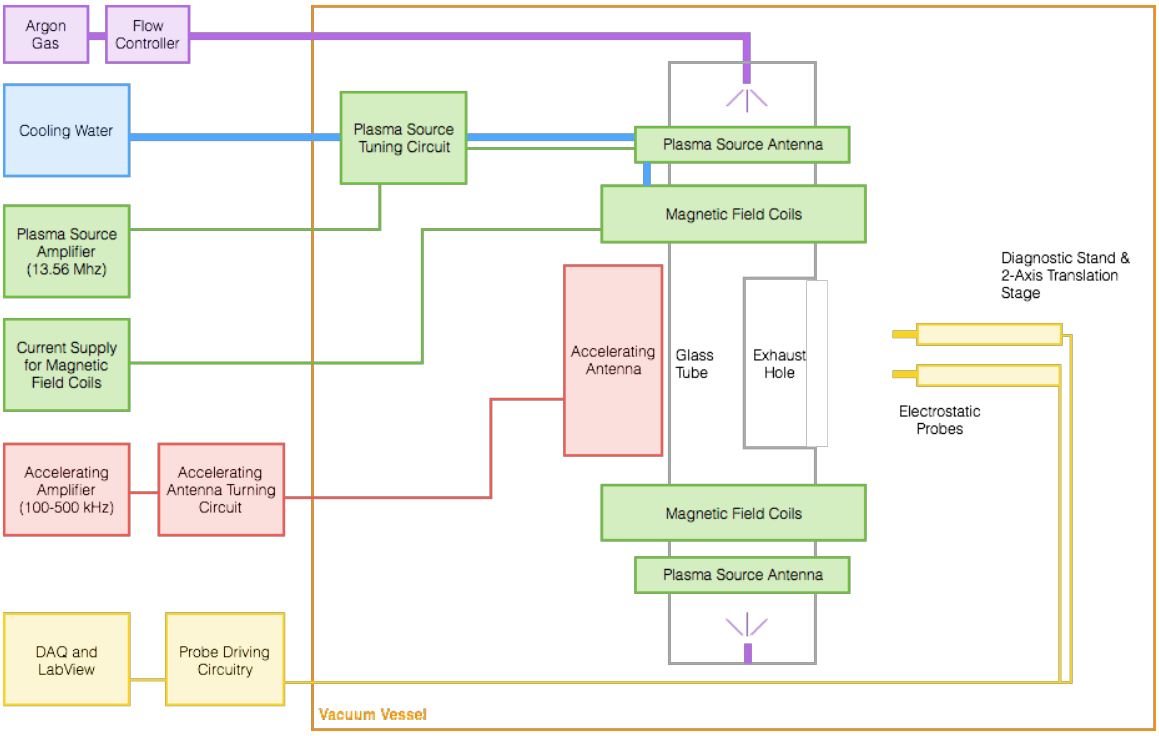

Figure 4.3: Direct Wave-Drive Thruster Experiment System Overview. GREEN: Plasma Source Generation Components. RED: Plasma Acceleration Components. YELLOW: Diagnostics.

tion tube. The plasma source antenna (PSA) consists of two single loop antennas[60] made from 1/4" copper tubing, connected in series, and positioned outside of the two electromagnets, encircling the glass tube. Therefore, plasma is generated outside the magnets and is allowed to flow into the center region along the confining magnetic field lines.

Magnetic Field Coils

The confining magnetic bottle is created by two identical electromagnets spaced roughly 12 cm apart. These coils were originally constructed for magnetic nozzle experiments[56, 61] and repurposed for the DWDTX. Each coil consists of 144 loops of square magnet wire wrapped in a 12x12 grid. To cool each magnet, we added two loops of 1/4-inch copper tubing wrapped around the outer edge and potted the wires and cooling lines in a thermally conductive resin[62]. A CAD model of an individual electromagnet and cooling line is shown in Figure 4.4.

The magnets are spaced wider than a typical Helmholtz configuration in order to accommodate the WLA, and so the field lines are not precisely uniform. We define

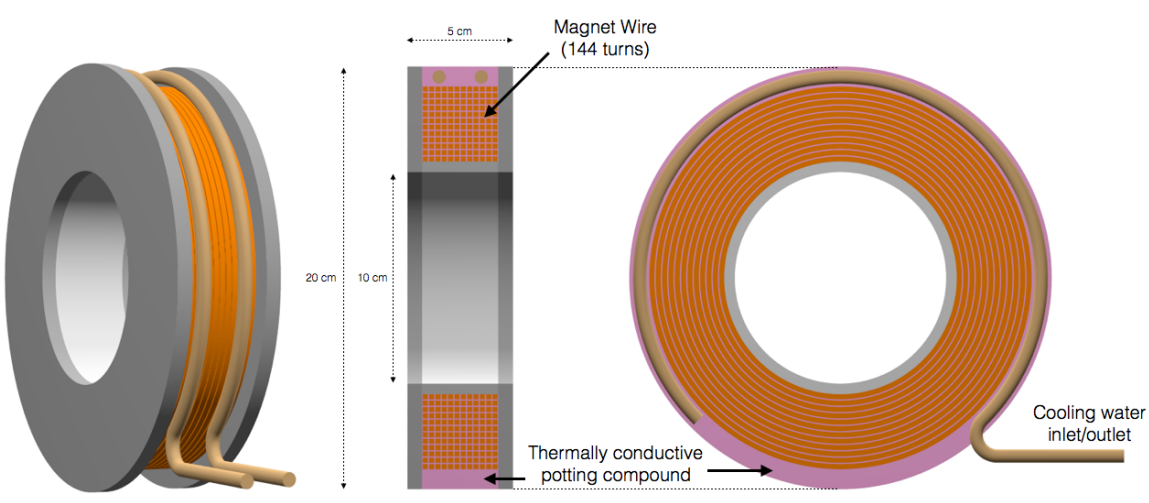

Figure 4.4: DWDTX Electromagnet. Left: Perspective without thermal compound to visualize water-cooling lines. Right: Orthographic slices showing electromagnet internals.

B_0 as the magnetic field strength at the center of the bottle configuration, half-way between the two magnets. To see the deviation from uniformity in the magnetic field, we plot magnetic field streamlines of the 2D field in the $\hat{r} - \hat{z}$ plane within the confining glass tube. Figure 4.5 shows that the field strength deviates 10% over the region of interest. Figure 4.6 shows the field strength along the centerline of the glass tube for various applied currents.

Plasma Source Antenna

The plasma is generated using a dual-loop source antenna (Figure 4.7) operated at 13.56 MHz. Each loop encircles the outer ends of the glass tube, as shown in Figure 4.1, and the loops are arranged in series to ensure roughly equal power to each side of the system. The antenna structure is formed from 1/4-inch copper tubing so it can be directly water-cooled. The outer-conductor is 1-1/8-inch copper tubing. The 13.56 MHz signal enters the vacuum chamber and then is matched to the antenna via a capacitive L-Network[63], shown in Figure E.1. Plasma is generated primarily at the center of each loop and then flows through the electromagnets to the center of the system. Figure 4.8 shows argon gas entering the system and being excited by the PSA, and the full plasma structure of the source is shown in Figures 4.18 and 4.19.

4.1.2 Acceleration Stage and the Wave-Launching Antenna

The main feature of any Direct Wave-Drive Thruster is the wave-launching antenna that accelerates the plasma. Our WLA is centered between the two electromagnets, directly behind the exhaust hole. The WLA is designed to target the fast wave both because of the beneficial characteristics described in Chapter 3 and because it allows us to control the plasma coupling by varying the background magnetic field strength. As a result, the current paths of the antenna must be perpendicular to the applied magnetic field to target these modes. Furthermore, the antenna is designed

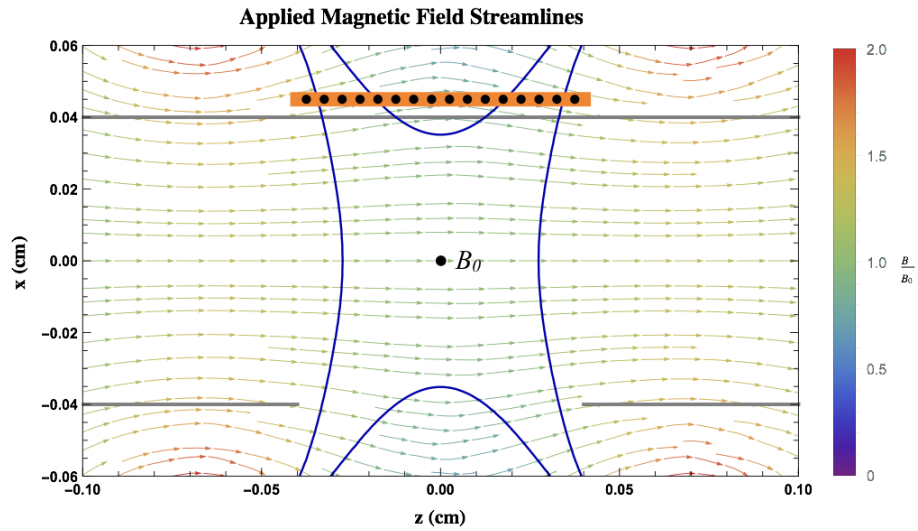

Figure 4.5: 2D Cross-section of the Applied Magnetic Field Streamlines and Field Strength along the experiment mid-plane. The glass cylinder is shown in gray and the WLA in orange. The applied field is primarily in the $\hat{z}$-direction within the glass tube. The field strengths are normalized to B_0, defined at the center point of the thruster geometry. The blue curves represent the region over which the field strength varies by less than 10%.

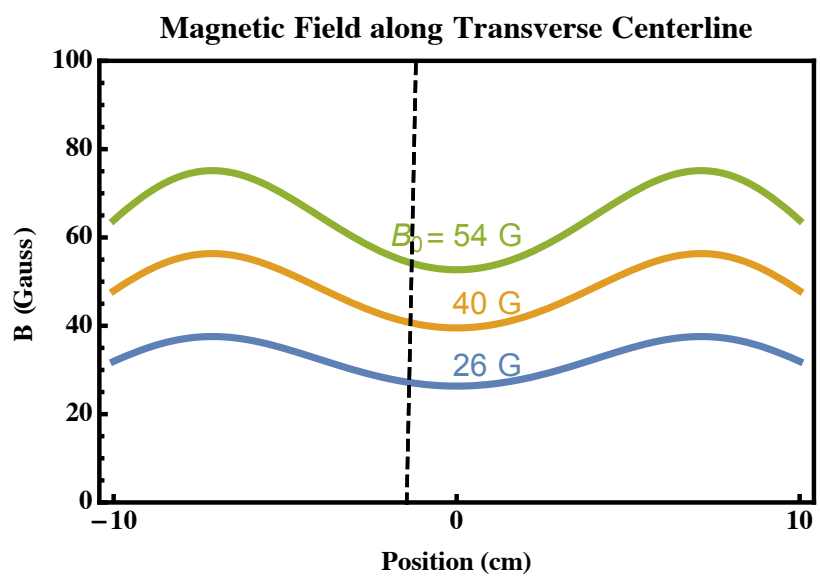

Figure 4.6: Magnetic field strength calculations for various applied currents along the centerline of the DWDTX. The dashed lines represent the edges of the exhaust hole in the glass tube.

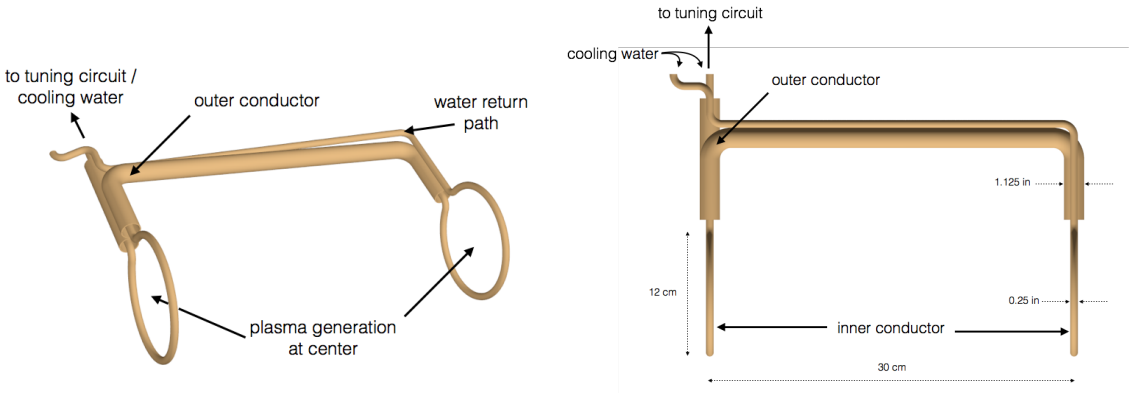

Figure 4.7: Plasma Source Antena. Left: Perspective. Right: Overview

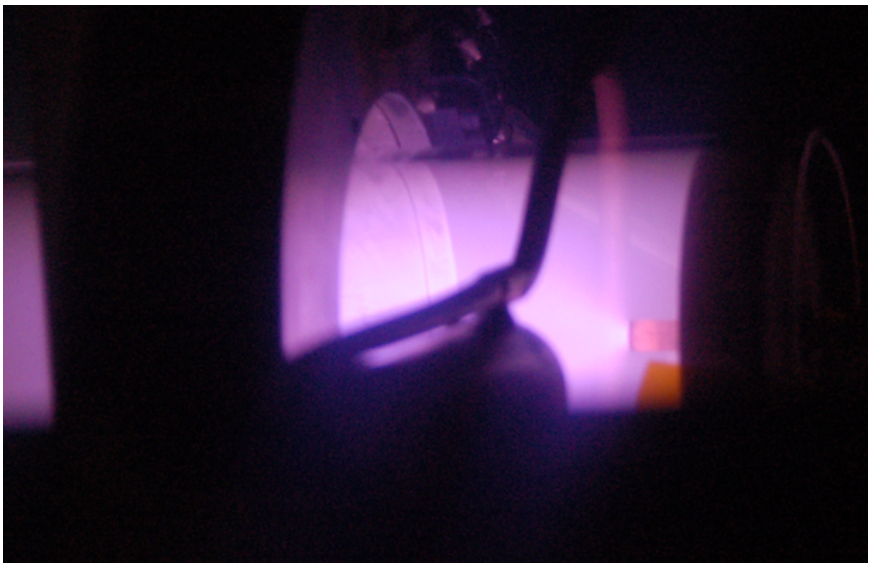

Figure 4.8: Photograph of Argon Ionization in Plasma Source

to contour as close to the confining tube as possible. The WLA consists of 1.5mm diameter magnet wire wrapped around four 8 cm alumina rods as show in Figure 4.9. The rods are supports by two G10 plates, 8 cm by 11 cm, with a semi-circle removed to allow the current paths to rest directly adjacent to the glass tube. Finally, the antenna is formed with 40 windings across its 8 cm width.

In our experimentation, the WLA is driven at frequencies from approximately 180 kHz to 450 kHz by a variable RF amplifier capable of delivering up to 1 kW. Similar to the PSA, the driving signal is also matched with a capacitive L-network[63], located

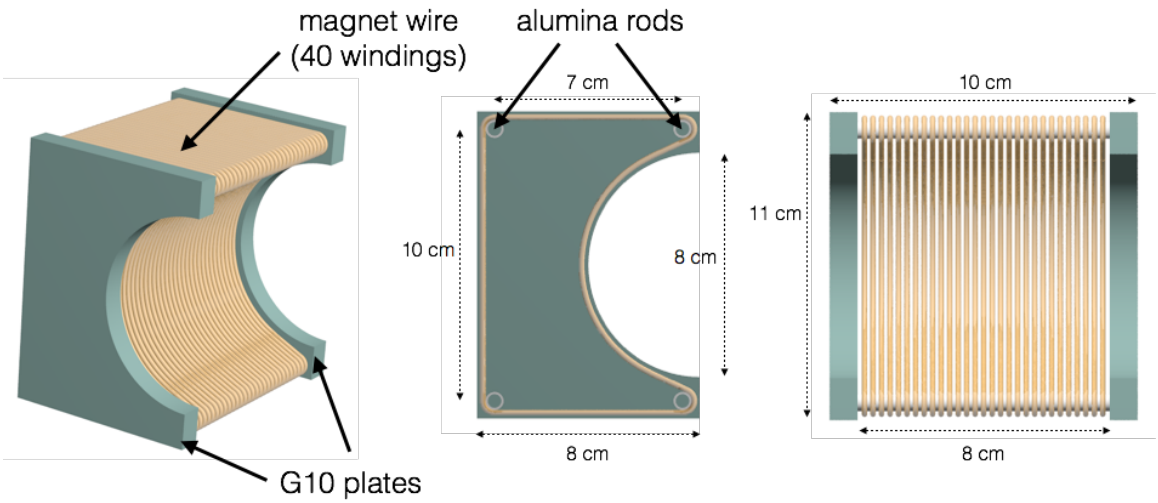

Figure 4.9: Wave Launching Antenna (WLA). Four alumina rods are mounted between two G10 plates. A single wrapping of the magnet wire is shown in yellow around the alumina rods.

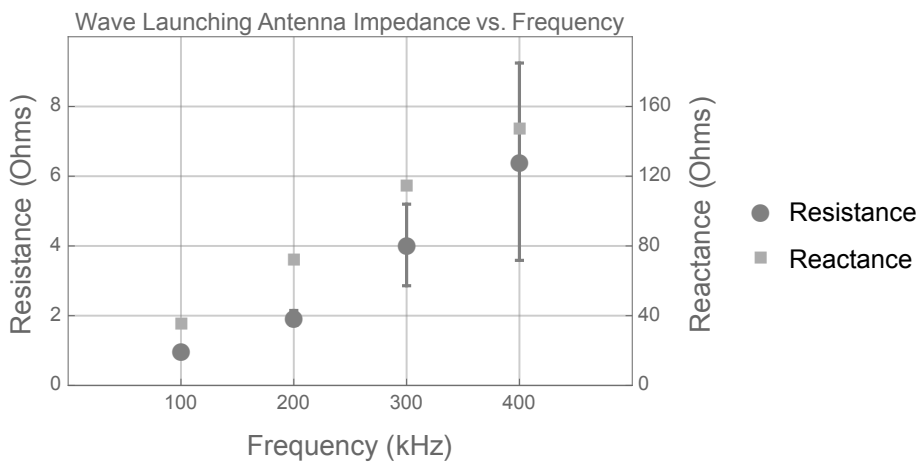

Figure 4.10: Impedance vs. Frequency. The WLA resistance and reactance was measured up to 400 kHz. At 400 kHz, the resistance is over 6 Ω, which creates large losses in the antenna. The linear fit of the antenna reactance gives an inductance of 60 μH.

outside the vacuum chamber. The frequency dependent impedance of the antenna was measured up to 400 kHz and is shown in Figure 4.10. The antenna inductance is 60 μH, and the resistance increases for increasing frequency, which results in larger power losses. This prevents the WLA from being driven to higher currents at higher frequencies.

Unlike the PSA, the WLA currents must be monitored in order to make direct comparisons to the developed analytical theory. Two diagnostics are connected to the WLA circuitry. Before the tuning network, a phase-matched voltage probe and Pearson coil[64] sample the voltage-current characteristics. A second Pearson coil is clamped along the current return path from the WLA to give the total current flowing into the antenna - which is the major controllable parameter in the analytical theory. The measured current is the amount flowing in a single winding of the WLA, and our theoretical model is dependent on the magnitude of the total current flowing on the antenna surface. Therefore, the correct J_a to match to our model is the measured current amplitude multiplied by the antenna winding number, 40. The matching network and diagnostic circuitry for the WLA is shown in Figure E.2.

4.1.3 Vacuum Chamber

The experimental apparatus was constructed on the thrust stand inside of EPPDyL's "Orange" Vacuum Tank (shown in Figure 4.11), which has an 8 ft. diameter and 25 ft. length. The chamber is pumped by a 4 ft. diffusion pump, backed by a roots blower and two roughing pumps, and we achieved an ultimate pressure typically near 30 μTorr while operating the experiment. The DWDTX is mounted at the front of the tank, on the far side from the pumping systems.

The tank has two translation stages for taking diagnostic measurements in the plasma plume, which can move a diagnostic suit in the axial and transverse directions. The axial direction is aligned with the length of the chamber and the transverse stage is perpendicular to the plasma plume.

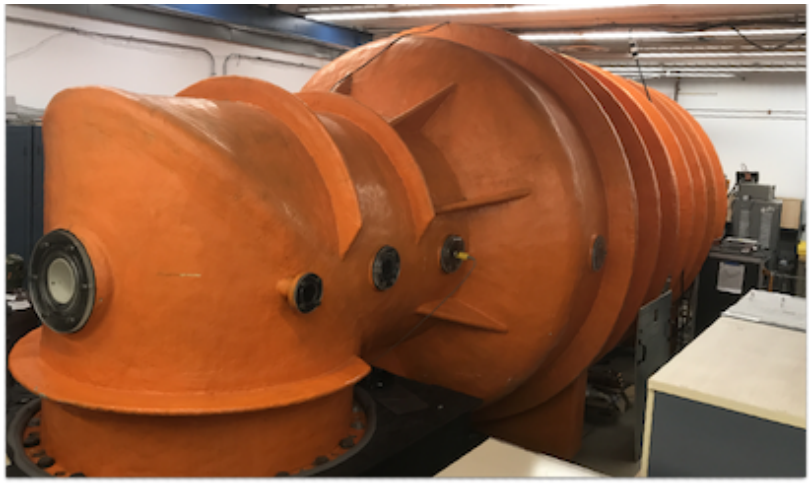

Figure 4.11: EPPDyL's "Orange" Tank. DWDTX is mounted on the far side of the tank. The near side of the tank sits on top of the pumping systems.

4.2 Plasma Diagnostics

The DWDTX deploys an array of electric probes to investigate the plasma plume including a Langmuir probe (LP), an emissive probe (EP), a Mach probe (MP), and a retarding potential analyzer (RPA). These probes can be mounted interchangeably on the two-axis translation stage. The primary diagnostic in this work is the MP used in conjuction with the LP to measure plasma flow velocity in Chapter 5. RPA measurements of ion acceleration are presented in Appendix C.

4.2.1 Langmuir Probe

Our Langmuir probe (LP) is used primarily to characterize the plasma source. Additionally, measurements of the electron temperature are used in conjunction with the Mach probe to take plume exhaust velocity measurements. The LP (shown in Figure 4.12) consists of a .25 mm diameter, 3 mm length, tungsten tip mounted in an alumina tube. The voltage on the probe is swept from -40 V to 80 V, and the corresponding current drawn by the probe is measured. It is driven by a 2 Hz oscillator connected to a floating bipolar operational amplifier. The current is measured

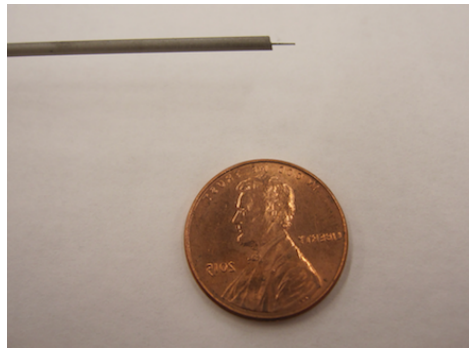

Figure 4.12: Langmuir Probe. An exposed .01 inch diameter tungsten wire housed in an insulating alumina tube. A current-voltage trace is used to determine the plasma electron temperature and density.

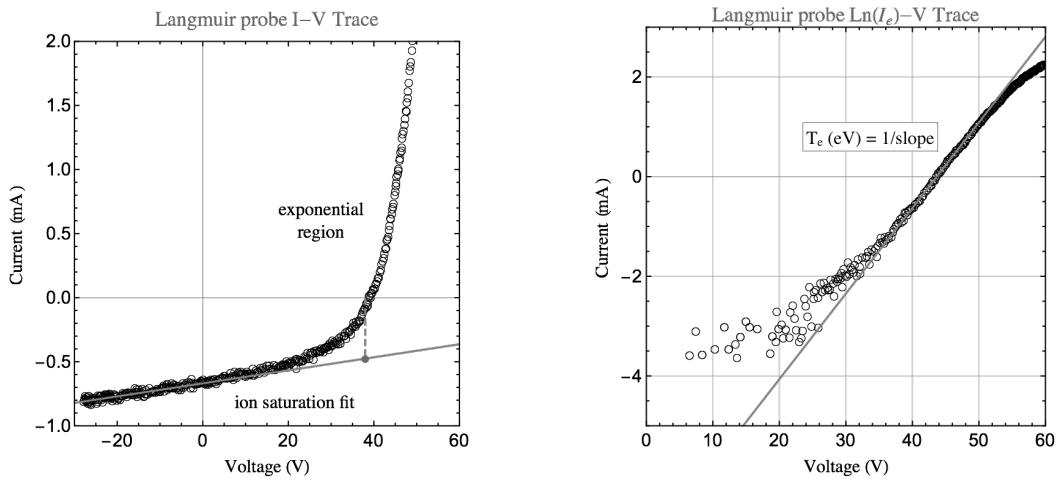

Figure 4.13: Sample Langmuir Probe Data Analysis.

from ground to the op-amp common over a 1kΩ sense resistor and a low-pass filter with a 3dB cut-off at 25 kHz to remove RF noise (circuitry shown in Figure E.3). It is well known that the electron temperature can be obtained from the inverse of the slope of the $\ln(I_e) - V$ trace (shown in Figure 4.13, and the density can be calculated from[65]

$$n = \frac{I_{\text{sat}}}{.61 e A_p \sqrt{T_e/m_i}}, \tag{4.1}$$

where I_{sat} can be determined by extrapolating a linear fit to the ion saturation regime up to the floating potential[66] as shown in Figure 4.13.

4.2.2 Mach Probe

Mach probes (MP) are electrostatic probes that measure the flow Mach number[67], $M = v_f/c_s$, where v_f is the flow velocity and c_s is the sound speed. The basic design includes two probe tips separated by an insulator and biased into the ion saturation regime. For a stationary plasma, each probe tip will draw equal ion saturation currents. However, when plasma flows perpendicularly to the collection surfaces (as shown in Figure 4.14), the upstream collection area will draw more current than the downstream side. The Mach number and flow velocity are then determined from[67, 68]

$$\frac{I_u}{I_d} = e^{\kappa_m M}, \tag{4.2}$$

where I_u and I_d are the respective upstream and downstream ion saturation currents and κ_m is a calibration constant.

Our probe (shown in Figure 4.14) consists of two 3 mm radius copper plates separated by ceramic insulation .5 mm thick. The probe is designed so that the size of the probe is larger than the Debye length even in the low density plume. Each plate is biased into ion saturation at -27 V and the current is measured over a 10 kΩ and 42 kΩ sense resistors for I_u and I_d respectively. The typical currents measured over the front and back surfaces of the MP differ by approximately a factor of 4-5 for most data runs. By using different sense resistors, the voltage drop on each side of the MP is roughly equal, which ensures that each probe surface maintains similar voltages.

Since the applied magnetic field in the exhaust plume is negligible, the calibration constant, κ_m, is taken to be 1.3 consistent with unmagnetized probe theory[68, 69, 70] and similar probe designs[71, 72]. Finally, we can measure the electron temperature with our Langmuir probe, and determine the plasma flow velocity from $M = u_{ex}/c_s$.

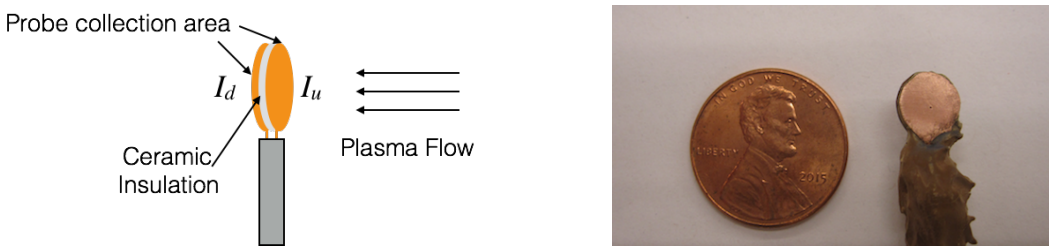

Figure 4.14: Mach Probe Geometry (left) and Photograph (right). Two 3mm radius copper plates sandwiched together. The variation in collected current by each plate is used to calculate the plasma flow velocity.

4.2.3 Retarding Potential Analyzer

A retarding potential analyzer (RPA) is an electrostatic probe which measures the ion velocity distribution. A RPA works by collecting ion currents for ion energies above a specified energy level, then sweeping over all relevant voltages to create a distribution function. This is done by biasing successive grids to varying potentials, so that no electrons and only the desired ions can reach the collecting electrode. The first grid is allowed to float to shield the plasma from the interior RPA potentials. The second grid is biased to a fixed negative potential to prevent electrons from entering the analyzer. The third grid is the varied from low to high potential in order to sweep through the ion energy distribution function (IEDF). And he final grid is negatively biased to suppress secondary electron emission from the collector plate, which rests at the back of the RPA channel. The RPA we used was borrowed from the Jet Propulsion Laboratory and has been used in previous work on Hall thrusters[73].

In order to measure the IEDF, the RPA selection grid was varied from 0 to 100 volts at 1 volt intervals. Simultaneously, the current collected was measured over a $1k\Omega$ resistor. The IEDF is then calculated from derivative of the IV curve,

$$f_\epsilon \propto -\frac{dI_c}{dV}, \tag{4.3}$$

and a sample measurement is shown in Figure 4.15.

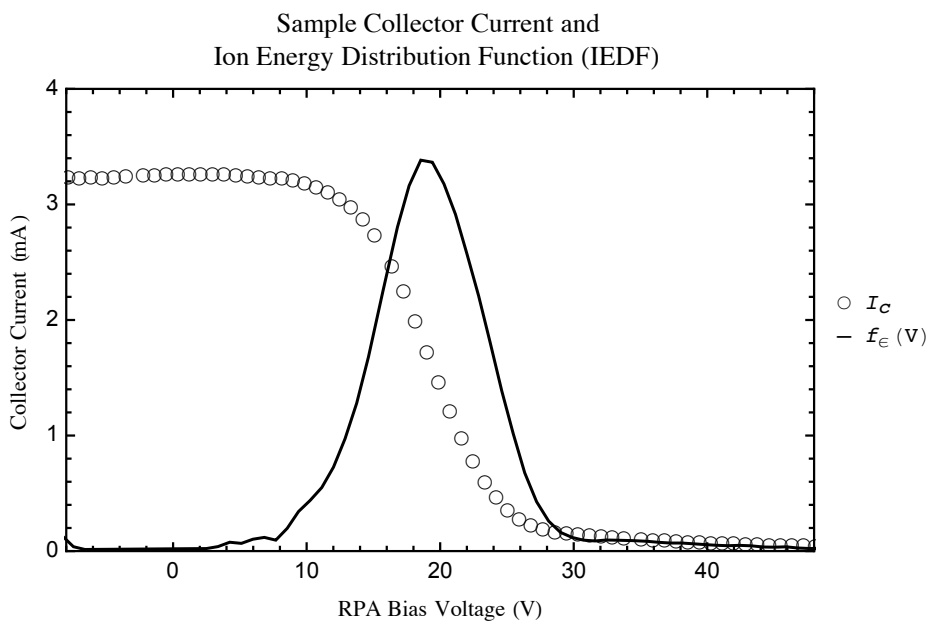

Figure 4.15: Sample Retarding Potential Analyzer Raw Data. The collector currents at each bias voltage are shown as circles. The ion energy distribution function from Equation 4.3 is the solid line shown in arbitrary units.

Finally, we note that the measured ions all enter the RPA at the plasma potential, which must be removed in order to get an accurate measurement. To do this, after each RPA sweep, the EP is moved into the same location and the data run repeated.

4.2.4 Emissive Probe

We use an emissive probe (EP) measurements to determine the plasma potential. Our probe (shown in Figure 4.16) is a .005 inch tungsten filament press mounted into a two bore alumina tube. The probe is heated by a Variac connected to an 10-to-1 voltage transformer, which also isolates the EP circuit. Finally, a diode is placed in series with the EP, which allows for the floating measurement to be taken during the half-cycle when no current flows and the entire isolated circuit floats to the plasma potential.[74, 75]

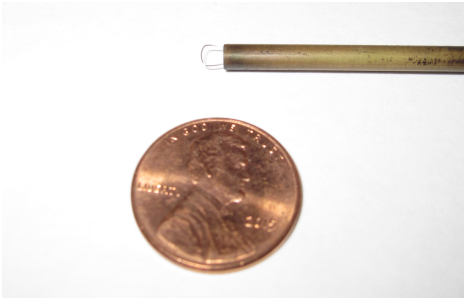

Figure 4.16: Emissive Probe. A .005 inch diameter loop of tungsten wire, which can be heated and allowed to float at the plasma potential.

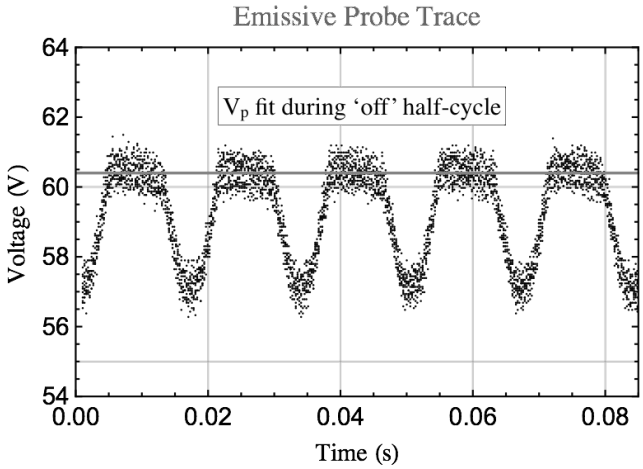

Figure 4.17: Sample Emissive Probe Data.

A typical EP trace is shown in Figure 4.17. While the probe is heated during a half-cycle, the circuit floats at a varying voltage. During the non-heating portion of the cycle, the probe floats to a constant value, which is taken as the plasma potential.

4.3 Plasma Source Characterization

Before taking measurements of any acceleration with the WLA, it is important to understand what is occurring within the pre-generated plasma, so that we can make direct comparisons with our analytical theory. Therefore, we take measurements of the plasma source and exhaust plume before adding any energy via the WLA, where

the entire plume structure is governed by the cross-field, cold-gas expansion into vacuum.

In our experimentation, we can control three major parameters into the system that effect the source plasma. These parameters are the neutral argon mass flow, $\dot{m}_n$; the PSA input power, P_{PSA}; and background magnetic field strength, B_0. For most of our experimentation, we will keep $\dot{m}_n$ and P_{PSA} constant while varying the background magnetic field (in addition to varying the frequency of the WLA once we begin powering the WLA). In this section, and in Chapter 5, we will fix the input power to the PSA at 550W with a neutral flow rate of 2 mg/s. This corresponds roughly to the minimum power and gas flow necessary to consistently excite a strong plasma over all chosen magnetic field strengths.

Pictures of the experiment at these conditions with the background magnetic field at 30 G are shown in Figures 4.18 and 4.19. Within the glass cylinder, where the plasma is generated and well-confined by the background magnetic field, a strong plasma is formed. The pink hue is typical of inductive argon plasma modes[76]. Outside the cylinder, well away from the exhaust plane, the plasma density has dropped off and we see only a diffuse blue glow.

The exhaust plume consists of particles that have exited from the source, and not plasma being created via stray RF fields. This was verified by extending the Faraday shield over the exhaust hole with an insulated copper mesh. When the shield was closed, plasma could still escape through the mesh, but RF fields would be cut off. No visible difference in the plume was observed between the two cases. However, the experiment was run solely without a faraday shield over the exhaust hole, since the physical impediment would prevent measurements inside the cylinder and potentially interfere with accelerated plasma as it exhausts.

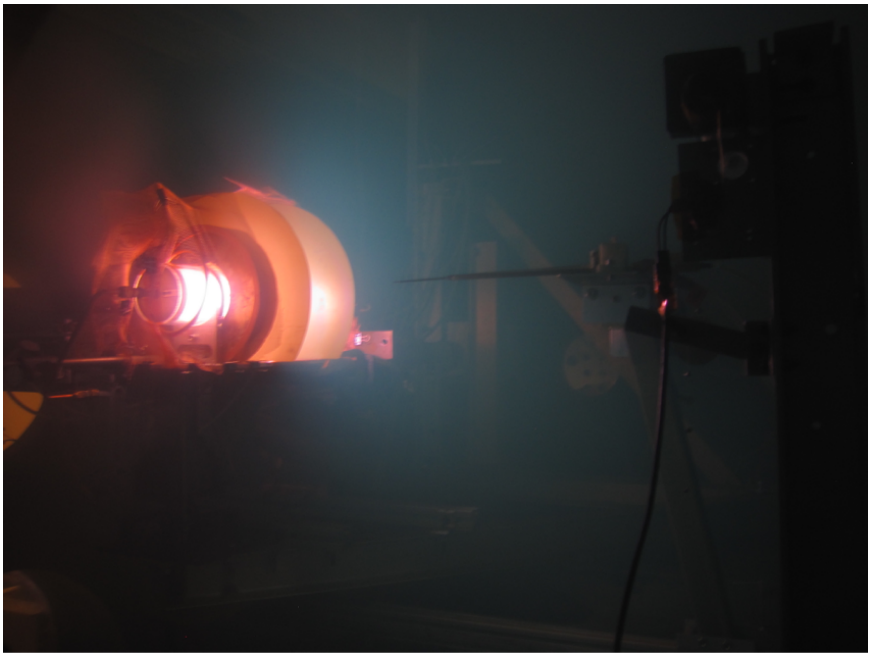

Figure 4.18: Direct Wave-Drive Thruster Experiment in Operation - Side View. The bright purple region is the generated source plasma. The blue cone is the expanding exhaust plume. A single Langmuir probe extends from the diagnostics stand into the plume.

Figure 4.19: Direct Wave-Drive Thruster Experiment in Operation - Overhead View. A strong plasma is formed in the glass tube, and some plasma is seen escaping the exhaust hole in the upper right direction. The blue exhaust plume seen in Figure 4.18 is not visible because the camera exposure was reduced in order to acquire a clearer image.

4.3.1 LP Measurements of the Plasma Source

Langmuir probe traces were taken of the plasma source at varying magnetic field strengths along the experimental center line, i.e, $z = 0$. These measurements start from the center of the glass cylinder (located 4 cm from the exhaust plane) to 20 cm into the plume from the exhaust plane. From the LP traces, we calculate the spatially dependent plasma density and electron temperature, which are shown in Figures 4.20 and 4.21 respectively. Inside the glass tube, where the magnetic field is strong, the density is approximately spatially constant. However, the source density varies for different magnetic field strengths. Plasma source density measurements at the DWDTX origin are shown for varying magnetic field strengths in Figure 4.22, and these density measurements are used in our analytical model to predict the WLA-plasma coupling in Chapter 5.

Unsurprisingly, the density falls off substantially outside of the source tube, as the plasma expands into the vacuum. This density decrease will limit the applicability of our thrust coupling model, since our model assumes a constant density infinitely far into the plume. The electron temperature similarly falls off as it exits the exhaust plane, but that temperature quickly stabilizes far into the plume for all background magnetic fields. This fall off is likely due to the plume expansion, as well as the electrons accelerating the ion population up to the sound speed.

Finally, we justify the sizes of our Langmuir and Mach probes using Table 4.1, contains a list of the various ranges of plasma properties measured at the center of the plasma source and in the plasma plume. Inside the source, the electron Larmor radius is larger than the LP and the Debye length is smaller. The Debye length is only comparable to the LP size as we get very far into the exhaust plume. 30 cm downstream into the plume, where our MP data will be taken, the Debye length is less than .5 mm, compared to the MP, which as a radius of 6 mm.

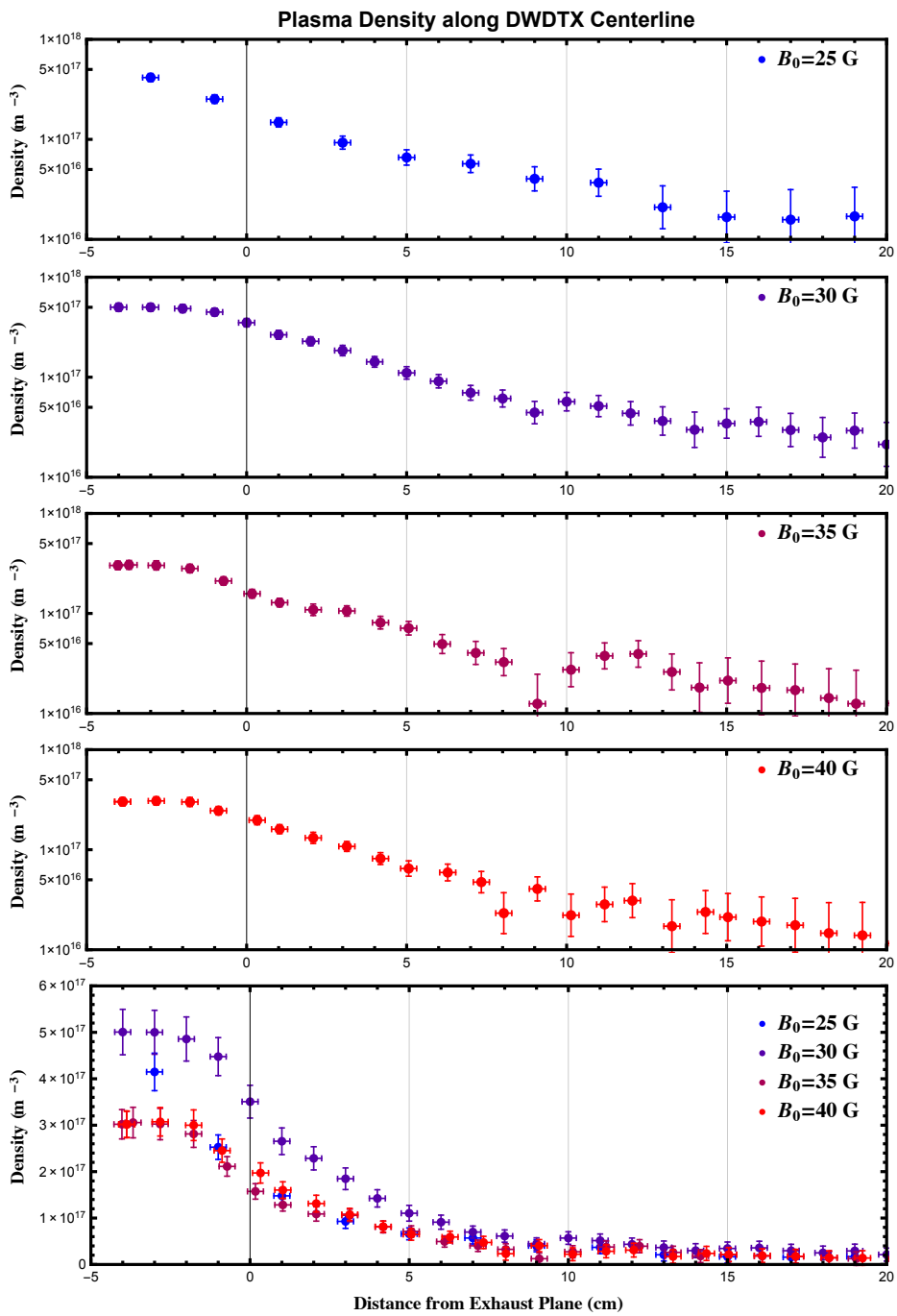

Figure 4.20: Plasma Density Measurements along DWDTX Centerline for Various B_0, $P_{\mathrm{PSA}} = 550\,\mathrm{W}$, and $\dot{m}_n = 2\,\mathrm{mg/s}$. Inside the glass cylinder, where the magnetic field is strong, we measure larger plasma densities that remain roughly constant. As the plasma expands across the field lines into vacuum, the density quickly decays for all magnetic field strengths.

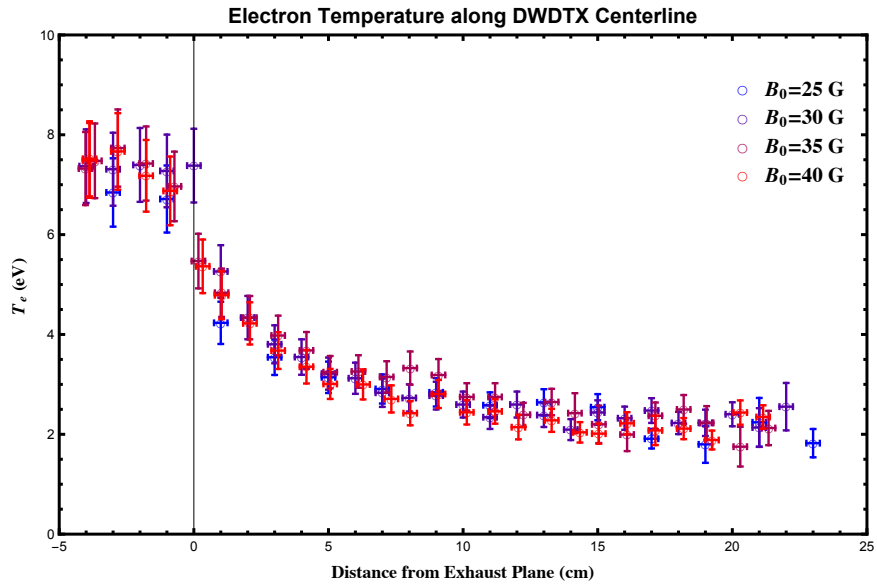

Figure 4.21: Electron Temperature Measurements along DWDTX Centerline for Various B_0, $P_{\mathrm{PSA}} = 550\,\mathrm{W}$, and $\dot{m}_n = 2\,\mathrm{mg/s}$. Inside the glass cylinder, where the magnetic field is strong, T_e is roughly 7.5 eV. As the plasma expands across the field lines into vacuum, the density quickly decays for all magnetic field strengths. This electron temperature does not vary substantially for the various magnetic fields strengths.

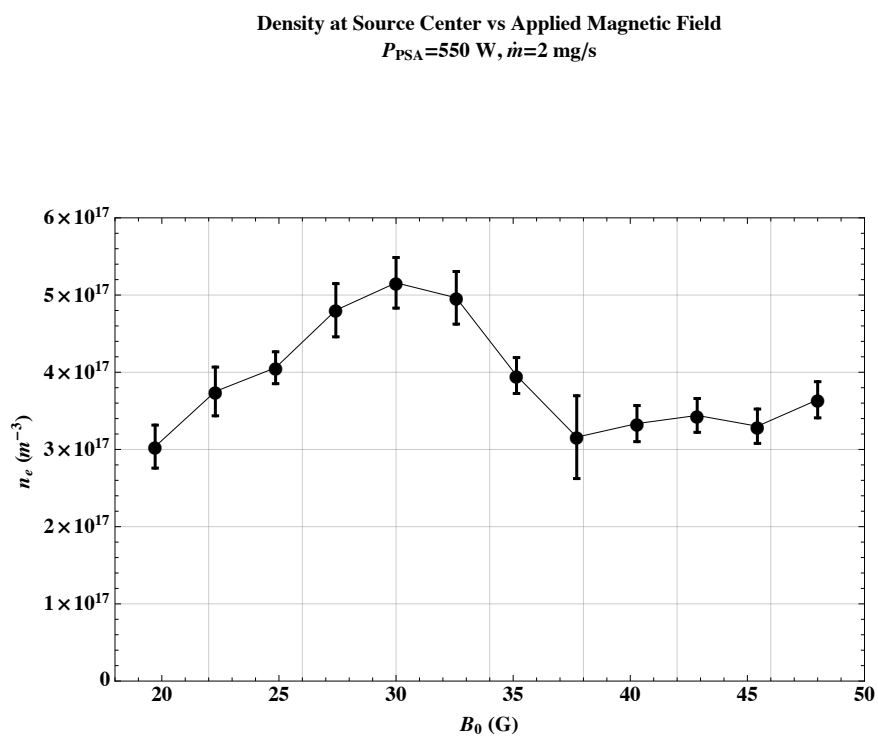

Figure 4.22: Density at center of plasma source is plotted against varying B_0 for $P_{\mathrm{PSA}} = 550\,\mathrm{W}$ and $\dot{m}_n = 2\,\mathrm{mg/s}$.

Table 4.1: DWDTX plasma properties measured in the source cylinder and in the plume. The source column gives ranges for the source operation. The plume values are at 30 cm downstream. Note the plume is effectively unmagnetized.

Parameter (Symbol)	**Source**	(unit)	**Plume**	(unit)
Plasma Density, n_e	$3-5\cdot 10^{17}$	m^{-3}	$\sim 10^{15}$	m^{-3}
Electron Plasma Frequency, ω_{pe}	$3-4\cdot 10^{10}$	rad/s	$2\cdot 10^{9}$	rad/s
Ion Plasma Frequency, ω_{pe}	$1.1-1.5\cdot 10^{8}$	rad/s	$7\cdot 10^{6}$	rad/s
Electron Temperature, T_e	$6-8$	eV	2.5	eV
Debye Length, λ_d	$2.5-3.5\cdot 10^{-5}$	m	$3\cdot 10^{-4}$	m
Plasma Parameter, Λ	$4-5\cdot 10^{5}$		$2\cdot 10^{5}$	
Electron Collision Frequency, ν_e	$1-2\cdot 10^{6}$	hz	$2\cdot 10^{4}$	hz
Electron Mean Free Path, λ_{mfp}	0.4-0.8	m	40	m
Electron Gyro Frequency, Ω_e	$4-9\cdot 10^{8}$	rad/s		
Ion Gyro Frequency, Ω_i	$6-13\cdot 10^{3}$	rad/s		
Electron Larmor Radius, ρ_{Larmor}	$1-2$	mm		
Ion Larmor Radius, ρ_{Larmor}	$2-4$	cm		

4.3.2 Critical Powers in the DWDTX

Before examining what, if any, changes occur to the plasma plume structure as the WLA is energized, it is helpful to examine the plasma source in the context of the design criteria from Section 3.2. Recall that in order for a thruster channel to be wave dominated, the total wave power must exceed certain critical values; $P_{\mathrm{wave}} \gg P^*$. P^* for both wall losses and thermal effects were derived in Equations 3.39 and 3.40 respectively. However, we assumed only a single propagating wave-mode in these derivations, which is not the case in the DWDTX, as the WLA launches a spectrum of wave-modes. As a result, the derived critical powers can only serve as a rough guide. Taking the geometry of the DWDTX, and noting the measurements for plasma density and temperature taken above, we can calculate P^* for each background magnetic field strength as shown in Table 4.2. While we have up to 1 kW of power available, the above requirements are for the power that must be injected into the launched wave

Table 4.2: Wave Power Required to Reach Wave-Dominated Channel Flow using Equations 3.39 and 3.40 and the measured DWDTX source densities and temperatures at the given B_0.

B_0	P^*_{wall}	P^*_{th}
25 G	3.3 W	120 W
30 G	4.0 W	170 W
35 G	2.8 W	240 W
40 G	2.8 W	310 W

modes, and the WLA-plasma coupling in the DWDTX is sufficiently weak that we do not operate in a wave-dominated regime.

To see this, we note that when operating the WLA at 400 kHz, near the high range of our tuning circuit, $R_{\text{wla}} = 6\Omega$. Therefore, the maximum amplitude of the current oscillation that 1 kW can drive through the WLA is approximately 18 A, which corresponds to $J_a = 720\,\text{Amp} - \text{turns}$. From Equation 3.71 and our source measurements at $B_0 = 25\,\text{G}$, the maximum achievable thrust on the order of 10 mN. And from Equation 2.4, this corresponds to only approximately 25 W of thrust power. Furthermore, we will see in Chapter 5 that by including the more applicable full cold, magnetized dispersion tensor in the coupling calculation, this force is an over-estimate. That the plume structure does not change significantly as the WLA is energized is demonstrated in Appendix B, where we show spatial density and temperature measurements for increasing power to the WLA, as well as overhead photographs of the plume structure for varying P_{WLA}. However, while the plume structure is not wave-dominated, we still observe increases in exhaust velocity in Chapter 5.

4.4 Discussion

In this chapter, we have presented the set-up for a proof-of-concept experiment to test the scaling laws derived in Chapters 2 and 3, and experimentally characterized the

exhaust plume. Using the criteria derived in Chapter 3, we showed that this plume structure should not be significantly affected by the addition of momentum from the WLA. This is demonstrated with Langmuir probe measurements in Appendix B.1 and visually in Appendix B.2.

While the plume is not wave-dominated, we still expect acceleration from the WLA. Some evidence for ion acceleration can be seen in Appendix C, where RPA measurements show an increase in the plume ion velocities as WLA power is increased. The behavior observed by the RPA is qualitatively consistent with our analytical predictions; however, the measured ion energy distribution functions exhibit too much broadening to compare directly with our analytical model. In the next chapter, we will explicitly validate the scaling behavior of our analytical model with Mach probe measurements in the exhaust plume.

Chapter 5

Exhaust Velocity Scaling in the Direct Wave-Drive Thruster Experiment[3]

While we have analyzed both the evanescing ordinary mode coupling and the magnetosonic mode coupling, we do not yet have any experimental evidence validating our analytical model and its predictions for the scaling behavior of such devices. In this Chapter, we will measure the downstream plume exhaust velocity as a function of increasing J_a over a range of plasma parameters in order to validate the predictions of our scaling model.

Before doing this, we note that for the parameter space that the DWDTX and WLA can reach, the low frequency assumption used in Chapter 3 does not hold. And instead we must use the full cold, magnetized dispersion tensor. After including this correction, we then derive the expected increase in the plume velocity. In particular, we will determine a single non-dimensional parameter which governs the antenna-

[3]This chapter is based on work being prepared to be submitted for publication and previously presented in [77]: Feldman, M.S. and Choueiri, E.Y., "Thrust Scaling in a Direct Wave-Drive Thruster," *52nd AIAA/ASME/SAE/ASEE Joint Propulsion Conference*, AIAA-2016-4948, Salt Lake City, UT, July 25-27, 2016.

plasma coupling in the DWDTX, which is a function of ω, B_0, and n_e. Therefore, we take velocity measurements in the plume while varying these quantities in order to demonstrate that antenna-plasma coupling and overall ion acceleration can be described by this single parameter.

In the next section, we will present the updated analytical theory specifically for the DWDTX configuration. In Section 5.2, we take Mach probe measurements of the exhaust plume for increasing J_a and varying applied frequencies and magnetic fields, and we compare the measured and predicted scaling behaviors in Section 5.3. Finally, we discuss the findings in Section 5.4.

5.1 Thrust and Exhaust Velocity Model for the DWDTX

For a simplified linear geometry, we previously determined that thrust is maximized for higher frequencies and lower magnetic field strengths. In this section, we will update the analytical model and apply it to the DWDTX. The previous geometry used in Chapter 3 assumed a forward and return current path for the WLA and a uniform plasma with a fixed magnetic field as shown in Figure 5.1. For the DWDTX, we assume the two current paths correspond to the front and back surface of the WLA described in Section 4.1.1. Since the front surface of the WLA is slightly curved to conform to the glass cylinder, we take the averaged position to be the location of the front surface in our modeled 2D geometry. And the total electromagnetic force is predicted by Equation 3.71:

$$T_{EM} = \frac{1}{8}\mu_0 J_a^2 Y \int_0^\infty \frac{2}{\pi}\left(\frac{\sin k_z H}{k_z H}\right)^2 \mathrm{Re}\left[\left(1 - e^{ik_1 l}\right)^2 e^{2ik_1 d}\frac{k_2 - k_1}{k_2 + k_1}\right] dk_z, \tag{5.1}$$

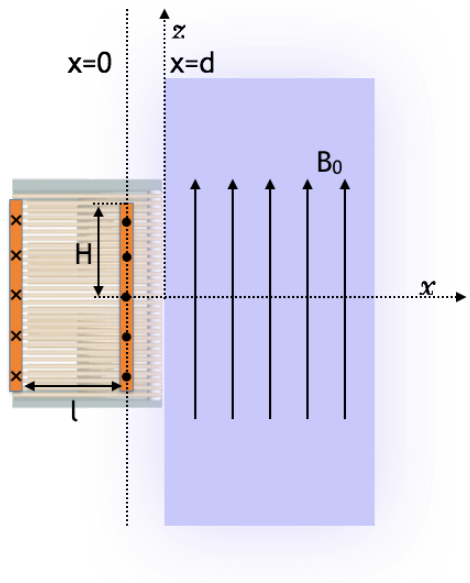

Figure 5.1: DWDTX Model Geometry. A semi-infinite plasma slab is placed at $x > d$ in a constant background magnetic field, $B_0\hat{z}$. A wave-launching antenna is located at $x = 0$ with a height, $2H$, in the $\hat{z}$-direction, and a total current in the $\hat{y}$-direction oscillating with frequency, ω, and magnitude, J_a. The location of the forward current path is taken to be the average position of the curved current path of the real WLA.

where $k_{1,2}$ correspond to the vacuum and plasma perpendicular wavenumbers, which are determined from the dispersion relation as a function of ω and k_z, and Y is the height of the WLA in the $\hat{y}$-direction.

In the DWDTX, our diagnostics measure the exhaust velocity. Before powering the WLA, the pre-generated plasma from the PSA simply expands into vacuum, and as the WLA is powered, we expect the exhaust velocity to increase in proportion to the thrust added in Equation 5.1. Therefore,

$$\Delta u_{ex_p} = u_{ex_p} - u_{ex_{p0}} = T_{EM}/\dot{m}_p. \tag{5.2}$$

where $u_{ex_{p0}}$ is the initial exhaust velocity of the non-WLA-driven plasma generated by the PSA and u_{ex_p} is the exhaust velocity as the WLA is powered.

However, the above equations for thrust and exhaust velocity include two assumptions that must be relaxed in order to match the DWDTX. First, the frequencies used

in the DWDTX are larger than the typical ion cyclotron frequencies, and therefore we must include the full, cold, magnetized dispersion tensor, rather than the dispersion relation in Equation 3.51. Second, the plasma source density is not uniform beyond the glass cylinder, and instead falls off rapidly, which limits the wave-modes that can be targeted.

In vacuum, the perpendicular wave-number remains the same;

$$k_1 = \sqrt{\frac{\omega^2}{c^2} - k_z^2}. \tag{5.3}$$

In the plasma, the correct dispersion relationship for the perpendicular wave number as a function of as a function of ω and k_z becomes

$$k_2 = \sqrt{\frac{\omega^2}{c^2} S - k_z^2 - \frac{\frac{\omega^4}{c^4} D^2}{\frac{\omega^2}{c^2} S - k_z^2}}, \tag{5.4}$$

where S and D are the typical parameters derived by Stix[58].

$$S = 1 - \sum_{\sigma=i,e} \frac{\omega_{p\sigma}^2}{\omega^2 - \omega_{c\sigma}^2}. \tag{5.5}$$

$$D = \sum_{\sigma=i,e} \frac{\omega_{c\sigma}}{\omega} \frac{\omega_{p\sigma}^2}{\omega^2 - \omega_{c\sigma}^2}. \tag{5.6}$$

As in Chapters 2 and 3, ω/c is sufficiently small that Equation 5.3 can be reduced to $k_1 = ik_z$. Additionally, Equation 5.1 was derived assuming the plasma extends infinitely in the $\hat{x}$-direction, and we note that the plasma density falls off rapidly outside of the glass cylinder in the DWDTX. Therefore, the WLA can only couple to wave modes with sufficiently small wavelength. We approximate this by integrating over only those k_z that generate modes with sufficiently large k_x, and we assume all other k_z have no contribution to the total thrust. This termination of the integral occurs at a maximum k_z defined when $k_x L = 1$, where L is the diameter of the

cylinder. Therefore, we define k_{zm} by

$$\frac{1}{L^2} = \frac{\omega^2}{c^2}S - k_{zm}^2 - \frac{\frac{\omega^4}{c^4}D^2}{\frac{\omega^2}{c^2}S - k_{zm}^2}. \tag{5.7}$$

And in the frequency range targeted in the DWDTX, $\omega_{ci} < \omega < \omega_{LH}$, we can approximate the solution as

$$k_{zm} \approx \frac{\omega}{v_A} \cdot \frac{\omega_{pi}L}{c}. \tag{5.8}$$

which becomes the upper limit of integration for our thrust and exhaust velocity equations. This is maximized for larger frequencies and densities, and lower magnetic fields. Finally, for all $k_z < k_{zm}$ in the targeted frequency range of the DWDTX, $k_2 \gg k_1$.

Combining these approximations with Equations 5.1 and 5.2, we have

$$\Delta u_{ex_p} \approx \frac{\mu_0}{4\pi\dot{m}_p} J_a^2 Y \cdot \int_0^{k_{zm}} \left(\frac{\sin k_z H}{k_z H}\right)^2 \left(1 - e^{-k_z l}\right)^2 e^{-2k_z d} dk_z. \tag{5.9}$$

In the DWDTX, the maximum k_{zm} we can target occurs at the high end of our frequency range and the low end of our applied magnetic field range, and corresponds to roughly $k_{zm} = 5\,\mathrm{m}^{-1}$. And the lengths of interest are: $H = .04\,\mathrm{m}$, $l = .04\,\mathrm{m}$ and $d = .01\,\mathrm{m}$. As a result, for our experimentation, k_{zm} is sufficiently small to justify a series expansion approximation. And we note that the predicted velocity increase is limited by the return current path that gives rise to the $(1 - e^{-k_z l})$ term.

Taking the first two terms of the series expansion,

$$\Delta u_{ex_p} \approx \frac{\mu_0}{4\pi\dot{m}_p} J_a^2 Y \cdot \int_0^{k_{zm}} \left(l^2 k_z^2 - \left(l^3 - 2dl^2\right) k_z^3\right) dk_z. \tag{5.10}$$

Table 5.1: Nondimensional parameters governing the DWDTX behavior and their approximate values.

Nondimensional Quantity	**Symbol**	**Value in DWDTX**
WLA Height	$\bar{Y}$	2
Stand-off Distance	$\bar{d}$	.25
Current Path Separation	$\bar{l}$	1
Characteristic Wave-number	K	up to .4

And integrating, we get

$$\Delta u_{ex_p} \approx \frac{\mu_0}{12\pi\dot{m}_p} J_a^2 \bar{Y}\bar{l}^2 K^3 \left(1 - \frac{3}{4}(\bar{l} + \bar{d})K\right), \tag{5.11}$$

where we have introduced four non-dimensional parameters: three lengths defined by $\bar{Y} = Y/H$, $\bar{d} = d/H$, and $\bar{l} = l/H$; and

$$K = k_{zm}H = \bar{k}_a \frac{\omega_{pi}L}{c} = \frac{\omega H}{v_A}\frac{\omega_{pi}L}{c}, \tag{5.12}$$

which is the characteristic nondimensional wavenumber of the system. K is proportional to the same normalized Alfvén wavenumber seen in Chapter 3 and a second term dependent on the diameter of the plasma source. Table 5.1 shows the values of each nondimensional parameter in the DWDTX. The lengths are all fixed ratios of the DWDTX geometry, but K can be varied as a function of frequency, magnetic field strength, and plasma density. That is,

$$K \sim \frac{\omega n_e}{B_0}. \tag{5.13}$$

Table 5.2: Parameter space investigated for each Trial measurement of Δu_{ex} vs. J_a.

Trial	$\boldsymbol{\omega/2\pi}$ **(kHz)**	$\boldsymbol{B_0}$ **(G)**	$\boldsymbol{n_e}$ **(m^{-3})**
1	200-440	30	$5 \pm 1 \cdot 10^{17}$
2	360	20-50	$3 - 5 \pm 1 \cdot 10^{17}$
3	440	20-50	$3 - 5 \pm 1 \cdot 10^{17}$

5.2 Exhaust Velocity Measurements

In order to validate our predictions for the scaling of exhaust velocity, we measure the increase in the plume exhaust velocity, Δu_{ex}, as J_a is increased for various frequencies and magnetic field strengths. To do this, Mach probe (MP) measurements were taken 30 cm from the edge of the glass cylinder, where the Mach number, $M = u_{ex}/c_s$. We then determined the sound speed, c_s, from Langmuir probe (LP) measurements of electron temperature at the same location. The plume electron temperature, $T_e \approx 2.5$ and does not vary significantly as shown in Appendix B.

In this chapter, the plasma source antenna power was held fixed at 550 W, and the neutral argon flow was held fixed at 2 mg/s. We then performed three data sweeps measuring Δu_{ex} vs. J_a for various applied frequencies and magnetic field strengths. Table 5.2 shows the parameter space investigated for each data sweep. In Trial 1, the background magnetic field was held constant as ω was increased. In the latter two, the applied frequency was held constant as the background magnetic field was varied. For each configuration, we measured the plasma source density at the center of the glass cylinder, as well as the electron temperature in the exhaust plume, neither of which varied as the WLA was energized.

The plume exhaust velocity before powering the WLA is approximately 3 km/s, and the measurements of the change in the plume exhaust velocity, Δu_{ex}, are shown in Figure 5.2 against the total current in the WLA, J_a. The exhaust velocity increases for increasing J_a, and we see that higher frequencies and lower magnetic fields result

in better performance. This is qualitatively consistent with our theoretical predictions in Equation 5.11, as well as our RPA measurements in Appendix C, which suggested stronger ion acceleration at lower B_0.

5.3 Comparison of Experimental Measurements to Analytical Theory

To make a more explicit comparison to our analytical predictions, we note that Equation 5.11 is proportional to J_a^2, a function of K, and various geometric ratios. And in fact, we can observe these dependencies in the measured data. In Figure 5.2, the increases is Δu_{ex} appear parabolic with J_a. In Figure 5.3, we plot Δu_{ex} against J_a^2 and observe approximately linear trend lines across most data sweeps, which is consistent with our model.

Next, we calculate K for each data run as a function of the measured n_e and the applied ω and B_0. In Figure 5.4, we combine the data from Figure 5.3 and show two plots of Δu_{ex} vs J_a^2 for all three trials. In the first, each trial is colored separately. In the second, we place each data run regardless of trial into one of four bins based on the nondimensional wavenumber, $K < .15$, $0.15 < K < 0.2$, $0.2 < K < 0.25$, and $K > 0.25$. And we can see clearly that increased K leads to better performance.

Finally, in order to make a direct comparison between the predicted and measured behavior for the scaling of exhaust velocity, we calculate $\Delta u_{ex}(J_a^2, K)$ from Equation 5.11 by including $\dot{m}$ and the system geometry, which remain fixed throughout the experimentation. In Figure 5.5, we show the measured increase in exhaust velocity against the predicted increase. The data collapse to a linear trend line, which suggests that the nondimensional K controls the device performance consistent with our model's predictions.

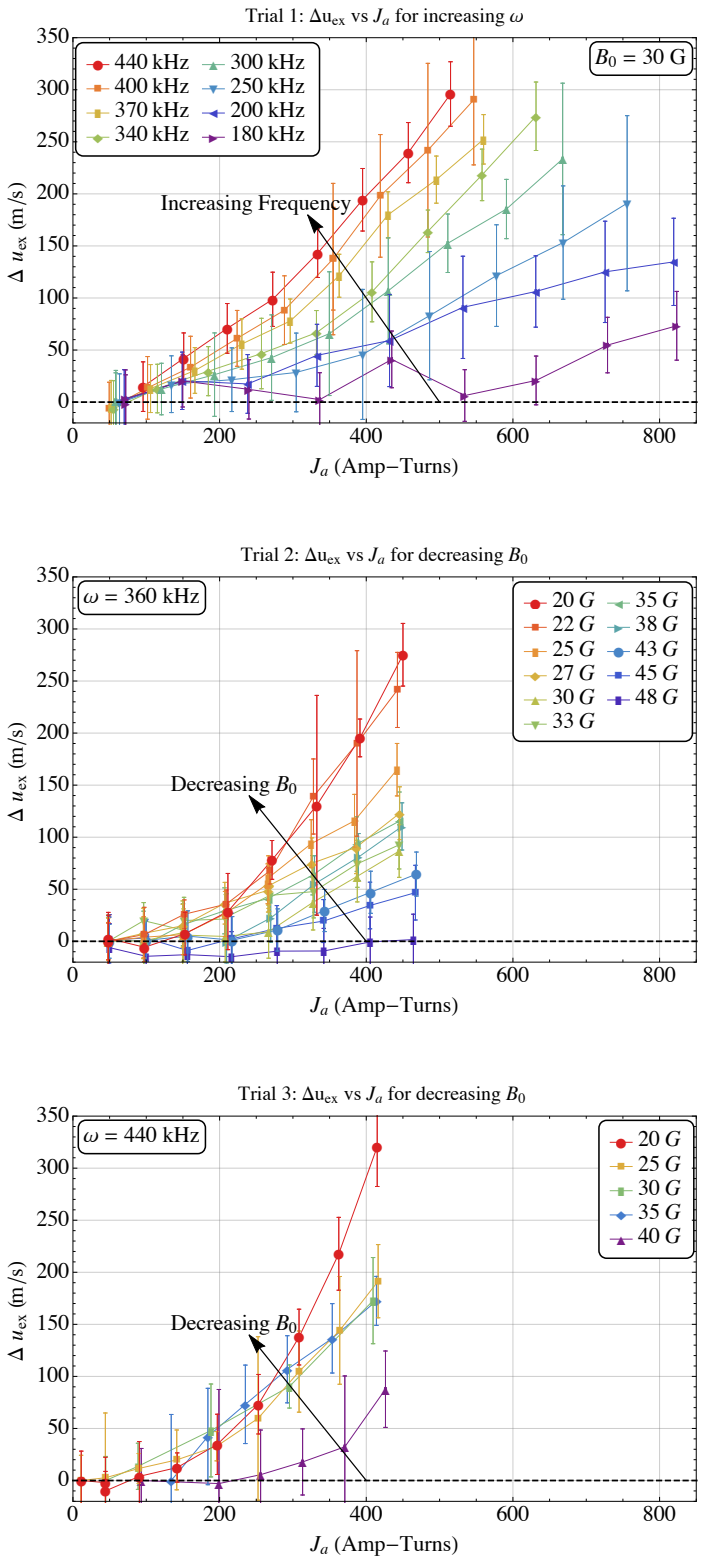

Figure 5.2: Measured increase in exhaust velocity, Δu_{ex}, vs. increasing WLA current, J_a, for each Trial.

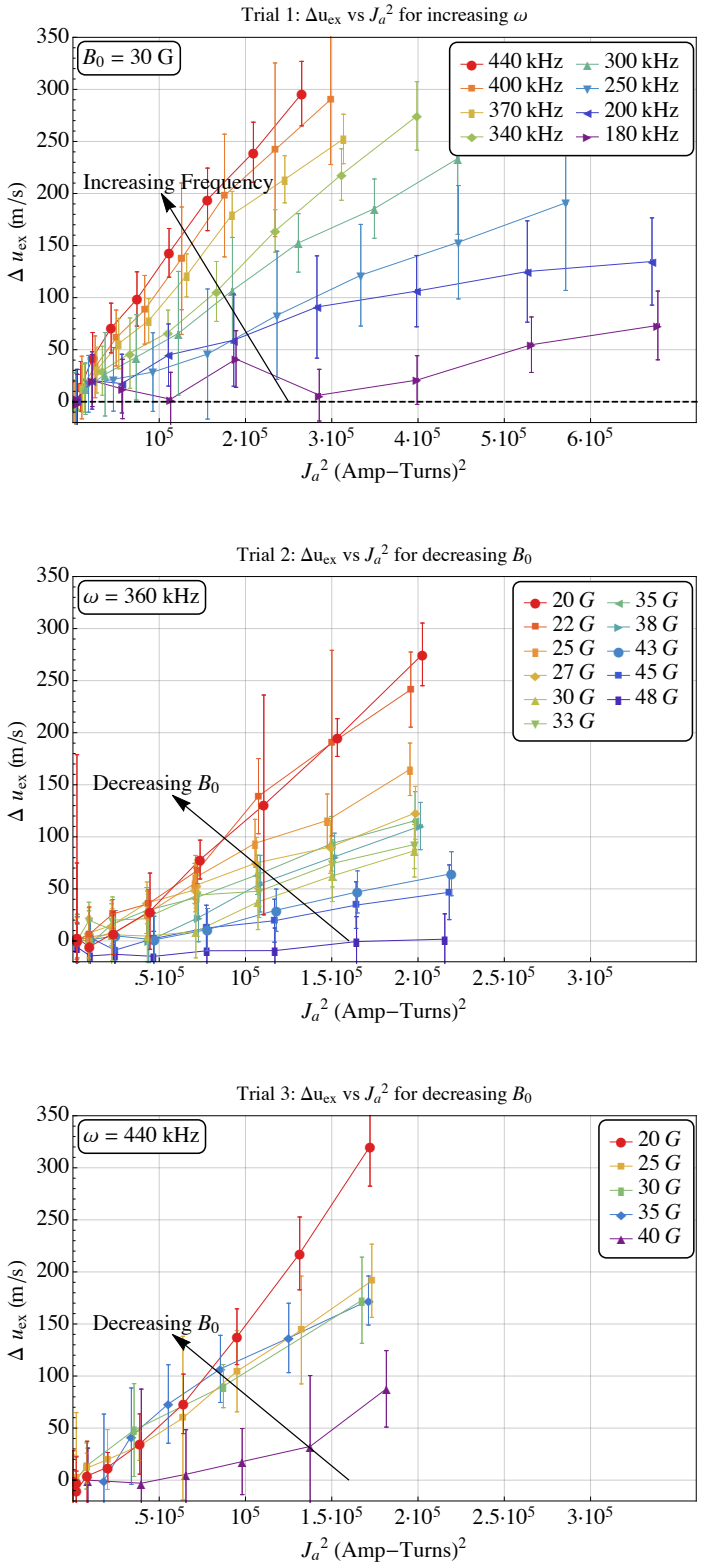

Figure 5.3: Measured increase in exhaust velocity, Δu_{ex}, vs. increasing WLA current squared, J_a^2, for each Trial.

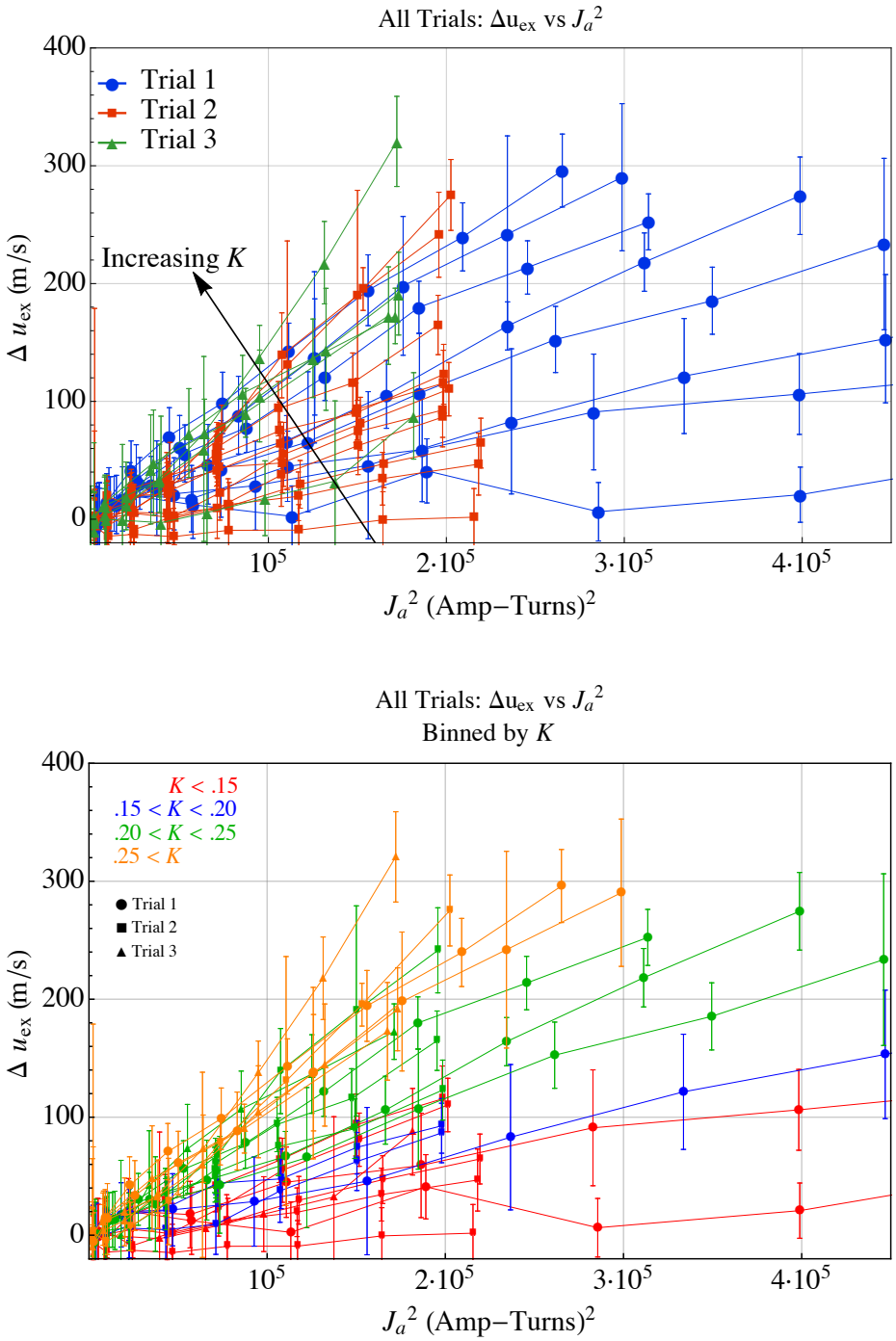

Figure 5.4: Measured increase in exhaust velocity, Δu_{ex}, vs. increasing WLA current squared, J_a^2, for each Trial. (Top) Each trial is colored separately. (Bottom) The data is binned by the calculated K. Red - $K < 0.15$, Blue - $0.15 < K < 0.2$, Green - $0.2 < K < 0.25$, Orange - $K > 0.25$.

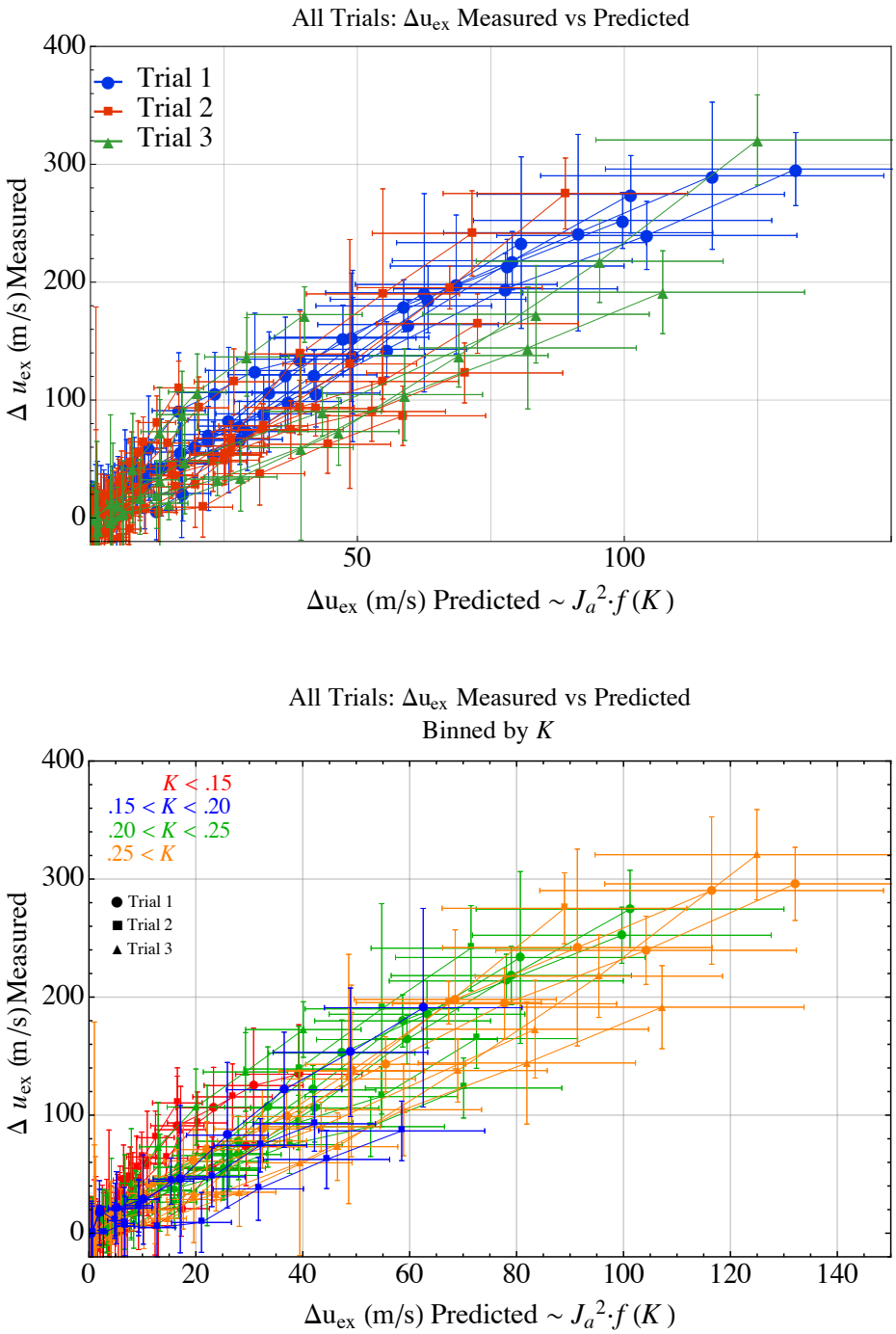

Figure 5.5: Measured change in exhaust velocity, Δu_{ex}, vs predicted change from Equation 5.11 for each Trial. (Top) Each trial is colored separately. (Bottom) The data is binned by the calculated K. Red - $K < 0.15$, Blue - $0.15 < K < 0.2$, Green - $0.2 < K < 0.25$, Orange - $K > 0.25$.

While most of the observed variation is within experimental error, the Trial 1 data, where frequency was varied, appears to collapse more tightly than Trials 2 and 3, where the applied magnetic field was varied. This is likely because the plasma source is dependent on the magnetic field strength. In Trial 1, where only Frequency is varied, the plasma source remains consistent throughout the data run. However, in Trials 2 and 3, the source density varies with the applied magnetic field. We account for this by including the measured density variations in our calculations for Δu_{ex}, but uncertainty in the density measurement could generate the observed deviations. And other unaccounted for effects, such as how the fringe interactions change with the varying plasma source structure, could further impact the observed scaling.

Finally, we note that Equation 5.11 under-predicts the measured increase in exhaust velocity by roughly a factor of 3. This is likely due to poor mass utilization in the DWDTX such that the momentum transferred is deposited only in the exhausted plasma and not the total neutral mass flow. This would tend to result in larger observed increases of the plasma exhaust velocity. Some of the total plasma momentum could also be deposited back into the neutrals via charge exchange collisions with exhausting neutrals, which is further discussed in Appendix D.

5.4 Chapter Summary

We have derived an analytical approximation for the scaling of T_{EM} and Δu_{ex} in the DWDTX as a function of the system geometry, the WLA current, J_a, and a single nondimensional parameter, K, which is essentially a normalized characteristic wavenumber. We validate this scaling law by taking representative measurements of the increase in u_{ex} in the plume as the WLA is powered. Qualitatively, u_{ex} increases for higher applied currents and frequencies, and for lower magnetic field strengths, which is consistent with the predictions of Equation 5.11. And by plotting $\Delta u_{ex_{\text{measured}}}$

against $\Delta u_{ex_{\text{predicted}}}$, the data collapses onto a linear trend, which suggests that the scaling of the observed behavior is consistent with the analytical scaling predictions.

The DWDTX is not an optimized configuration, but the derived scaling law suggests that performance can be improved by increasing a single nondimensional parameter $K \sim (\omega n_e)/B_0$ or increasing the size of the system, which agrees with predictions from Chapters 2 and 3. As it is difficult to increase density significantly in the system, performance can be most easily improved by decreasing B_0 or increasing ω. However, we cannot decrease B_0 arbitrarily as the source would quickly become unmagnetized, and we cannot increase ω arbitrarily as the WLA typically experiences higher resistive losses at higher frequencies. Nevertheless, even in the unoptimized configuration, we measure increases in the exhaust velocity that follow the our analytical scaling law.

Chapter 6

Conclusion

In this dissertation, we have presented a new, steady-state electric propulsion concept, which uses waves to directly accelerate a plasma. The primary advantage of such a device - the Direct Wave-Drive Thruster (DWDT) - is that the acceleration can be achieved electrodelessly via inductive coupling, which prevents lifetime limitations associated with current mature electric propulsion technologies[2, 5, 6, 4, 3, 7, 8]. This acceleration scheme additionally avoids various drawbacks and inefficiencies associated with other electrodeless thrusters, and can potentially be operated with variable specific impulses.

Using various waves to drive plasma flows has been discussed extensively in fusion literature[36, 37, 38, 39, 40, 41, 42, 51, 52], but there has been little consideration for propulsion applications. The novelty of our analytical approach is that we begin the analysis with the wave-launching structure and not after the wave has already been excited within the plasma. This approach allows us to derive the scaling behavior of this class of accelerator as a function of externally controllable parameters.

We set out to describe the DWDT, determine its potential efficacy as a plasma accelerator, and develop guiding principles for the future development of these devices. Our findings can readily be split into three primary components:

- The generalized scaling behavior of thrust and thrust efficiency
- Major design considerations, including the choice of wave-mode
- Experimental validation of the scaling of the plasma acceleration

6.1 Summary of Major Findings

6.1.1 Generalized Scaling Behavior

A key aspect of any DWDT is that total force imparted to the plasma is proportional to the square of the oscillating field strength generated by the wave-launching antenna (WLA) structure. Assuming a linear plasma response to inductively launched wave-modes, these field strengths are proportional to the current flowing in the WLA. And in general, we can describe the total thrust as

$$T = C_T J_a^2, \tag{6.1}$$

where the thrust coefficient is dependent on the targeted wave-modes and geometry of the device. Moreover, thrust power is proportional to the square of thrust, and therefore scales with J_a^4, while the energy losses incurred from the momentum coupling are resistive in nature, which scale with J_a^2. Therefore the efficiency associated with the momentum coupling improves with increasing current:

$$\eta = \frac{1}{1 + \frac{\dot{m} R_{\text{eff}}}{C_T^2 J_a^2}}. \tag{6.2}$$

6.1.2 Design Considerations

While improved efficiency can be obtained with increasing current or power, much of the salient physics is subsumed into the thrust and loss coefficients, C_T and R_{eff}. By

analyzing the force coupling between a WLA and plasma via the evanescing, ordinary mode, we revealed three key nondimensional quantities of interest.

- $\bar{d}$ - WLA-Plasma stand-off distance normalized to the size of the WLA
- $\bar{\delta}_s$ - Plasma skin depth normalized to the size of the WLA
- $\bar{\nu}_e$ - Electron collision frequency normalized to the excitation frequency.

And we note that coupling improves as each of these quantities is decreased. Physically speaking, the force from the WLA on the plasma increases as the WLA is closer to the plasma, as the interaction length within the plasma decreases, and as fewer electron collisions de-phase the induced currents within the plasma. With typical assumptions for the size of a thruster and the plasma properties, we estimated an upper bound on potential efficiencies near 50% for a 10kW device.

The above calculations for thrust and efficiency describe the expected scaling trends, but ignore potential improvements and drawbacks associated with targeting specific wave modes. We showed that the expected exhaust velocity of an efficient DWDT should be comparable to the phase velocity of the targeted wave mode(s). For the typical EP plasmas, the magnetosonic wave has phase velocities in the desired range, and those phase velocities could be variably tuned by controlling the applied magnetic field strength. These waves have the added benefit of containing large momentum densities compared to other potential modes, such as electrostatic waves that were previously explored[30].

Assuming a 1D channel, with a single propagating magnetosonic wave-mode, we derived the channel dynamics for the mass and momentum flux carried by the magnetosonic wave. By comparing the idealized wave-driven transport to the mass flow driven by diffusion and thermal effects, we derived criteria to determine when the thruster channel dynamics will be dominated by the wave dynamics. These criteria take the form of Péclet numbers comparing the wave-driven mass advection or

diffusion due to the various effects.

$$\Pi_{th} = \frac{B_1^4}{4\mu_0^2}\frac{2\mu_0}{B_0^2}\frac{A}{2v_{th}\dot{m}} \gg 1. \tag{6.3}$$

$$\Pi_{\text{wall}} = \frac{B_1^4}{4\mu_0^2}\frac{\mu_0 e^2}{m_e T_e \nu_e}\frac{W A_{ex}^2}{\dot{m} A_{\text{wall}}} \gg 1. \tag{6.4}$$

And we used these criteria to define critical power requirements to generate a magnetosonic wave-dominated channel:

$$P_{th}^* = 2v_{th}\frac{B_0^2}{2\mu_0}A_{ex}, \tag{6.5}$$

$$P_{\text{wall}}^* = \frac{m_e T_e \nu_e}{\mu_0 e^2}\frac{A_{\text{wall}}}{W}. \tag{6.6}$$

Finally, we solved for the thrust coefficient in a simplified, linear geometry while targeting these magnetosonic modes and showed that improved coupling occurs for smaller wavelengths. This result is unsurprising, since it would be difficult to couple strongly to wavelengths substantially larger than the system size, and it agrees with the conclusions in Chapter 2 that suggest larger DWDTs have better coupling. Alternatively stated, momentum coupling into a DWDT is maximized for modes with large wavenumbers.

6.1.3 Experimental Validation

In order to validate our analytical framework discussed throughout this dissertation, we built a proof-of-concept experiment to test how various externally controlled parameters affected the antenna-plasma coupling. In the Direct Wave-Drive Thruster Experiment (DWDTX), we pre-ionized a plasma and measured the cold gas exhaust velocity of the plume with a Mach probe. Then for various applied magnetic field

strengths and excitation frequencies, we measured the increase in the plume exhaust velocity as the driving current to the WLA was increased.

We modeled the interaction between the WLA and the experimental plasma analytically and determined a nondimensional wave number that controls momentum coupling in the DWDTX,

$$K = \frac{\omega e n_e H L}{\epsilon_0 B_0 c^2} = \frac{\omega H}{v_A} \frac{\omega_{pi} L}{c} \sim \frac{\omega n_e}{B_0}, \tag{6.7}$$

where K is proportional to the excitation frequency and plasma density, but inversely proportional to the magnetic field strength. In this work, the maximum K achieved was approximately 0.4, and the total accelerations achieved were relatively small.

However, the measured increases in exhaust velocity were observed to be roughly proportional to J_a^2, which is expected from our global scaling model predictions. Additionally, by plotting the various measured increases in exhaust velocity against the predicted increases derived from the analytical model of the DWDTX, we found a single linear trend, consistent with our model predictions. That is, the derived nondimensional parameter, K, controls the performance the experiment.

6.2 Future Work

The work in this dissertation presents the Direct Wave-Drive Thruster concept and describes a framework for analyzing the scaling of thrust and thrust efficiency in such devices. This modeling has provided guidance to the design and optimization of DWDTs. However, there are number of outstanding questions regarding the efficacy of this type of accelerator. Our model has been limited to a linear regime, and therefore does not include non-linear effects that may be present at higher powers. Since the linear scaling laws suggest that higher efficiency is achieved for higher powers, it is important to understand how these effects might alter the current ana-

lytical model. Additionally, we constrained our various coupling solutions to planar geometries. This facilitated the derivation of explicit analytical solutions, but ignored any potential benefits that more complicated geometries might provide. Finally, our model is limited to cold, magnetized dispersion relationships, and could naturally be improved by the inclusion of kinetic terms and full numerical simulations, which might aid future optimizations.

The experimental work in this dissertation was performed primarily to validate the scaling of exhaust velocity derived from our analytical modeling. The DWDTX was designed to be simple to model and easy to vary parameters that affect coupling. As a result, it is not designed for efficient performance. Moreover, the total thrust and acceleration is constrained by large WLA resistances and a lack of available power. In order to validate the scaling of thrust with direct thrust measurements, either more power or a more optimized geometry will likely be required. One such option is to use an annular WLA geometry to ensure the current paths are all located adjacent to the plasma, which limits the adverse affects of the reverse current path in the linear geometry. This may increase the complexity of the design for the magnetic field structure, such as the proposed topology by Jorns and Choueiri[30], and increase the complexity of the analytical model. However, it is our hope that the approach validated in this work can help form the basis of these future optimizations.

Appendix A

Coupling Derivations from Chapters 2 and 3

A.1 Coupling in the Annular Geometry

Starting with Equations 2.14 and 2.17, we apply separation of variables on $\boldsymbol{A}_s$ such that

$$\boldsymbol{A}_s = R(\bar{r}) \cdot X(\bar{x}), \tag{A.1}$$

and define a separation constant a^2. Therefore, the solution can be described by

$$\frac{1}{\bar{r}R}\frac{\partial}{\partial \bar{r}}(\bar{r}\frac{\partial R}{\partial \bar{r}}) - \frac{1}{\bar{r}^2} = -a^2 \tag{A.2}$$

$$\frac{1}{X}\frac{\partial^2 X}{\partial \bar{x}^2} = a^2 + \begin{cases} 0, & \text{Region 1, 2} \\ b^2 & \text{Region 3} \end{cases} \tag{A.3}$$

where $b^2 = \bar{\delta}_s^{-2} \cos\theta_\nu e^{i\theta_\nu}$. The solutions to the R equation are Bessel functions of the 1st and 2nd kind. However, only Bessel functions of the first kind are physical. The X equation has growing and decaying exponential solutions, where physically

region 1 can only have growing exponentials and region 3 can only have decaying exponentials.

As a result, the solutions to Equations 2.14 and 2.17 in each region are:

$$\boldsymbol{A}_{1s}(\bar{r},\bar{x}) = \int_0^\infty \Big[C_1(a)e^{a\bar{x}}J_1(a\bar{r})\Big]da, \tag{A.4}$$

$$\boldsymbol{A}_{2s}(\bar{r},\bar{x}) = \int_0^\infty \Big[\big(C_2(a)e^{a\bar{x}} + C_3(a)e^{-a\bar{x}}\big)J_1(a\bar{r})\Big]da, \tag{A.5}$$

$$\boldsymbol{A}_{3s}(\bar{r},\bar{x}) = \int_0^\infty \Big[C_4(a)e^{-b\bar{x}}J_1(a\bar{r})\Big]da. \tag{A.6}$$

And C_i is the amplitude of each mode. Dodd and Deeds[46] previously generated and solved similar equations when the excitation term in Equation 2.11 was a single coil loop and the material had multiple layers of purely real conductivities. We proceed using their methodology. However, instead of a single loop we have an annular antenna, so we will use their solution and integrate over many loops to form a full annulus. Assuming a single coil loop with radius $\bar{r}_s$ in normalized coordinates and fixed current, J_a, the appropriate boundary conditions are:

$$\boldsymbol{A}_{1s}(\bar{r},-\bar{d}) = \boldsymbol{A}_{2s}(\bar{r},-\bar{d}) \tag{A.7}$$

$$\boldsymbol{A}_{2s}(\bar{r},0) = \boldsymbol{A}_{3s}(\bar{r},0) \tag{A.8}$$

$$\frac{\partial \boldsymbol{A}_{1s}}{\partial \bar{x}}\Big|_{\bar{x}=-\bar{d}} = \frac{\partial \boldsymbol{A}_{2s}}{\partial \bar{x}}\Big|_{\bar{x}=-\bar{d}} + \mu_0 J_a \delta(\bar{r}-\bar{r}_s) \tag{A.9}$$

$$\frac{\partial \boldsymbol{A}_{2s}}{\partial \bar{x}}\Big|_{\bar{x}=0} = \frac{\partial \boldsymbol{A}_{3s}}{\partial \bar{x}}\Big|_{\bar{x}=0}. \tag{A.10}$$

Solving these four equations for the unknown C_i, we have

$$C_1(a) = \frac{1}{2}\mu_0 J_a \bar{r}_s J_1(a\bar{r}_s)\left[\frac{a-b}{a+b}e^{-a\bar{d}} + e^{a\bar{d}}\right], \tag{A.11}$$

$$C_2(a) = \frac{1}{2}\mu_0 J_a \bar{r}_s J_1(a\bar{r}_s)\frac{a-b}{a+b}e^{-a\bar{d}}, \tag{A.12}$$

$$C_3(a) = \frac{1}{2}\mu_0 J_a \bar{r}_s J_1(a\bar{r}_s)e^{-a\bar{d}}, \tag{A.13}$$

$$C_4(a) = \mu_0 J_a \bar{r}_s J_1(a\bar{r}_s)\frac{a}{a+b}e^{-a\bar{d}}. \tag{A.14}$$

In order to calculate the forces and losses in the plasma, we are solely concerned with region 3, and the magnetic vector potential in that region is:

$$\boldsymbol{A}_{3\text{single}-\text{loop}}(\bar{r},\bar{x}) = \mu_0 J_a \int_0^\infty \left[\bar{r}_s J_1(a\bar{r}_s)J_1(a\bar{r})\frac{a}{a+b}e^{-a\bar{d}}e^{-b\bar{x}}\right]da. \tag{A.15}$$

A full annulus with inner radius r_0 and outer radius $2r_0$ can be thought of as many individual coils with radii between r_0 and $2r_0$, which correspond to $x = 1$ and $x = 2$ in the normalized coordinate system. Each individual coil has a fraction of the total antenna current, J_a. Taking the limiting behavior as infinitely many coils with J_a evenly distributed amongst them, we get a total magnetic vector potential by integrating over $\bar{r}_s$:

$$\boldsymbol{A}_{3s}(\bar{r},\bar{x}) = \mu_0 I_a \int_1^2 \int_0^\infty \left[\bar{r}_s J_1(a\bar{r}_s)J_1(a\bar{r})\frac{a}{a+b}e^{-a\bar{d}}e^{-b\bar{x}}\right]da d\bar{r}_s. \tag{A.16}$$

A.2 Magnetosonic Wave Coupling in a Linear Geometry

In this appendix, we present the derivation of the solution to the normalized vector potential in the linear geometry described in Chapter 3 and reprinted below in Figure A.1. Fourier transforming in time, and using the normalization scheme in Equation 3.43,

$$\bar{x} = \frac{x}{H} \qquad \bar{z} = \frac{z}{H} \qquad \bar{l} = \frac{l}{H} \qquad \bar{k}_v = \frac{\omega H}{c} \qquad \bar{k}_a = \frac{\omega H}{v_A}$$
$$\bar{A} = \frac{A}{\mu_0 J_a} \qquad \tau = \omega t \qquad \bar{\nabla} = H\nabla,$$

the wave equation becomes

$$\bar{\nabla}^2 \bar{A}_y + \bar{k}^2 \bar{A}_y = 0, \tag{A.17}$$

where

$$\bar{k}^2 = \begin{cases} \bar{k}_v^2 & \bar{x} < \bar{l} \\ \bar{k}_v^2 + \bar{k}_a^2 & \bar{x} > \bar{l} \end{cases}. \tag{A.18}$$

Applying separation of variables, such that $\bar{A}_y(\bar{x}, \bar{z}) = X(\bar{x}) \cdot Z(\bar{z})$, we have

$$X''(\bar{x}) = (-\bar{k}^2 + \bar{k}_z^2)X, \tag{A.19}$$

$$Z''(\bar{z}) = -\bar{k}_z^2 Z, \tag{A.20}$$

where k_z is a separation constant which must be integrated over to form a complete solution. Physically, k_z is the component of the solution wavenumber parallel to the magnetic field, and we effectively solve the coupling problem by determining the corresponding k_x for each k_z.

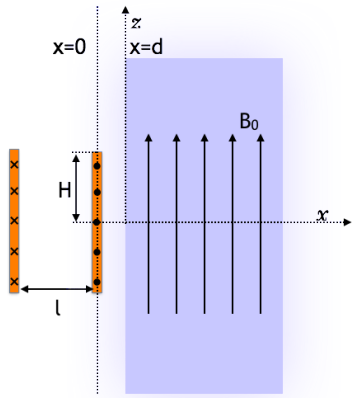

Figure A.1: Simplified magnetosonic mode driven DWDT geometry. A semi-infinite plasma slab is placed at $x > d$ in a constant background magnetic field, $B_0\hat{z}$. A wave-launching antenna is located at $x = 0$ with a height, $2H$, in the $\hat{z}$-direction, and a total current in the $\hat{y}$-direction oscillating with frequency, ω, and magnitude, J_a. The current return path for the WLA is located at $x = -l$. The geometry is assumed to be uniform and infinite in the $\hat{y}$-direction.

From the symmetry of the geometry, the solution is

$$Z \sim \cos(\bar{k}_z \bar{z}), \tag{A.21}$$

$$X \sim e^{\pm i\bar{k}_x \bar{x}}, \tag{A.22}$$

where

$$\bar{k}_x = \sqrt{\bar{k}^2 - \bar{k}_z^2}, \tag{A.23}$$

and X can take on either mode in regions 2 and 3, but can only represent outward propagating modes in regions 1 and 4. That is, no energy is coming into the system from infinity. Therefore, the piecewise solution of $\bar{A}_y$ is generated by integrating over

all possible parallel wavenumbers and takes the form given below:

$$\bar{A}_{y1}(\bar{x},\bar{z},\bar{k}_v,\bar{k}_a,\bar{l}) = \int_0^\infty C_1 e^{-i\bar{k}_x\bar{x}} \cos(\bar{k}_z\bar{z}) d\bar{k}_z, \tag{A.24}$$

$$\bar{A}_{y2}(\bar{x},\bar{z},\bar{k}_v,\bar{k}_a,\bar{l}) = \int_0^\infty (C_2 e^{i\bar{k}_x\bar{x}} + C_3 e^{-i\bar{k}_x\bar{x}}) \cos(\bar{k}_z\bar{z}) d\bar{k}_z, \tag{A.25}$$

$$\bar{A}_{y3}(\bar{x},\bar{z},\bar{k}_v,\bar{k}_a,\bar{l}) = \int_0^\infty (C_4 e^{i\bar{k}_x\bar{x}} + C_5 e^{-i\bar{k}_x\bar{x}}) \cos(\bar{k}_z\bar{z}) d\bar{k}_z, \tag{A.26}$$

$$\bar{A}_{y4}(\bar{x},\bar{z},\bar{k}_v,\bar{k}_a,\bar{l}) = \int_0^\infty C_6 e^{i\bar{k}_x\bar{x}} \cos(\bar{k}_z\bar{z}) d\bar{k}_z, \tag{A.27}$$

where

$$\bar{k}_x = \begin{cases} \bar{k}_1 = \sqrt{\bar{k}_v^2 - \bar{k}_z^2} & \bar{x} < \bar{d} \\ \bar{k}_2 = \sqrt{\bar{k}_v^2 + \bar{k}_a^2 - \bar{k}_z^2} & \bar{x} > \bar{d} \end{cases}, \tag{A.28}$$

and we have defined $\bar{k}_1, \bar{k}_2$ for convenience, representing the $\hat{x}$-directed wavenumbers corresponding to each k_z in vacuum and in the plasma respectively.

We can solve for each C_i by matching boundary conditions between each region as done in the derivation in Chapter 2 and Appendix A.1. Those conditions require that $\boldsymbol{A}$ and its derivative are continuous, except for a step dependent on the exciting currents in the WLA. Respectively, those conditions are equivalent to requiring a continuous electric and magnetic fields. All together, this forms six boundary conditions (2 at each interface corresponding to $\bar{x} = -\bar{l}, 0, \bar{d}$) which can be used to solve for the

six unknown C_is. In the dimensional system, these boundary conditions are:

$$\boldsymbol{A}_{y1}(-l, z) = \boldsymbol{A}_{y2}(-l, z), \tag{A.29}$$

$$\boldsymbol{A}_{y2}(0, z) = \boldsymbol{A}_{y3}(0, z), \tag{A.30}$$

$$\boldsymbol{A}_{y3}(d, z) = \boldsymbol{A}_{y4}(d, z), \tag{A.31}$$

$$\frac{\partial \boldsymbol{A}_{y1}}{\partial x}|_{x=-l} = \frac{\partial \boldsymbol{A}_{y2}}{\partial x}|_{x=-l} + \frac{\mu_0 J_a}{2H}(\Theta(z+H) - \Theta(z-H)), \tag{A.32}$$

$$\frac{\partial \boldsymbol{A}_{y2}}{\partial x}|_{x=0} = \frac{\partial \boldsymbol{A}_{y3}}{\partial x}|_{x=0} - \frac{\mu_0 J_a}{2H}(\Theta(z+H) - \Theta(z-H)), \tag{A.33}$$

$$\frac{\partial \boldsymbol{A}_{y3}}{\partial x}|_{x=d} = \frac{\partial \boldsymbol{A}_{y4}}{\partial x}|_{x=d}. \tag{A.34}$$

The $+$ and $-$ signs in Equations A.32 and A.33 correspond to current flowing in the negative and positive $\hat{y}$ directions in the return and forward current paths of the WLA, respectively. In the normalized system, these become:

$$\bar{A}_{y1}(-\bar{l}, \bar{z}) = \bar{A}_{y2}(-\bar{l}, \bar{z}), \tag{A.35}$$

$$\bar{A}_{y2}(0, \bar{z}) = \bar{A}_{y3}(0, \bar{z}), \tag{A.36}$$

$$\bar{A}_{y3}(\bar{d}, \bar{z}) = \bar{A}_{y4}(\bar{d}, \bar{z}), \tag{A.37}$$

$$\frac{\partial \bar{A}_{y1}}{\partial \bar{x}}|_{\bar{x}=-\bar{l}} = \frac{\partial \bar{A}_{y2}}{\partial \bar{x}}|_{\bar{x}=-\bar{l}} + \frac{1}{2}(\Theta(\bar{z}+1) - \Theta(\bar{z}-1)), \tag{A.38}$$

$$\frac{\partial \bar{A}_{y2}}{\partial \bar{x}}|_{\bar{x}=0} = \frac{\partial \bar{A}_{y3}}{\partial \bar{x}}|_{\bar{x}=0} - \frac{1}{2}(\Theta(\bar{z}+1) - \Theta(\bar{z}-1)), \tag{A.39}$$

$$\frac{\partial \bar{A}_{y3}}{\partial \bar{x}}|_{\bar{x}=\bar{d}} = \frac{\partial \bar{A}_{y4}}{\partial \bar{x}}|_{\bar{x}=\bar{d}}. \tag{A.40}$$

Substituting in Equations A.24-A.27, we can write Equations A.35-A.40 respectively as

$$\int_0^\infty C_1 e^{i\bar{k}_1\bar{l}} \cos(\bar{k}_z\bar{z}) d\bar{k}_z = \int_0^\infty (C_2 e^{-i\bar{k}_1\bar{l}} + C_3 e^{i\bar{k}_1\bar{l}}) \cos(\bar{k}_z\bar{z}) d\bar{k}_z, \tag{A.41}$$

$$\int_0^\infty (C_2 + C_3) \cos(\bar{k}_z\bar{z}) d\bar{k}_z = \int_0^\infty (C_4 + C_5) \cos(\bar{k}_z\bar{z}) d\bar{k}_z, \tag{A.42}$$

$$\int_0^\infty (C_4 e^{i\bar{k}_1\bar{d}} + C_5 e^{-i\bar{k}_1\bar{d}}) \cos(\bar{k}_z\bar{z}) d\bar{k}_z = \int_0^\infty C_6 e^{i\bar{k}_2\bar{d}} \cos(\bar{k}_z\bar{z}) d\bar{k}_z, \tag{A.43}$$

$$\int_0^\infty -i\bar{k}_1 C_1 e^{i\bar{k}_1\bar{l}} \cos(\bar{k}_z\bar{z}) d\bar{k}_z =$$

$$\int_0^\infty i\bar{k}_1 (C_2 e^{-i\bar{k}_1\bar{l}} - C_3 e^{i\bar{k}_1\bar{l}}) \cos(\bar{k}_z\bar{z}) d\bar{k}_z + \frac{1}{2}(\Theta(\bar{z}+1) - \Theta(\bar{z}-1)), \tag{A.44}$$

$$\int_0^\infty i\bar{k}_1 (C_2 - C_3) \cos(\bar{k}_z\bar{z}) d\bar{k}_z =$$

$$\int_0^\infty i\bar{k}_1 (C_4 - C_5) \cos(\bar{k}_z\bar{z}) d\bar{k}_z - \frac{1}{2}(\Theta(\bar{z}+1) - \Theta(\bar{z}-1)), \tag{A.45}$$

$$\int_0^\infty i\bar{k}_1 (C_4 e^{i\bar{k}_1\bar{d}} - C_5 e^{-i\bar{k}_1\bar{d}}) \cos(\bar{k}_z\bar{z}) d\bar{k}_z = \int_0^\infty i\bar{k}_2 C_6 e^{i\bar{k}_2\bar{d}} \cos(\bar{k}_z\bar{z}) d\bar{k}_z, \tag{A.46}$$

Equations A.41,A.42,A.43, and A.46 are easily simplified to exclude any integration. However, to simplify Equations A.44 and A.45, we first rearrange them into

$$\int_0^\infty -i\bar{k}_1(C_1e^{i\bar{k}_1\bar{l}} + C_2e^{-i\bar{k}_1\bar{l}} - C_3e^{i\bar{k}_1\bar{l}})\cos(\bar{k}_z\bar{z})d\bar{k}_z = \frac{1}{2}(\Theta(\bar{z}+1) - \Theta(\bar{z}-1)), \tag{A.47}$$

$$\int_0^\infty i\bar{k}_1(C_2 - C_3 - C_4 + C_5)\cos(\bar{k}_z\bar{z})d\bar{k}_z = -\frac{1}{2}(\Theta(\bar{z}+1) - \Theta(\bar{z}-1)). \tag{A.48}$$

Then we rely on the following equality:

$$\int_0^\infty \frac{2}{\pi}\frac{\sin\bar{k}_z}{\bar{k}_z}\cos(\bar{k}_z\bar{z})d\bar{k}_z = (\Theta(\bar{z}+1) - \Theta(\bar{z}-1)), \tag{A.49}$$

which essentially describes the Fourier-cosine decomposition of the WLA's shape into its constituent modes and allows us solve for the corresponding C_is without integration. As a result, Equations A.41-A.46 can be written more succinctly as:

$$C_1e^{i\bar{k}_1\bar{l}} = (C_2e^{-i\bar{k}_1\bar{l}} + C_3e^{i\bar{k}_x\bar{l}}), \tag{A.50}$$

$$(C_2 + C_3) = (C_4 + C_5), \tag{A.51}$$

$$(C_4e^{i\bar{k}_1\bar{d}} + C_5e^{-i\bar{k}_1\bar{d}}) = C_6e^{i\bar{k}_2\bar{d}}, \tag{A.52}$$

$$-i\pi\bar{k}_1(C_1e^{i\bar{k}_1\bar{l}} + C_2e^{-i\bar{k}_1\bar{l}} - C_3e^{i\bar{k}_1\bar{l}}) = \frac{\sin\bar{k}_z}{\bar{k}_z}, \tag{A.53}$$

$$i\pi\bar{k}_1(C_2 - C_3 - C_4 + C_5) = -\frac{\sin\bar{k}_z}{\bar{k}_z}, \tag{A.54}$$

$$i\bar{k}_1(C_4e^{i\bar{k}_1\bar{d}} - C_5e^{-i\bar{k}_1\bar{d}}) = i\bar{k}_2C_6e^{i\bar{k}_2\bar{d}}. \tag{A.55}$$

Finally, we can algebraically solve Equations A.50-A.55 to find each C_i.

$$C_1 = \frac{1}{2\pi i}\frac{\sin \bar{k}_z}{\bar{k}_z}\frac{1}{\bar{k}_1}\left(1 - e^{i\bar{k}_1\bar{l}}\right)\left(1 + \frac{\bar{k}_1 - \bar{k}_2}{\bar{k}_1 + \bar{k}_2}e^{2i\bar{k}_1 d}\right) \tag{A.56}$$

$$C_2 = -\frac{1}{2\pi i}\frac{\sin \bar{k}_z}{\bar{k}_z}\frac{1}{\bar{k}_1}e^{i\bar{k}_1\bar{l}} \tag{A.57}$$

$$C_3 = \frac{1}{2\pi i}\frac{\sin \bar{k}_z}{\bar{k}_z}\frac{1}{\bar{k}_1}\left(1 + \frac{\bar{k}_1 - \bar{k}_2}{\bar{k}_1 + \bar{k}_2}\left(1 - e^{i\bar{k}_1\bar{l}}\right)e^{2i\bar{k}_1 d}\right) \tag{A.58}$$

$$C_4 = \frac{1}{2\pi i}\frac{\sin \bar{k}_z}{\bar{k}_z}\frac{1}{\bar{k}_1}\left(1 - e^{i\bar{k}_1\bar{l}}\right) \tag{A.59}$$

$$C_5 = \frac{1}{2\pi i}\frac{\sin \bar{k}_z}{\bar{k}_z}\frac{1}{\bar{k}_1}\frac{\bar{k}_1 - \bar{k}_2}{\bar{k}_1 + \bar{k}_2}\left(1 - e^{i\bar{k}_1\bar{l}}\right)e^{2i\bar{k}_1 d} \tag{A.60}$$

$$C_6 = \frac{1}{\pi i}\frac{\sin \bar{k}_z}{\bar{k}_z}\frac{1}{\bar{k}_1 + \bar{k}_2}\left(1 - e^{i\bar{k}_1\bar{l}}\right)e^{i(\bar{k}_1 - \bar{k}_2)d} \tag{A.61}$$

Appendix B

Observations of DWDTX Plume Structure as WLA is Energized

In Chapter 4, we predicted that the structure of the DWDTX plume was unlikely to be dominated by wave dynamics. In this Appendix, we show this both visually and with direct LP measurements of the plume.

B.1 Langmuir Probe Measurements

Using the same input conditions to the DWDTX as in Chapter 4, where $P_{\mathrm{PSA}} = 550\,\mathrm{W}$ and $\dot{m}_n = 2\,\mathrm{mg/s}$, we take LP measurements of the exhaust plume with $B_0 = 30\,\mathrm{G}$. The WLA was driven at $\omega = 2\pi \cdot 300\,\mathrm{kHz}$ and at $P_{\mathrm{WLA}} = 0, 400, 700\,\mathrm{W}$. Under these conditions, the maximum J_a is roughly 600 Ampere-turns. Figure B.1 shows the spatial density measurements as the WLA power is increase, and there is no statistically significant change in the plasma density at any location in the plume. A similar plot of the electron temperature variation is shown in Figure B.2 under the same conditions. Again the measured change is within the error of the measurement. At conditions with higher B_0, there is similarly little change in the measured profile of the plume density and the plume electron temperature.

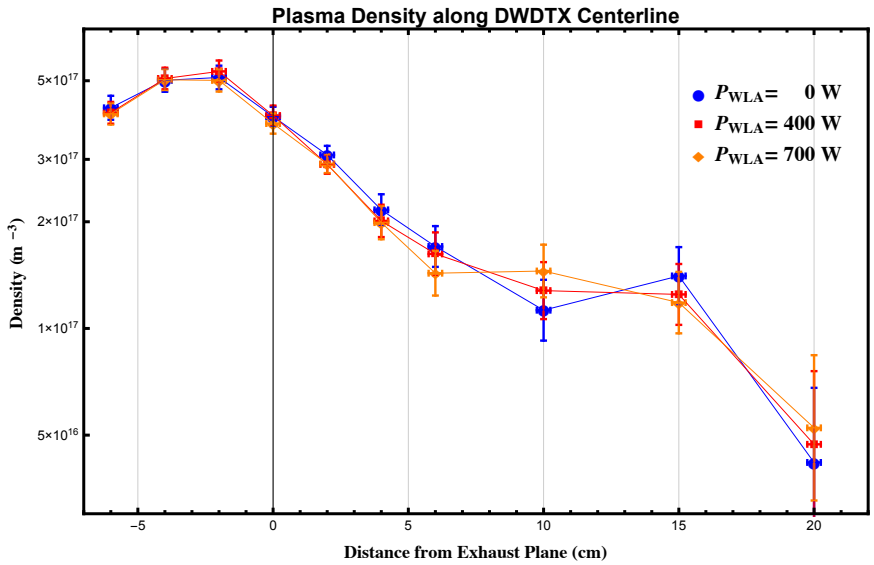

Figure B.1: Spatial Density Variation along the DWDTX Centerline as WLA Power is Increased for $\omega = 2\pi \cdot 300\,\text{kHz}$, $B_0 = 30\,\text{G}$, $P_{\text{PSA}} = 550\,\text{W}$, and $\dot{m}_n = 2\,\text{mg/s}$. In the plasma source region, there is no observed variation in the plasma density. Far into the exhaust plume, the observed variations are still within experimental error. Power is not increased to the maximum 1 kW because the WLA would overheat in the time it takes to make the various LP measurements.

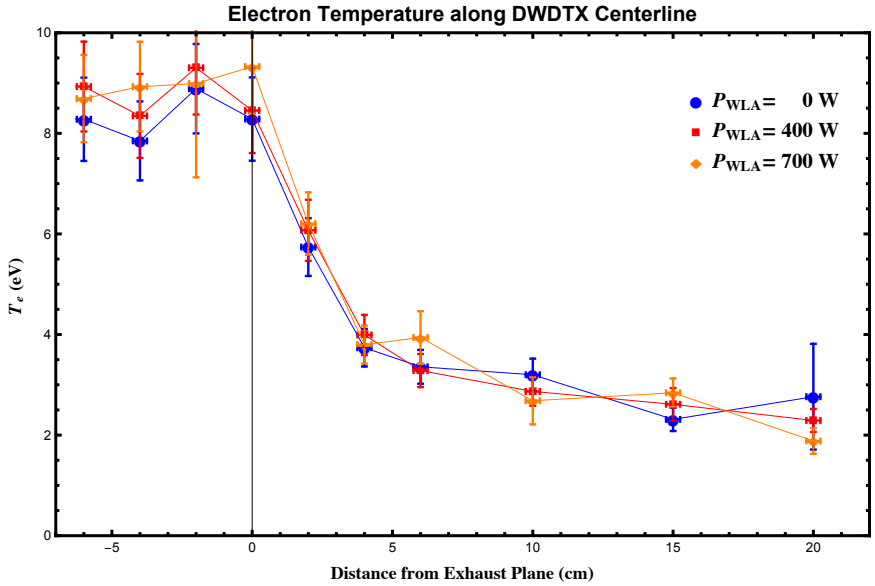

Figure B.2: Spatial Temperature Variation along the DWDTX Centerline as WLA Power is Increased at same conditions as Figure B.1.

Because each LP trace is averaged over many cycles and the WLA has no cooling, it becomes difficult to take full spatial resolutions of the plume density and temperature profiles as done with the WLA not powered. But it is clear that the overall plume structure is not significantly affected. However, because the velocity measurements derived from the Mach probe are sensitive to T_e, we specifically retake those measurements at the MP measurement location for full sweeps of the WLA power at various B_0 and ω, and observe no significant change in T_e. Sample runs for the same conditions above and for varying B_0 are shown in Figure B.3. T_e 30 cm downstream in the plume remains near 2.5 eV, as seen in Figures 4.21 and B.2. While it does vary as J_a is increased, this appears to be predominantly due to measurement error rather than any heating effect in the plume.

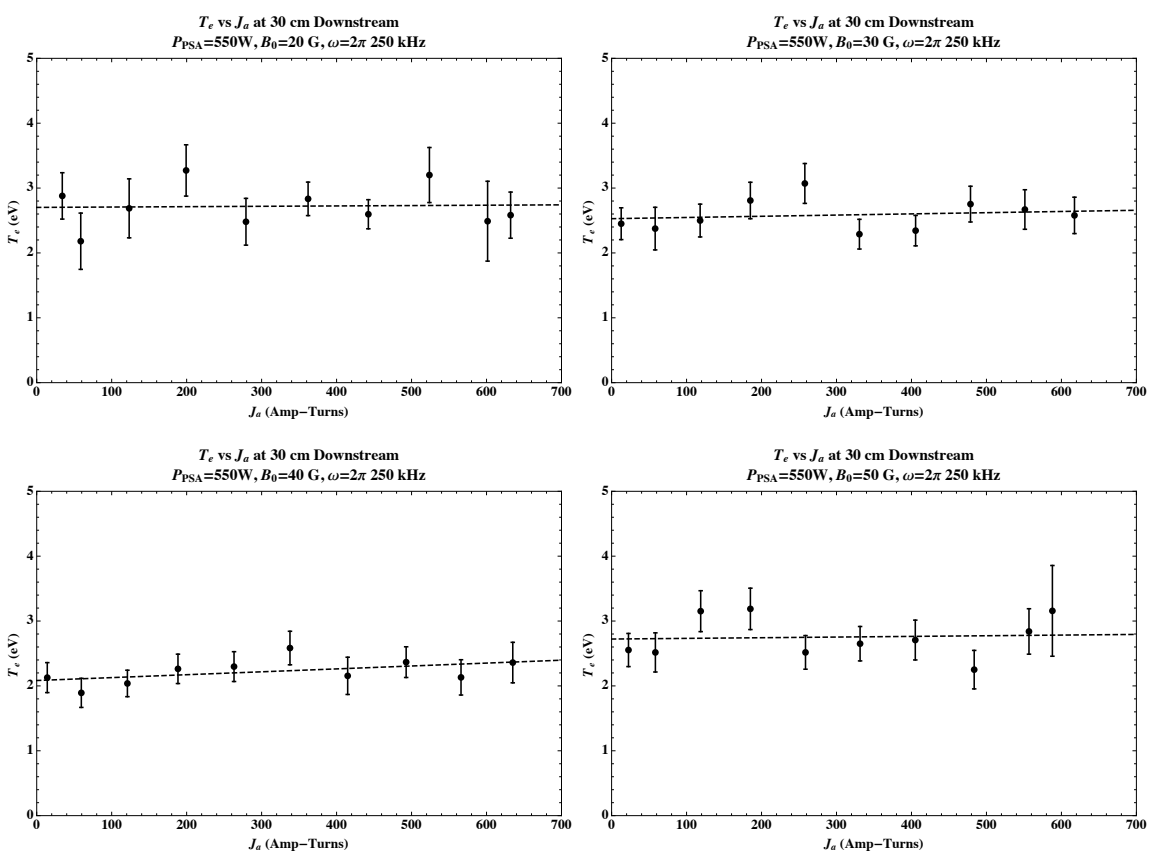

Figure B.3: Electron Temperature measured 30 cm downstream as the WLA is energized for various B_0 at $\omega = 2\pi \cdot 300\,\text{kHz}$. The dashed lines are a linear fits. The observed variation with J_a is mostly within experimental error.

B.2 Visual Changes

It is interesting to observe visually any changes in the plasma plume as the WLA is powered. To do this, overhead pictures of the exhaust plume were taken with a Logitech C920 webcam[78] and using Logitech's control application with brightness set to 25% and contrast to 50%. Images were taken for various B_0 and increasing power to the WLA, up to 500 W operating at 200 kHz. Under these conditions, we do not expect the plume to be wave dominated, since most of the WLA power is lost to the antenna resistance. Therefore, we do not expect major changes in the plume structure.

Two sets of images are shown below in Figure B.4. The first set of images are taken with $B_0 = 26\,\mathrm{G}$. The second set with $B_0 = 50\,\mathrm{G}$. In each set on the left is the exhaust plume with no wave power applied. And on the right is the plume with 600 W of power to the WLA at 200 kHz.

While there is no significant changes in the visible plume structure in either case, we do observe a slightly brighter plume in the lower B_0 case when amplifying the visible differences. To do this, we take the difference of RGB color channels from each image set and amplify the resulting channel data by a factor of 5. Those two resulting image differences are shown in Figure B.5. For the $B_0 = 50\,\mathrm{G}$ case, there is little obvious difference in the exhaust plume. And for the $B_0 = 26\,\mathrm{G}$ case, there is a subtle increase in the light intensity of the plasma just outside of the exhaust plane. It makes sense that the lower B_0 case would affect the plume more, since from Table 4.2 we see that the lower B_0 case requires less power for the plume to become wave-dominated. However, even for the lower magnetic field, the change in the plume is minimal.

Figure B.4: Photographs of Exhaust Plume as Power to the WLA is Increased. Left: $B_0 = 26\,\mathrm{G}$, Right: $B_0 = 50\,\mathrm{G}$. Top: $P_{\mathrm{WLA}} = 0\,\mathrm{W}$. Bottom: $P_{\mathrm{WLA}} = 500\,\mathrm{W}$

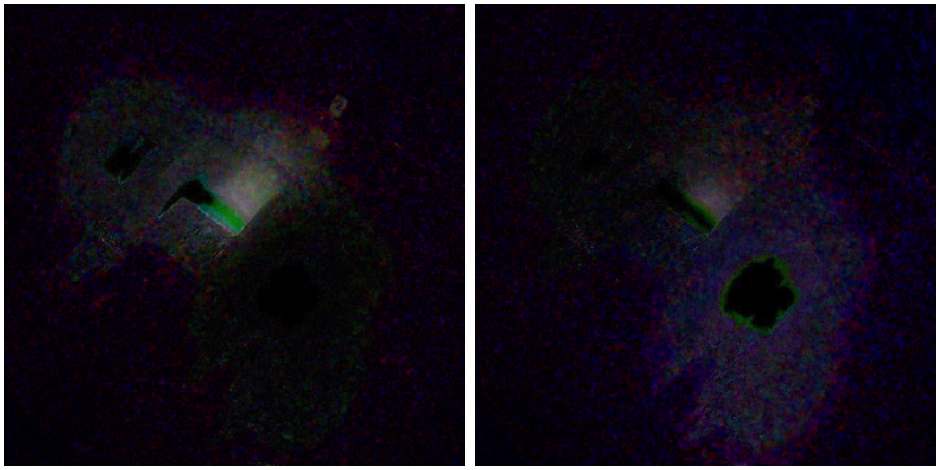

Figure B.5: Differences in Visible Exhaust Plume Intensity as WLA Power is Increased from 0 to 500 W. Left: $B_0 = 26\,\mathrm{G}$, Right: $B_0 = 50\,\mathrm{G}$. Top: $P_{\mathrm{WLA}} = 0\,\mathrm{W}$

Appendix C

Ion Energy Measurements of the DWDTX Exhaust using a Retarding Potential Analyzer[4]

Mach probe measurements were used to validate the scaling behavior in the DWDTX. A previous attempt to verify ion acceleration in the DWDTX plume was done using a retarding potential analyzer (RPA). In order to demonstrate that ion energies are increasing, we take measurements of the ion energy distribution function (IEDF) using the RPA. We measured the evolution of these distribution functions for three plasma source configurations and single exciting frequency, as shown in Table C.1. The source plasma was generated with $\dot{m}_n = 1.6\,\mathrm{mg/s}$ and $P_{\mathrm{PSA}} = 360\,\mathrm{W}$ with varying B_0 (26, 40, 60 G), and the WLA was driven at 200 kHz.

For each of these conditions, we positioned the RPA on the plume centerline 18 cm from the glass tube edge, then increased the power to the WLA from 0 W to 400 W to 700 W. After each RPA measurement, we repositioned the emissive probe

[4]This appendix is based on work previously presented in [79]: Feldman, M.S., Choueiri, E.Y., and Jorns, B., "Ion Energy Measurements in a Direct Wave-Drive Thruster," *51st AIAA/ASME/SAE/ASEE Joint Propulsion Conference*, AIAA-2015-3726, Orlando, FL, July 27-29, 2015.

Table C.1: Plasma Source Data for Each RPA Trial

Trial	$\boldsymbol{B_0}$ **(G)**	$\boldsymbol{P_{\mathrm{PSA}}}$ **(W)**	$\boldsymbol{\dot{m}_n}$ **(mg/s)**	$\boldsymbol{\omega}$ **(kHz)**
A	25	400	1.6	200
B	40	400	1.6	200
C	55	400	1.6	200

Table C.2: Plasma Potential Measurements for increasing WLA Power with $B_0 =$ 26 G. EP measurements were taken at 18 cm from the edge of the glass tube. Error is taken from the larger estimates in the literature of 10%[75].

Trial	$\boldsymbol{P_{\mathrm{WLA}} = 0\,\mathrm{W}}$	$\boldsymbol{P_{\mathrm{WLA}} = 400\,\mathrm{W}}$	$\boldsymbol{P_{\mathrm{WLA}} = 700\,\mathrm{W}}$
A	50 V	51 V	53 V
B	44 V	46 V	48 V
C	34 V	42 V	45 V

(EP) at the same location and energized the WLA to determine the change in plasma potential. These plasma potentials shown in Table C.2 were used to correct the measured IEDFs.

The corrected IEDFs are shown in Figure C.1. For each source configuration before the addition of power to the WLA, the most probable ion voltages are slightly above 0 V. This is unsurprising as the measured Mach numbers in the plume varied between $M = 1-2$, which corresponds to at most 4 eV. However, the RPA experiences a significant spread in the measured ion voltages beyond what would be physically expected. This is likely do to the large plasma potentials compared to the ion energies. Because an ion must fall over the full space potential in order to reach the grounded collector plate, it is likely that the measured IEDF experiences substantial broadening from the measurement that does not in fact exist within the plasma. This is made more obvious by the fact that a significant fraction of the IEDF has ion voltages less than 0, which would correspond to ions moving in the wrong direction as they 'enter' the RPA. Rather, the more likely explanation is that most ions enter the RPA slowly with energies of only a few eV, but the anomalous broadening of the device slows

Table C.3: Plasma Potential Measurements for increasing WLA Power with $B_0 =$ 26 G. EP measurements were taken at 18 cm from the edge of the glass tube. Error is taken from the larger estimates in the literature of 10%[75].

Trial	**Ion Voltage Increase from $P_{\mathbf{WLA}} = 0 \rightarrow 700\,\mathbf{W}$**
A	1.2 V
B	0.4 V
C	0.2 V

some of these ions down as they fall to the grounded collector. When the measured plasma potential is subtracted off, the negative voltages appear.

Even in the presence of this broadening, we still observe a distinct shift in the IEDF during Trial A, which is the low B_0 case. As the WLA is energized, we see the left side of the broadened IEDF does not change substantially, but that the distribution appears to develop a high energy tail.

The changes in the IEDFs as the WLA is powered are shown in Figure C.1 along with a sample error bar that demonstrate the increase in high energy ions for the $B_0 = 26\,\mathrm{G}$ case. For the higher magnetic field cases, the observed differences in the IEDFs are small. This corresponds with our theoretical predictions, which suggest that coupling will improve for lower magnetic fields.

Unfortunately, due to the large energy spread generated by the RPA, it is difficult to determine the precise IEDFs. In fact, while the peak of the Δ IEDF functions occurs near 10 V, this is not necessarily indicative of the addition of 10 eV ions. Instead, this is likely due to a smaller energy increase. This is most easily seen by examining the average ion voltages from the distributions. The increase in expected ion voltage in each configuration for $P_{\mathrm{WLA}} = 700\,\mathrm{W}$ is shown in Table C.3. However, in addition to any error from the RPA broadening, the EP plasma potential measurement alone contributes a couple volts of error[74, 75]. Therefore these expected increases are not statistically significant. We determine exhaust velocity increases more precisely via the MP data taken in Chapter 5.

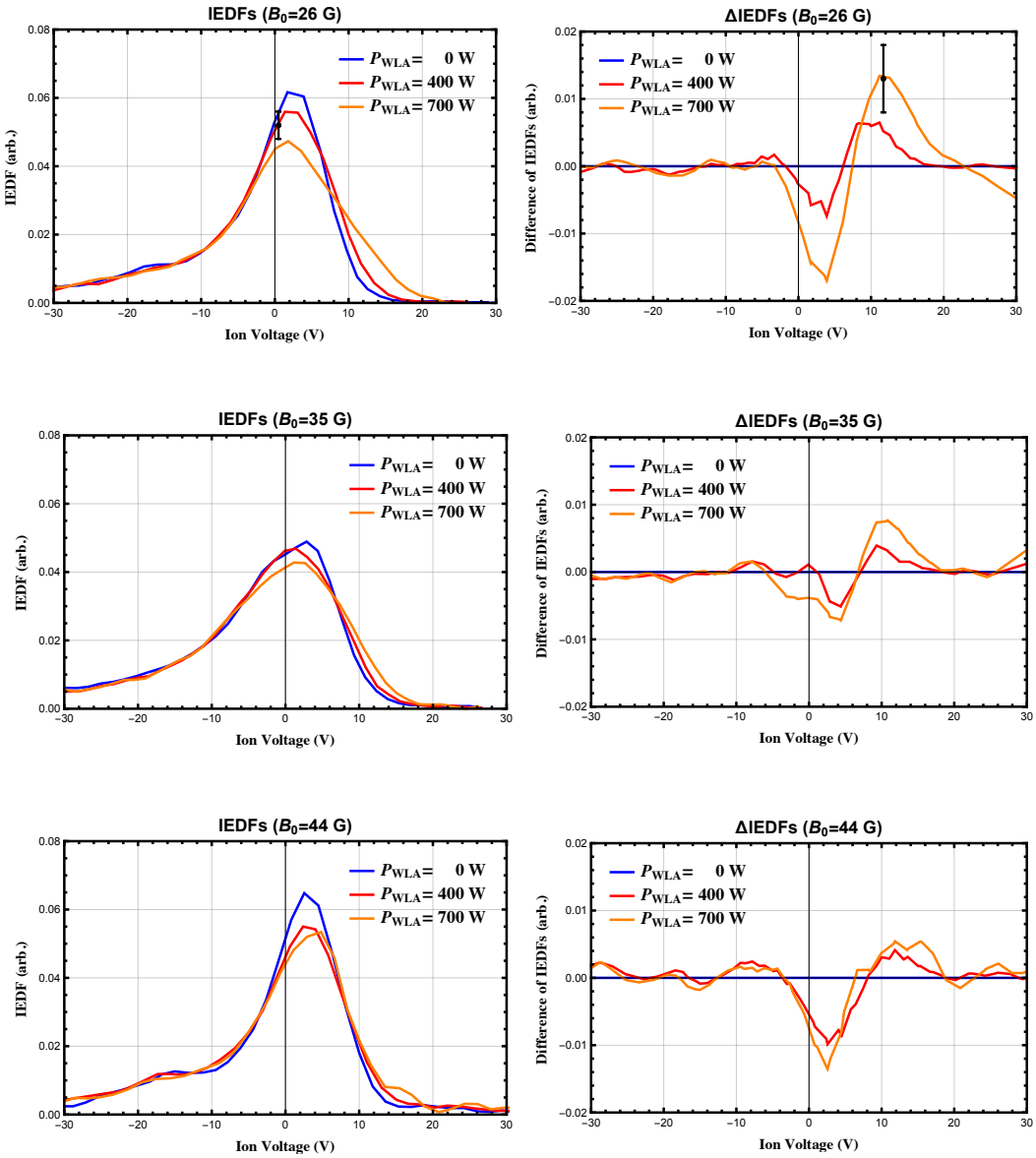

Figure C.1: Ion Energy Distribution Functions (IEDFs) for $P_{\mathrm{PSA}} = 360\,\mathrm{W}$, $\dot{m}_n = 1.6\,\mathrm{mg/s}$, $\omega = 2\pi \cdot 200\,\mathrm{kHz}$, and $B_0 = 26, 35, 44\,\mathrm{G}$. IEDFs are shown in normalized units for increasing P_{WLA}, and are smoothed and shown corrected for the measured plasma potential. The difference in the distribution functions are shown on the right comparing the 400 W and 700 W case to the zero power case.

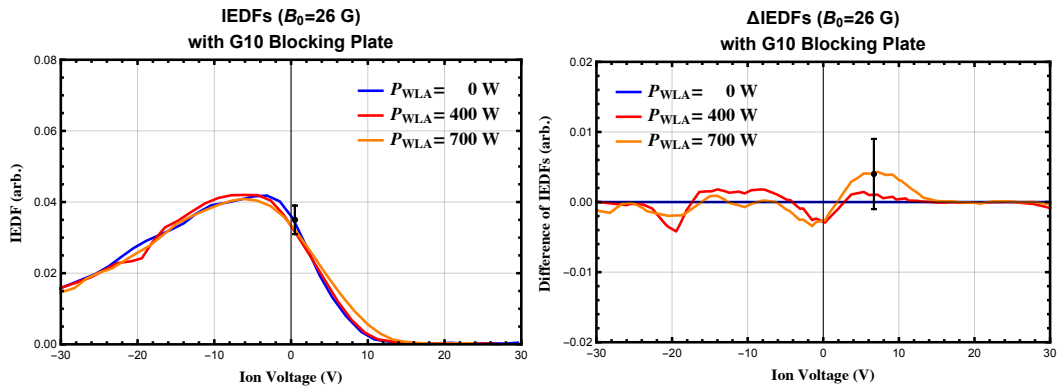

Figure C.2: Ion Energy Distribution Functions (IEDFs) for $P_{\mathrm{PSA}} = 360\,\mathrm{W}$, $\dot{m}_n = 1.6\,\mathrm{mg/s}$, $\omega = 2\pi \cdot 200\,\mathrm{kHz}$, and $B_0 = 26\,\mathrm{G}$ with a G10 plate 3 cm downstream of the RPA blocking the orifice, so that no beam ions can enter. IEDFs are shown in normalized units for increasing P_{WLA}, and are smoothed and shown corrected for the measured plasma potential. The difference in the distribution functions are shown on the right comparing the 400 W and 700 W case to the zero power case. Unlike the non-blocked case in Figure C.1, no significant acceleration is observed.

We have previously observed RF energy to cause spurious effects in the RPA traces. In order rule out these effects, we placed a 1 cm wide G10 plate 3 cm downstream in front of the RPA. This plate serves to block any potential beam ions while allowing the background distribution to still be measured. We then repeated the previous RPA sweeps at the lowest magnetic field, $B_0 = 26\,\mathrm{G}$ to verity that no beam is occurring. We follow the same procedure as before and subtract the IEDFs with varying WLA power from the base case of no added WLA power. These RPA traces are shown in Figure C.2. The increase in high energy ions that was seen without a blocking plate has mostly disappeared and is now well within experimental error. This is suggestive that the measured increase in the number of high energy ions is not a spurious effect of the RF or plasma potential increase.

Overall, these RPA measurements are too coarse to make explicit comparisons of the scaling of thrust or exhaust velocity to our analytical theory. While a major reason is that RPA broadening introduces substantial uncertainty in the measurement, a second issue is the time it takes to complete an RPA sweep. Because each sweep

takes over 30 seconds to complete, the WLA heats up significantly over the course of a data run. With no active cooling, attempts to take repeated measurements over a wide range of the parameter space led to damage of the WLA on multiple occasions. Nevertheless, the observed ion energy increases at lower magnetic field strengths is qualitatively consistent with our analytical predictions.

Appendix D

Charge Exchange Collisions in the DWDTX Plume

Because the exhaust plume is not fully ionized, the plume ions can be slowed via charge exchange collisions with the co-exhausting neutrals. These neutrals are neither directly accelerated by the addition of WLA power or by ambipolar effects and therefore move more slowly the ion population. In order to characterize these effects, we use our Mach probe to measure the flow velocity as the cold plume expands. That is, when no power is applied to the WLA. These measurements are plotted in Figure D.1 for various B_0 at $P_{\mathrm{PSA}} = 550\,\mathrm{W}$ and $\dot{m}_n = 2\,\mathrm{mg/s}$. Near the exit of the glass tube, the velocity decreases, but it stabilizes farther into the plume, where our eventual MP measurements were taken in Chapter 5.

In order to show this velocity decrease is consistent with charge exchange collisions with co-exhausting neutrals, we model the momentum transfer with the ion momentum equation:

$$m_i n_i v_i \frac{\partial v_i}{\partial x} = -m_i n_i v_i \nu_i, \tag{D.1}$$

or simply

$$\frac{\partial v_i}{\partial x} = -\nu_i. \tag{D.2}$$

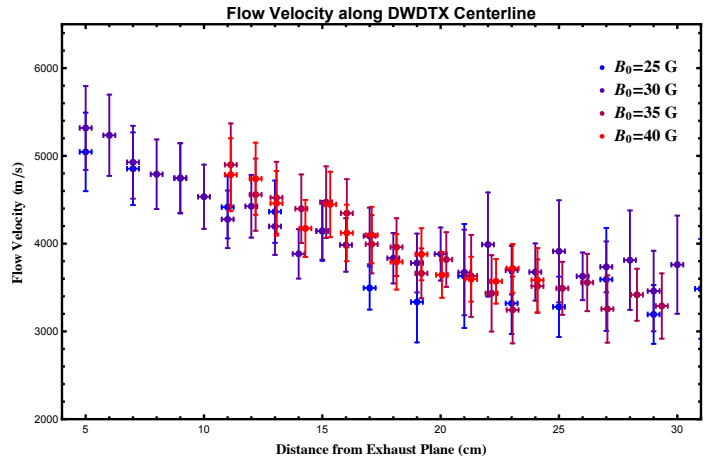

Figure D.1: Flow Velocity Variation Along Exhaust Plume Centerline.

That is, the spatial decay of the ion velocity is equal to the ion momentum exchange collision rate. And because we are only inputting argon gas into the chamber, we assume the dominant source of heavy neutrals is argon. So we simply need to know the $Ar^+ - Ar$ momentum exchange cross section in order to calculate ν_i.

This cross section is typically dominated by charge exchange collisions at the ion velocities of interest[80, 81]. Rather than a hard sphere Ar^+ ion colliding with a hard sphere neutral, an argon atom can simply 'give up' an electron to a passing argon ion. The cross section of this collision is larger than the typical size of an argon neutral, and so we will focus on it as the exclusive source of momentum exchange.

There are two possible neutral argon populations that can contribute to charge exchange collisions in the DWDTX: the background density of gas in the vacuum chamber and the non-ionized plume exhausting with the plasma. The background density, however, is much smaller than the neutral plume. To see this, we first calculate the expected neutral density as it leaves the glass exhaust hole.

$$\dot{m} = \rho v A_{cs}. \tag{D.3}$$

Ignoring any neutrals lost to the plasma generation, assuming the exhaust velocity is the thermal velocity of the injected neutrals, and noting the exhaust hole is an 8 cm x 8 cm square, we can calculate the neutral density at the exhaust plane.

$$\rho_n = \frac{\dot{m}_n}{c_{sn} A_{cs}} \tag{D.4}$$

For $\dot{m} = 2\,\mathrm{mg/s}$, $c_{sn} = 246\,\mathrm{m/s}$, and $A_{cs} = 64\,\mathrm{cm}^2$, we have $\rho_n = 1.27 * 10^{-6}\,\mathrm{kg/m}^3$, which gives a neutral particle density for argon of $n_n = 2 * 10^{19}\,\mathrm{m}^{-3}$. The background neutral density can be determined from the measured background pressure of the tank, which is typically near 30μTorr while operating the experiment. This corresponds to a neutral argon density of roughly $10^{18}\,\mathrm{m}^{-3}$ at room temperature. Therefore, we will only consider the neutrals streaming with the exhaust plume, rather than the full background density of the vacuum chamber.

From Equation D.2, and noting that $\nu_i = \sigma_{ce} n_n v_i$, we have the differential equation governing the ion plume velocity:

$$\frac{\partial v_i}{\partial x} = -\sigma_{ce} n_n v_i, \tag{D.5}$$

where we have assumed the neutral argon velocity is much smaller than the ion velocity. The charge exchange collision cross section, σ_{ce}, varies with ion velocity, but over the range of ion velocities measured in Figure D.1 remains roughly constant at $4 * 10^{-15}\,\mathrm{cm}^{-2}$[80, 81]. If we first assume a spatially constant neutral density, then the spatial velocity profile becomes

$$v_i(x) = v_i(0) e^{-x \sigma_{ce} n_n}. \tag{D.6}$$

And the length scale over which the ion velocity decays due to charge exchange collisions, $l_{ce} = 1/\sigma_{ce} n_n$, is approximately 12.5 cm.

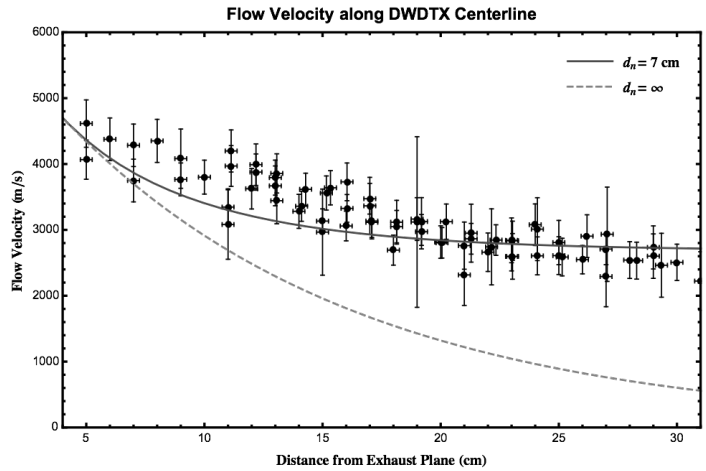

Figure D.2: Flow Velocity Variation Along Exhaust Plume Centerline with predicted change in velocity due to charge exchange collisions. The red dashed line assumes a constant argon neutral density, and the blue line assumes a spatially decaying neutral density.

However, as shown by the red line in Figure D.2, the velocity doesn't decay does not match prediction this prediction. This is likely because the neutral density in the plume is not constant, and instead decays spatially. As a result, the flow velocity lost to charge exchange collisions similarly decreases. If we assume the neutral density decay is exponential in nature, with a decay length, d_n, then Equation D.5 can be solved to

$$v_i(x) = v_i(0)e^{-(d_n/l_{ce})(1-e^{-x/d_n})}. \tag{D.7}$$

The neutral density decay rate outside of the glass cylinder is not a quantity we can directly measure. However, we can approximate the neutral density decay rate from the measured plasma density decay rate. Outside the cylinder, the plasma expands without any intervening magnetic field, and because both populations are expanding into vacuum from a similar geometry, we assume their density decay rates are similar. By fitting to the measured densities in Figure 4.20, we find the plasma density decays with a characteristic length scale of approximately 7 cm. Figure D.2 also shows this updated prediction by assuming the neutral density decays over a similar 7 cm length scale.

Finally, we note that since most of the charge exchange collisions are likely with the co-exhausting neutrals, the momentum generated is simply transferred into the neutral flowing particles. This does not substantially alter the potential thrust generation. However, it does effect our Mach number measurements such that they are underestimating the total momentum being injected into the plasma plume.

Appendix E

Direct Wave-Drive Thruster Experiment Circuitry

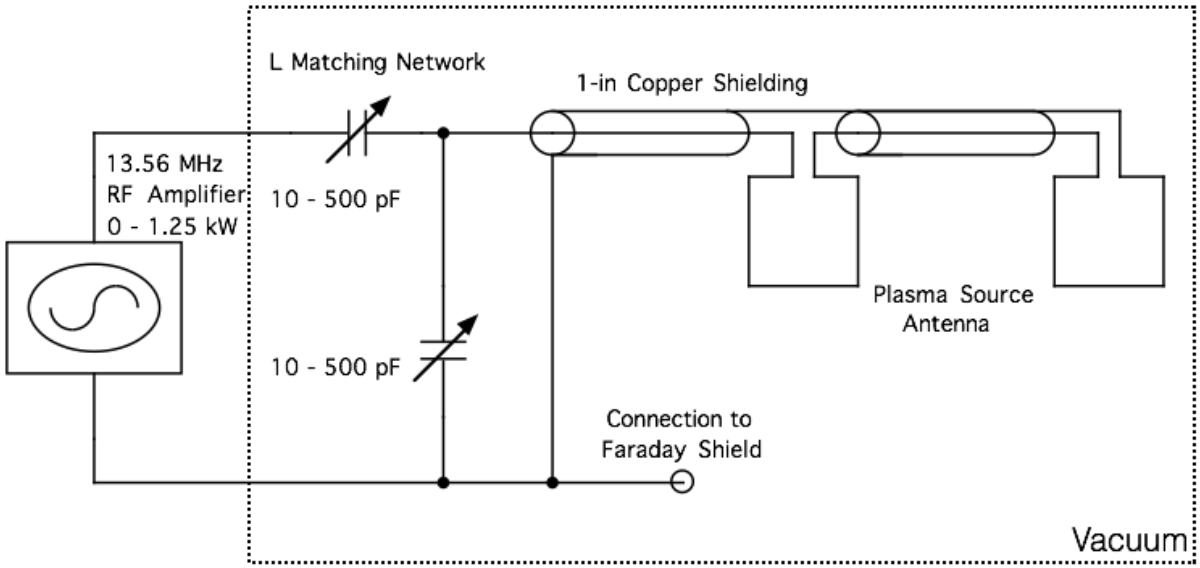

Figure E.1: Plasma Source Antena Tuning Circuitry. A simple capacitive L-network matches the 13.56 Mhz signal to the PSA.

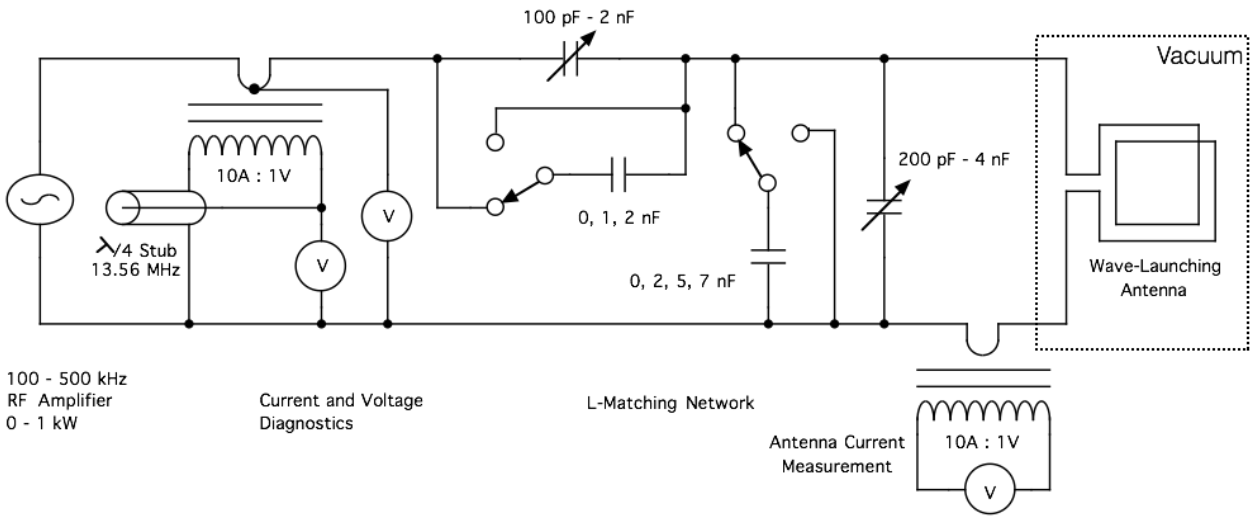

Figure E.2: Wave-Launching Antenna Tuning Circuitry and Diagnostics. Voltage and current before and after the tuning circuit are measured. A quarter-wave stub is used to filter 13.56 MHz noise from the smaller current signal measurement.

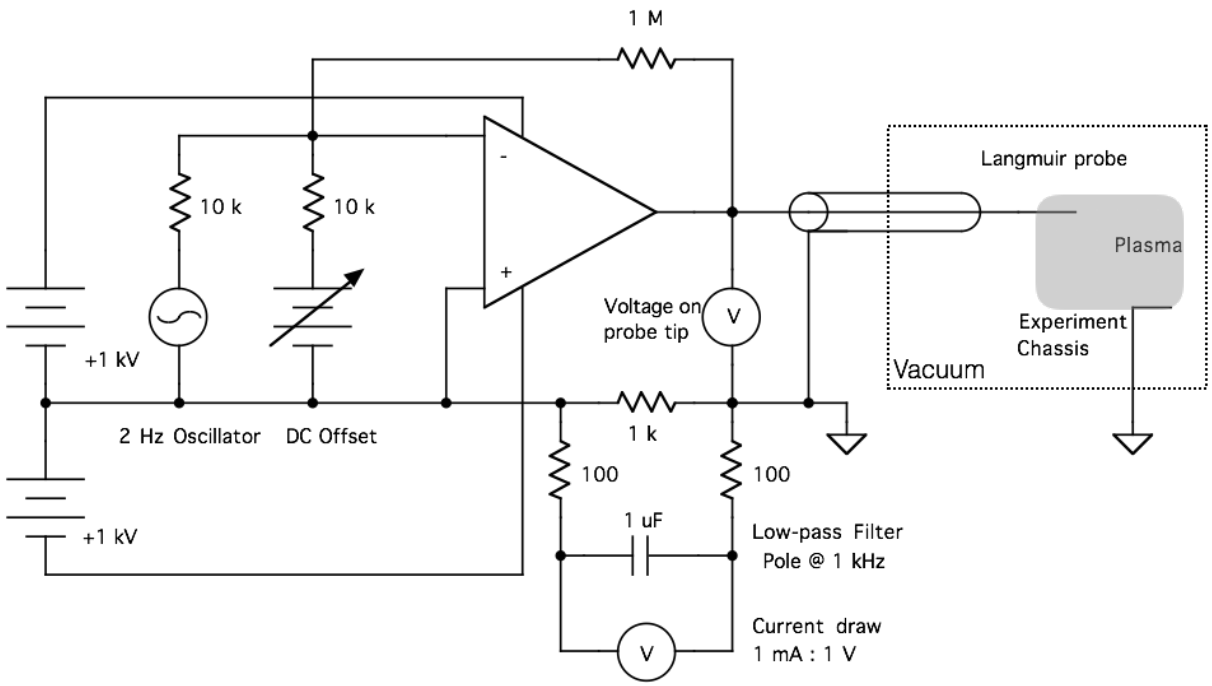

Figure E.3: Langmuir Probe Driver Circuit. Current flowing into the probe is measured over a 1 kΩ sense resistor and a low-pass filter.

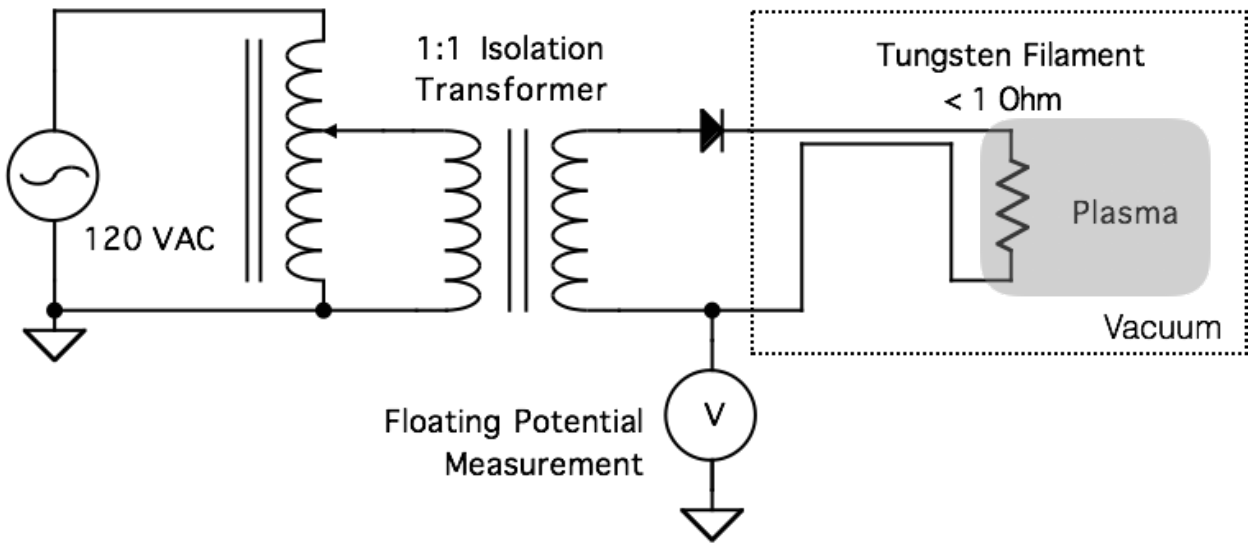

Figure E.4: Emissive Probe Driver Circuit. The emissive probe is isolated and heated with a Variac. A bias diode only allows heating during half the 60 Hz cycle, so that a floating measurement can be taken during the off half-cycle.

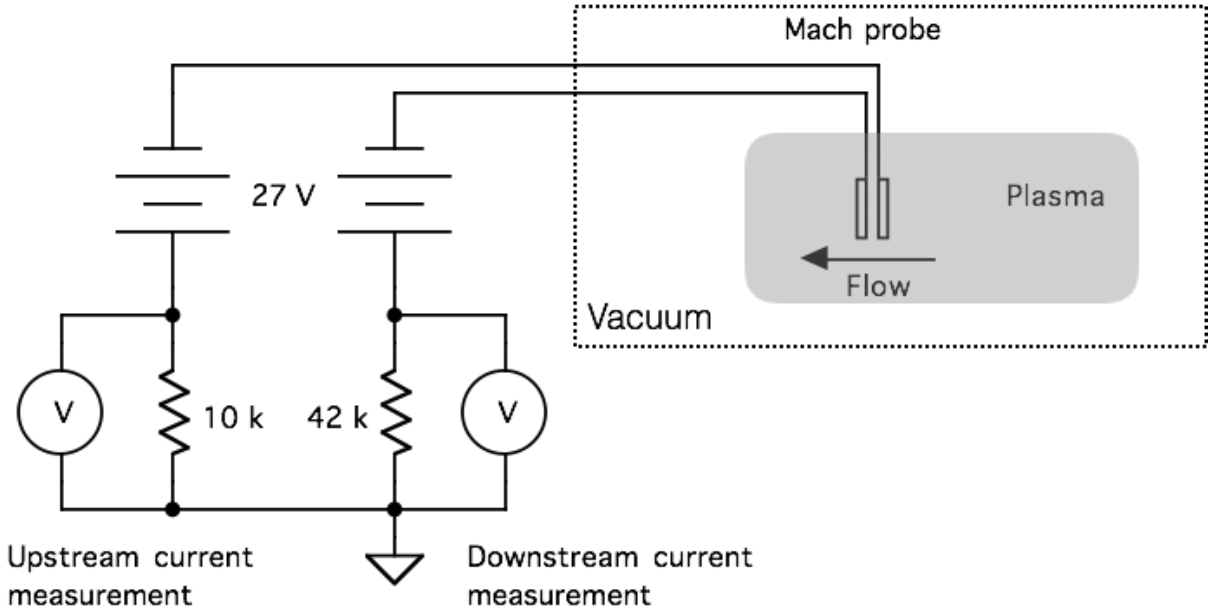

Figure E.5: Mach Probe Driver Circuit. Each surface of the Mach probe is biased into ion saturation. Two different sense resistors are used in order to help maintain an equal voltage on both probes.

Bibliography

[1] Jahn, R., *Physics of Electric Propulsion*, McGraw-Hill, New York, NY, 1968.

[2] Goebel, D. and Katz, I., *Fundamentals of Electric Propulsion: Ion and Hall Thrusters*, John Wiley and Sons, Hoboken, NJ, 2008.

[3] Shastry, R., Herman, D., Soulas, G., and Patterson, M., "NASA's Evolutionary Xenon Thruster (NEXT) Long-Duration Test as of 736 kg of Propellant Throughput," *48th AIAA Joint Propulsion Conference*, Atlanta, GA, 2012.

[4] Polk, J., Brinza, D., Kakuda, R., Brophy, J., Katz, I., and Anderson, J., "Demonstration of the NSTAR Ion Propulsion System on the Deep Space One Mission," *27th International Electric Propulsion Conference*, Pasadena, CA, 2001.

[5] Jacobson, D., Manzella, D., Hofer, R., and Peterson, P., "NASA's 2004 Hall Thruster Program," *40th AIAA Joint Propulsion Conference*, For Lauderdale, FL, 2004.

[6] Hofer, R. and et. al., "Development Approach and Status of the 12.5 kW HERMeS Hall Thruster for the Solar Electric Propulsion Technology Demonstration Mission," *34th International Electric Propulsion Conference*, Kobe, Japan, 2015.

[7] Polk, J., Jaskowsky, W., Kelly, A., and Jahn, R., "Measurement of MPD Thruster Erosion Using Surface Layer Activation," *Journal of Propulsion and Power*, Vol. 3, No. 1, 1987.

[8] Choueiri, E. Y. and Ziemer, J., "Quasi-Steady Magnetoplasmadynamic Thruster Performance Database," *Journal of Propulsion and Power*, Vol. 17, No. 5, 2001, pp. 967–976.

[9] Plasek, M., Wordingham, C. J., Rojas Mata, S., Luzarraga, N., and Choueiri, E. Y., "Experimental Investigation of a Large Diameter Cathode," *50th AIAA/ASME/SAE/ASEE Joint Propulsion Conference*, 2014, AIAA-2014-3825.

[10] Goebel, D. and Chu, E., "High Current Lanthanum Hexaboride Hollow Cathode for High-Power Hall Thrusters," *Journal of Propulsion and Power*, Vol. 30, No. 1, 2014.

[11] Chu, E. and Goebel, D., "High-Current Lanthanum Hexaboride Hollow Cathode for 10-50-kW Hall Thrusters," *IEEE Transactions on Plasma Science*, Vol. 40, No. 9, 2012.

[12] Noord, J. V., Kamhawi, H., and Mcewen, H., "Characterization of a High Current, Long Life Hollow Cathode," *29th International Electric Propulsion Conference*, Princeton, NJ, 2005.

[13] Lev, D. and Choueiri, E. Y., "Scaling of Efficiency with Applied Magnetic Field in Magnetoplasmadynamic Thrusters," *Journal of Propulsion and Power*, Vol. 28, No. 3, 2012.

[14] Hooper, E., "Plasma detachment from a magnetic nozzle," *Journal of Propulsion and Power*, Vol. 9, No. 5, 1993.

[15] Diaz, F., "The Vasimr Rocket," *Scientific American*, Vol. 283, No. 5, November 2000, pp. 90–97.

[16] Takahashi, K., Charles, C., Boswell, R., and Ando, A., "Performance Improvement of a Permanent Magnet Helicon Thruster," *Journal of Physics D: Applied Physics*, Vol. 46, No. 35, 2013, pp. 352001.

[17] Pavarin, D., Ferri, F., and et. al., "Design of a 50 W Helicon Plasma Thruster," *31st International Electric Propulsion Conference*, No. IEPC-2009-205, September 2009.

[18] Lovberg, R. and Dailey, C., "PIT Mark V Design," *Conference on Advanced SEI Technologies*, No. AIAA-1991-3571, September 1991.

[19] Choueiri, E. Y. and Polzin, K., "Faraday Acceleration with Radio-frequency Assisted Discharge," *Journal of Propulsion and Power*, Vol. 22, No. 3, 2006, pp. 611–619.

[20] Brown, D., Beal, B., and Haas, J., "Air Force Research Laboratory High Power Electric Propulsion Technology Development," *2010 IEEE Aerospace Conference*, March 6-13, 2010, pp. 1–9.

[21] Slough, J., Kirtley, D., and Weber, T., "Pulsed Plasmoid Propulsion: The ELF Thruster," *31st International Electric Propulsion Conference*, No. IEPC-2009-265, Ann Arbor, Michigan, Sept 20-24, 2009.

[22] Ahedo, E. and Merino, M., "On Plasma Detachment in Propulsive Magnetic Nozzles," *Physics of Plasmas*, Vol. 18, No. 5, 2011, pp. 053504.

[23] Arefiev, A. and Breizman, B., "Magnetohydrodynamic scenario of plasma detachment in a magnetic nozzle," *Physics of Plasmas*, Vol. 12, No. 4, 2005, pp. 043504.

[24] Merino, M. and Ahedo, E., "Plasma detachment in a propulsion magnetic nozzle via ion demagnetization," *Plasma Sources Science and Technology*, Vol. 23, No. 3, 2014.

[25] Polzin, K., "Comprehensive Review of Planar Pulsed Inductive Plasma Thruster Research and Technology," *Journal of Propulsion and Power*, Vol. 27, No. 3, 2011, pp. 513–531.

[26] Meeks, W., Pahl, R., and Rovey, J., "Investigation of Pre-ionization Characteristics in Heavy Gas Pulsed Inductive Plasmas via Numerical Modeling," *47th AIAA Joint Propulsion Conference*, No. AIAA-2011-5655, San Diego, CA, August 2011.

[27] Toki, K., Shinohara, S., Tokai, T., and et. al., "On the Electrodeless MPD Thruster Using a Compact Helicon Plasma Source," *44th AIAA/ASME/SAE/ASEE Joint Propulsion Conference*, No. AIAA-2008-4729, Hartford, CT, July 21-23, 2009.

[28] Satoh, S., Matsuoka, T., Fujino, T., and Funaki, I., "A Theoretical Analysis for Electrodeless Lissajous Acceleration of HELICON Plasmas," *42nd AIAA Plasmadynamics and Lasers Conference in conjunction with the 18th International Conference on MHD Energy Conversion (ICMHD)*, No. AIAA-2011-4008, Honolulu, HI, June 27-30, 2011.

[29] Emsellem, G., "Electrodeless Plasma Thruster Design," *41st AIAA/ASME/SAE/ASEE Joint Propulsion Conference*, No. AIAA-2005-3855, Tucson, Arizona, July 10-13, 2005.

[30] Jorns, B. and Choueiri, E., "Thruster concept for transverse acceleration by the beating electrostatic wave ponderomotive force," *32nd International Electric Propulsion Conference*, No. IEPC-2011-214, Wiesbaden, Germany, September 11-15, 2011.

[31] Benisti, D., Ram, A., and Bers, A., "Ion dynamics in multiple electrostatic waves in a magnetized plasma. I. Coherent acceleration," *Physics of Plasmas*, Vol. 5, No. 9, 1998.

[32] Jorns, B. and Choueiri, E. Y., "Experimental Characterization of Plasma Heating with Beating Electrostatic Waves," *AIAA's 48th Joint Propulsion Conference*, No. AIAA-2012-4194, July 30 - August 1, 2012.

[33] Jorns, B. and Choueiri, E. Y., "Experiment for Plasma Energization with Beating Electrostatic Waves," *31st International Electric Propulsion Conference*, No. IEPC-2009-199, September 21-24, 2009.

[34] Spektor, R. and Choueiri, E. Y., "Measurements of Ion Energization by a Pair of Beating Electrostatic Ion Cyclotron Waves," *29th International Electric Propulsion Conference*, No. IEPC-2005-289, October 31 - November 4, 2005.

[35] Peter, W. and Rostoker, N., "Theory of plasma injection into a magnetic field," *Physics of Fluids*, Vol. 25, No. 730, 1982.

[36] Jaeger, E., Berry, L., and Batchelor, D., "Full-wave calculation of Sheared Poloidal Flow Driven by High-Harmonic Ion Bernstein Waves in Tokamak Plasmas," *Physics of Plasmas*, Vol. 7, No. 8, 2000, pp. 3319–3329.

[37] Myra, J. and D'Ippolito, D., "Toroidal Formulation of Nonlinear-RF-Driven Flows," *Physics of Plasmas*, Vol. 9, No. 9, 2002, pp. 3867–3873.

[38] Myra, J., Berry, L., D'Ippolito, D., and Jaeger, E., "Nonlinear fluxes and forces from radio-frequency waves with application to driven flows in Tokamaks," *Physics of Plasmas*, Vol. 11, No. 5, 2004.

[39] Myra, J., D'Ippolito, D., Berry, D. R. L., Jaeger, E., and Carter, M., "Nonlinear ICRF Plasma Interactions," *Nuclear Fusion*, Vol. 46, No. 7, 2006.

[40] Fisch, N., Rax, J., and Dodin, I., "Current Drive in a Ponderomotive Potential with Sign Reversal," *Physics Review Letters*, Vol. 91, No. 20, 2003, pp. 205004.

[41] Gao, Z., Fisch, N., and Qin, H., "Nonlinear ponderomotive force by low frequency waves and nonresonant current drive," *Physics of Plasmas*, Vol. 13, No. 11, 2006.

[42] Fisch, N., "Theory of Current Drive in Plasmas," *Review of Modern Physics*, Vol. 59, No. 1, 1987, pp. 175.

[43] Motz, H. and Watson, C., "The Radio-frequency Confinement of Plasmas," *Advances in Electronics and Electron Physics*, Vol. 23, Academic Press, 1967.

[44] Feldman, M. S. and Choueiri, E. Y., "The Direct Wave-Drive Thruster," *50th AIAA Joint Propulsion Conference*, No. AIAA-2014-4025, Cleveland, OH, July 28-30, 2014.

[45] Choueiri, E. Y., "The Scaling of Thrust in Self-Field Magnetoplasmadynamic Thrusters," *Journal of Propulsion and Power*, Vol. 14, No. 5, 1998, pp. 744–753.

[46] Dodd, C. and Deeds, W., "Analytical Solutions to the Eddy-Current Probe-Coil Problems," *Journal of Applied Physics*, Vol. 39, No. 6, 1968, pp. 2829–2838.

[47] Skiff, F., Ono, M., and Wong, K., "Excitation of Ion Bernstein Waves from Loop Antennas," 1988.

[48] Brambilla, M., "Theory of Bernstein Wave Coupling with Loop Antennas," *Nuclear Fusion*, Vol. 28, No. 4, 1988.

[49] Purcell, E., *Electricity and Magnetism*, McGraw-Hill, New York, NY, 1985.

[50] Feldman, M. S. and Choueiri, E. Y., "A Direct Wave-Drive Thruster using the Magnetosonic Mode," *34th International Electric Propulsion Conference*, No. IEPC-2015-115, Kobe, Japan, July 6-10, 2015.

[51] Chiu, S., Chan, V., Harvey, R., and Porkolab, M., "Theory of Fast Wave Current Drive For Tokamak Plasmas," *Nuclear Fusion*, Vol. 29, No. 12, 1989.

[52] Goree, J., Ono, M., Colestock, P., Horton, R., McNeill, D., and Park, H., "Fast-Wave Current Drive in a Toroidal Plasma," *Physical Review Letters*, Vol. 55, No. 16, 1985.

[53] Dodin, I. and Fisch, N., "Axiomatic Geometrical Optics, Abraham-Minkowski controversy and photon properties derived classically," *Physics Review A*, Vol. 86, No. 053834, 2012.

[54] Dodin, I., "On Variational Methods in the Physics of Plasma Waves," *Fusion Science and Technology*, Vol. 65, No. 1, 2014.

[55] Chen, F., *Introduction to Plasma Physics and Controlled Fusion*, Springer, 1984.

[56] Little, J. and Choueiri, E. Y., "Critical Condition for Plasma Confinement in the Source of a Magnetic Nozzle Flow," *IEEE Transactions on Plasma Science*, Vol. 43, No. 1, 2015, pp. 277–286.

[57] Chen, F., "Experiments on helicon plasma sources," *Journal of Vacuum Science Technology A*, Vol. 10, No. 4, 1992.

[58] Stix, T. H., *Waves in Plasmas*, American Institute of Physics, Springer-Verlag New York, Inc, 1992.

[59] Feldman, M. S. and Choueiri, E. Y., "Single Stage Faraday Accelerator with Radio-frequency Assisted Discharge," *32nd International Electric Propulsion Conference*, No. IEPC-2011-220, Wiesbaden, Germany, September 11-15, 2011.

[60] Melazzi, D. and Lancellotti, V., "A comparative study of radiofrequency antennas for Helicon plasma sources," *Plasma Sources Science and Technology*, Vol. 24, No. 2, 2015.

[61] Little, J. and Choueiri, E. Y., "Electron Cooling in a Magnetically Expanding Plasma," *Physical Review Letters*, Vol. 117, No. 22, 2016.

[62] Insulcast, *RTVS 3-95-2*, Batch 50268883.

[63] Bowick, C., *RF Circuit Design*, Newnes, 2nd Edition, 1982.

[64] Pearson Electronics, Inc, *Pearson Current Monitor, Model 411*, 2002.

[65] Hutchinson, I., *Principles of Plasma Diagnostics*, Cambridge University Press, 2005.

[66] Chen, F., "Langmuir probe analysis for high density plasmas," *Physics of Plasmas*, Vol. 8, 2001.

[67] Hutchinson, I., "Ion collection by probes in strong magnetic fields with plasma flow," *Physics Review A*, Vol. 37, No. 11, 1988.

[68] Hutchinson, I., "The invalidity of a Mach Probe model," *Physics of Plasmas*, Vol. 9, 2002.

[69] Hudis, M. and Lidsky, L., "Directional Langmuir Probe," *Journal of Applied Physics*, Vol. 41, 1970.

[70] Hutchinson, I., "Ion collection by a sphere in a flowing plasma: I. Quasineutral," *Plasma Physics and Controlled Fusion*, Vol. 44, 2002.

[71] Oksuz, L., Khedr, M. A., and Hershkowitz, N., "Laser induced fluorescence of argon ions in a plasma presheath," *Physics of Plasmas*, Vol. 8, 2001.

[72] Oksuz, L. and Hershkowitz, N., "Understanding Mach probes and Langmuir probes in a drifting, unmagnetized, non-uniform plasma," *Plasma Sources Science and Technology*, Vol. 13, No. 2, 2004.

[73] Conversano, R. and et. al., "Development and Initial Testing of a Magnetically Shielded Miniature Hall Thruster," *IEEE Transactions on Plasma Science*, 2014.

[74] Dorf, L., Raitses, Y., and Fisch, N., "Electrostatic probe apparatus for measurements in the near-anode region of hall thrusters," *Review of Scientific Instruments*, Vol. 75, No. 5, 2004.

[75] Sheehan, J. and Hershkowitz, N., "Emissive Probes," *Plasma Sources Science and Technology*, Vol. 20, No. 063001, 2001.

[76] Little, J., *Performance Scaling of Magnetic Nozzles for Electric Propulsion*, Ph.D. thesis, Princeton University, 2015.

[77] Feldman, M. S. and Choueiri, E. Y., "Thrust Scaling in a Direct Wave-Drive Thruster," *52nd AIAA Joint Propulsion Conference*, No. AIAA-2016-4948, Salt Lake City, UT, July 25-27, 2016.

[78] Logitech International S.A., *Logitech HP Pro Webcam C920*, 2011.

[79] Feldman, M. S., Choueiri, E. Y., and Jorns, B., "Ion Energy Measurements in a Direct Wave-Drive Thruster," *51st AIAA Joint Propulsion Conference*, No. AIAA-2015-3726, Orlando, FL, July 27-29, 2015.

[80] Nichols, B. J. and Witteborn, F. C., "Measurements of Resonant Charge Exchange Cross Sections in Nitrogen and Argon Between 0.5 and 17 eV," Tech. Rep. NASA TN D-3265, Ames Research Center, Washington D.C., 1966.

[81] Hegerberg, R., Elford, M., and Skullerud, H., "The cross section for symmetric charge exchange of Ne+ in Ne and Ar+ in Ar at low energies," *Journal of Physics B*, Vol. 15, No. 5, 1981.